Plasticity of Human Microglia and Brain Perivascular Macrophages in Aging and Alzheimer's Disease

Authors

Donghoon Lee[#†1,2,3,4], James M. Vicari[#1,2,3,4], Christian Porras[#1,2,3,4], Collin Spencer[#1,2,3,4], Milos Pjanic[1,2,3,4], Xinyi Wang[1,2,3,4], Seon Kinrot[1,2,3,4], Philipp Weiler[5,6], Roman Kosoy[1,2,3,4], Jaroslav Bendl[1,2,3,4], Prashant N M[1,2,3,4], Konstantina Psychogyiou[1,2,3,4], Periklis Malakates[1,2,3,4], Evelyn Hennigan[1,2,3,4], Jennifer Monteiro Fortes[1,2,3,4], Shiwei Zheng[3,7,8], Karen Therrien[1,2,3,4], Deepika Mathur[1,2,3,4], Steven P. Kleopoulos[1,2,3,4], Zhiping Shao[1,2,3,4], Stathis Argyriou[1,2,3,4], Marcela Alvia[1,2,3,4], Clara Casey[1,2,3,4], Aram Hong[1,2,3,4], Kristin G. Beaumont[3], Robert Sebra[3], Christopher P. Kellner[9], David A. Bennett[10], Guo-Cheng Yuan[3,7,8], George Voloudakis[1,2,3,4], Fabian J. Theis[5,6,11], Vahram Haroutunian[2,4,12,13], Gabriel E. Hoffman[1,2,3,4,13], John F. Fullard[#1,2,3,4], Panos Roussos[#†1,2,3,4,13]

Affiliations

[1] Center for Disease Neurogenomics, Icahn School of Medicine at Mount Sinai, New York, NY, USA.
[2] Department of Psychiatry, Icahn School of Medicine at Mount Sinai, New York, NY, USA.
[3] Department of Genetics and Genomic Sciences, Icahn School of Medicine at Mount Sinai, New York, NY, USA.
[4] Friedman Brain Institute, Icahn School of Medicine at Mount Sinai, New York, NY, USA.
[5] Institute of Computational Biology, Helmholtz Center Munich, Munich, Germany.
[6] Department of Mathematics, Technical University of Munich, Munich, Germany.
[7] Tisch Cancer Institute, Icahn School of Medicine at Mount Sinai, New York, NY 10029, USA.
[8] Black Family Stem Cell Institute, Icahn School of Medicine at Mount Sinai, New York, NY 10029, USA.
[9] Department of Neurosurgery, Icahn School of Medicine at Mount Sinai, New York, NY, USA.
[10] Rush Alzheimer's Disease Center, Rush University Medical Center, Chicago, IL, USA.
[11] TUM School of Life Sciences Weihenstephan, Technical University of Munich, Munich, Germany.
[12] Department of Neuroscience, Icahn School of Medicine at Mount Sinai, New York, NY, USA.
[13] Mental Illness Research, Education and Clinical Centers, James J. Peters VA Medical Center, Bronx, New York.

[#]These authors contributed equally to this work.
[†]Corresponding author: donghoon.lee@mssm.edu; panagiotis.roussos@mssm.edu

Abstract

The complex roles of myeloid cells, including microglia and perivascular macrophages, are central to the neurobiology of Alzheimer's disease (AD), yet they remain incompletely understood. Here, we profiled 832,505 human myeloid cells from the prefrontal cortex of 1,607 unique donors covering the human lifespan and varying degrees of AD neuropathology. We delineated 13 transcriptionally distinct myeloid subtypes organized into 6 subclasses and identified AD-associated adaptive changes in myeloid cells over aging and disease progression. The GPNMB subtype, linked to phagocytosis, increased significantly with AD burden and correlated with polygenic AD risk scores. By organizing AD-risk genes into a regulatory hierarchy, we identified and validated *MITF* as an upstream transcriptional activator of *GPNMB*, critical for maintaining phagocytosis. Through cell-to-cell interaction networks, we prioritized *APOE-SORL1* and *APOE-TREM2* ligand-receptor pairs, associated with AD progression. In both human and mouse models, *TREM2* deficiency disrupted GPNMB expansion and reduced phagocytic function, suggesting that GPNMB's role in neuroprotection was *TREM2*-dependent. Our findings clarify myeloid subtypes implicated in aging and AD, advancing the mechanistic understanding of their role in AD and aiding therapeutic discovery.

Main

Despite the quantifiable neuropathology of β-amyloid plaques (Aβ) and neurofibrillary tangles (NFTs) (*1*), the exact neurobiological mechanisms underlying Alzheimer's disease (AD) remain elusive. Brain myeloid-origin immune cells, including microglia and perivascular macrophages (PVMs), play crucial roles in the pathogenesis of AD (*2–9*), providing neuroprotective benefits by clearing lesions, but also exacerbating the disease through the induction of excessive neuroinflammation (*10*). While previous studies utilizing single-nucleus/-cell RNA sequencing (snRNA-seq/scRNA-seq) have made significant progress describing complex functional roles of murine and human microglia in AD (*5*, *11–14*), challenges with characterizing the wide spectrum of microglial heterogeneity and identifying more nuanced AD-associated subtypes still remain (*15*), largely due to limited sample sizes and differences in the single-cell technologies used. Among the issues that arise is the failure of nuclear fractions in snRNA-seq from frozen tissue to capture key genes related to microglial adaptation and response to pathogenic lesions (*16*). Moreover, microglia are highly reactive cells, and describing their adaptive nature using scRNA-seq in cells isolated from fresh tissue is challenging (*17*). To overcome those limitations, we present two independent human myeloid cohorts generated at single-cell resolution from the prefrontal cortex (PFC). In the first cohort, we isolated viable *ex-vivo* human myeloid cells from fresh postmortem PFC and deeply profiled both nuclear and cytoplasmic RNA. The second cohort focused on the breadth of the transcriptome, profiling human myeloid nuclei from a large number of demographically diverse frozen cortical tissues. By considering both the depth and the breadth of the human myeloid transcriptome, we establish a reproducible taxonomy and demonstrate the importance of

77   microglia and PVM plasticity throughout the lifespan, across different stages of AD
78   pathological and clinical severity, and genetic liability.

79

Cellular taxonomy of human myeloid cells

81   In total, we profiled 832,505 human myeloid cells from the PFC of 1,607 unique donors.
82   The first dataset, named FreshMG, includes samples from fresh autopsy tissue specimens of
83   137 unique postmortem donors recruited from two brain banks and contains individuals
84   displaying varying degrees of AD neuropathology as well as controls (**Fig. 1A, Supplementary**
85   **Fig. S1A**). FreshMG donors are aged between 26 and 107 years (average 80.7 years),
86   comprising 76 females and 61 males. To enrich for myeloid cells, viable CD45+ cells were
87   isolated via fluorescence-activated cell sorting (FACS). In addition, for a subset (n=3 donors,
88   each with 8 technical replicates), we profiled surface-level protein markers using CITE-seq (*18*),
89   using a panel of 154 unique antibodies, resulting in a total of 161 scRNA-seq libraries from
90   fresh brain specimens. Following rigorous QC and initial clustering, we found a large, relatively
91   homogeneous, cluster of myeloid cells along with small subsets of co-purified immune cells,
92   such as monocytes, neutrophils, T, NK, and B cells. The myeloid cluster consisted of 543,012
93   microglia and PVMs robustly expressing 23,740 genes (**Supplementary Fig. S1E**).
94   The second dataset, named PsychAD, consists of frozen prefrontal cortex specimens and
95   includes cases and controls from a cohort of 1,470 unique donors (**Fig. 1B**). PsychAD donors
96   were aged between 0 and 108 years, (average 71.3 years), comprising 761 females and 709
97   males (**Supplementary Fig. S1B**). Frozen samples were subject to snRNA-seq profiling from
98   which microglia and PVMs were sorted *in silico* after basic clustering. After rigorous QC, we
99   identified 289,493 microglia and PVM nuclei robustly expressing 34,890 genes
100   (**Supplementary Fig. S1F**). Next, we aligned and harmonized the scale of clinical variables to
101   facilitate annotation of both datasets (**Methods**) and saw a strong positive correlation with
102   measures of the severity of AD neuropathology, namely diagnostic certainty of AD, Consortium
103   to Establish a Registry for Alzheimer's Disease (CERAD) (*19*), and Braak stage (*20*)
104   (**Supplementary Fig. S1C**). In contrast, the clinical measures of dementia severity were less
105   well correlated with AD.
106   Our primary objective was to establish a comprehensive cellular taxonomy that is robust
107   and reproducible; however, cross-validating these independent and large-scale single-cell
108   datasets, each with a distinct transcriptomic origin (whole cell vs. nuclei), posed technical
109   challenges. To overcome these, we devised an iterative cross-validation strategy, which
110   involved establishing a reference state and validating it independently until both datasets were
111   in agreement (**Methods**). Utilizing the FreshMG dataset, which provides comprehensive
112   transcriptomic profiles from both nuclear and cytosolic fractions, we identified functionally
113   distinct phenotypes of microglia and PVMs. Subsequently, we cross-validated the presence of
114   these reference subtypes in the frozen specimen snRNA-seq PsychAD dataset. Our iterative
115   process converged on 13 functionally distinct subtypes of human myeloid cells (**Fig. 1C,**
116   **Supplementary Fig. S2A, Supplementary Tables S1-2**), and comparison between FreshMG

117   and PsychAD revealed a high degree of consistency between the two cohorts, as evidenced by

118   an average Pearson correlation of 0.77 across all identified subtypes (**Fig. 1F**). This rigorous

119   methodology ensured the accuracy and reliability of our cellular taxonomy, laying a solid

120   foundation for further analyses.

121   We grouped the cells using two levels of taxonomic hierarchy; the 13 distinct subtypes

122   under six broad functional subclasses of human myeloid cells: Homeostatic (green), Adaptive

123   (blue), Proliferative (yellow), AD-Associated or ADAM (red), *ex-vivo* Activated Microglia or exAM

124   (pink), and PVM (orange) (**Fig. 1C**). Each subtype is associated with specific markers that not

125   only aid in their identification but also hint at their functional significance (**Fig. 1D,**

126   **Supplementary Fig. S2D**). Within the homeostatic microglia subclass, we highlight two

127   subtypes, CECR2 and PICALM, both of which are associated with the regulation of GTPase

128   activity. Homeostatic microglia make up the largest proportion of myeloid cells

129   (**Supplementary Figs. S2B-C**) and express microglia-specific canonical markers such as

130   *P2RY12* and *CX3CR1*. The CECR2 subtype uniquely expresses *CECR2* and *NAV2*, with other

131   genes pointing towards cellular maintenance, phagocytosis, cell migration, and adhesion. The

132   PICALM subtype shows elevated expression of *PICALM* and *ELMO1*, suggesting roles in the

133   regulation of the immune response.

134   We identified 7 specialized microglial subtypes, each exhibiting unique adaptive responses

135   to neuro-environmental cues. In general, the gene signatures across these adaptive microglia

136   underscored an enhancement in antigen processing and presentation programs and the

137   facilitation of MHC protein complex assembly. The CCL3 subtype is characterized by the

138   upregulation of chemotactic genes, most notably the inflammatory cytokines *CCL3*, *CCL4*, and

139   interleukin 1 beta (*IL1B*). In addition, the *IFI44L* subtype is enriched in interferon-inducible

140   genes, like *IFIT1*, *IFIT2*, and *IFIT3*, suggesting a role in the antiviral innate immune response.

141   The AIF1, HIF1A, and HIST clusters share a common gene program related to immunoglobulin-

142   mediated immune response, while the TMEM163 cluster focuses on antigen processing and

143   presentation via MHC II. The final adaptive cluster, HSPA1A, is enriched for gene signatures

144   responsible for adaptive response to unfolded protein, which is characterized by elevated

145   activity of heat shock proteins and cellular stress response, with a potential role in AD

146   neuropathology (*21*). In addition, we identified a subtype, the GPNMB, which is predominantly

147   observed in individuals with AD (*22*, *23*). These AD-associated microglia (ADAM) feature

148   elevated expression of glycoprotein non-metastatic melanoma protein B (*GPNMB*),

149   microphthalmia-associated transcription factor (*MITF*), and protein tyrosine phosphatase

150   receptor type G (*PTPRG*) genes, and functional enrichment analysis suggests increased

151   phagocytic activity is a hallmark of these cells. Consistent with previous studies (*11*), we also

152   identified a cluster of proliferative cells, MKI67, that is highly enriched in cell-cycle dependent

153   genes (*STMN1*, *MKI67*, *TOP2A*). Lastly, we report a cluster, ERN1, showing specific expression

154   of *ERN1* and *PLK2* genes that resemble activation patterns of exAM (*17*) (**Supplementary**

155   **Information**). In addition to microglial subtypes, we identified a PVM cluster, named CD163,

156   expressing a unique set of known PVM-specific markers, notably *CD163* and *F13A1*. The

157   CD163 cluster displayed a significant enrichment of genes involved in endocytic processes,

158   emphasizing its priming for receptor-mediated endocytosis and phagocytosis. While we

159 observe a close similarity between ADAM and PVM clusters (**Supplementary Fig. S2A**), we
160 found a clear separation between the two when we enriched for conserved murine disease-
161 associated microglia (DAM) signatures as well as human DAM signature from iPSC-derived
162 microglia (*5, 23–25*) (**Supplementary Fig. S3A**).
163   We further annotated myeloid subtypes by estimating the enrichment with polygenic risk
164 scores of heritable traits at single-cell resolution (scDRS; **Methods**; **Supplementary Fig. S3B,**
165 **Supplementary Table S15**). We extended the analysis to a set of the brain related diseases
166 beyond AD including schizophrenia (SCZ), bipolar disorder (BD), major depressive disorder
167 (MDD), autism spectrum disorder (ASD), multiple sclerosis (MS), amyotrophic lateral sclerosis
168 (ALS), and Parkinson's disease (PD). The polygenic risk scores for each trait were highly
169 reproducible between the FreshMG and PsychAD cohorts with AD and MS having the greatest
170 correlation (**Supplementary Fig. S3C**). The meta-analysis of both FreshMG and PsychAD
171 cohorts indicated that the 9 subtypes of myeloid cells were significantly associated with
172 heritable AD risk, which was the largest of all brain diseases followed by MS, SCZ, and MDD
173 (**Fig. 1E**). Notably, the GPNMB subtype had the widest coverage showing significant heritable
174 risks for all 8 diseases.
175
176 **Multi-modal validation of human myeloid taxonomy**
177   To show the utility of our annotation as the reference human myeloid taxonomy, we
178 validated the reproducibility of 13 myeloid subtypes using several independent datasets. First,
179 using a published human microglia dataset (*14*), we assessed the similarity of our taxonomy to
180 existing microglia annotations. While we found 8 of their microglial states, including their brain-
181 associated macrophage (BAM), resemble our subtypes (**Supplementary Fig. S3D**), the
182 alignments were moderate for the remaining 5 states. After re-annotating their nuclei using our
183 taxonomy as the reference (**Methods**), we confirmed the presence of all 13 subtypes (**Fig. 1G,**
184 **Supplementary Fig. S3G**). We also discovered the subtype composition was comparable to
185 our PsychAD snRNA-seq dataset (**Supplementary Figs. 2B-C**).
186   Since the taxonomy was established based on post-mortem tissues, we needed to ensure
187 the taxonomy was not biased for post-mortem effects, and it can be reproduced using living
188 brain tissues. Independent from the FreshMG and PsychAD cohorts, we generated an
189 additional scRNA-seq dataset, called LivingMG, from brain biopsies, which were obtained from
190 25 unique human donors (26 libraries; 97,828 cells after QC) diagnosed with spontaneous
191 intracerebral hemorrhage (ICH) (*26*). The brain tissue was collected during treatment and
192 processed in an identical manner to the fresh autopsy material. It's important to note that
193 cortical biopsy samples were obtained from a site distal to the site of the hemorrhage and, in
194 the absence of a secondary diagnosis, are considered neurotypical controls. We annotated
195 myeloid cells using the taxonomy derived from the FreshMG dataset and confirmed the
196 presence of all 13 subtypes in living cells. (**Fig. 1G**, **Supplementary Fig. S3E, S3J**).
197   Since the taxonomy was primarily derived from sc/snRNA-seq datasets, we utilized
198 different technology and modalities to confirm the robustness of our myeloid taxonomy. To
199 validate the spatial context, we conducted deep single-cell phenotyping and spatial analysis
200 using multiplexed imaging assay (Akoya PhenoCycler) and demonstrated, for example, PVMs

201 colocalize around blood vessels via staining for CD163 (**Fig. 1H**). Subsequently, we performed
202 spatial transcriptomic characterization using the Xenium *in situ* technology on 11 tissue slides
203 obtained from 8 individual donors (**Methods**). A custom panel of 366 genes, including both a
204 pre-designed human brain panel and additional markers for myeloid subtypes, was used to
205 further characterize the myeloid taxonomy (**Fig. 1I**). We showed the presence of 5 major
206 subclasses excluding the exAM, which was not expected to be present in cryosectioned tissue
207 (**Fig. 1G, Supplementary Figs. S3F, S4A-B**). While the resolution was limited in the Xenium
208 data, we were able to stratify robust subtypes via stability analysis (**Methods**) and validated the
209 presence of myeloid subtypes.
210 Lastly, we applied a multi-omic assay to further characterize the myeloid subtypes. We
211 employed CITE-seq, jointly quantifying the transcriptome and 154 unique cell-surface proteins,
212 to assess the preservation of the functional hierarchical structure at the protein-level. Using this
213 approach, we confirmed the presence of distinct proteomic patterns for each myeloid subtype
214 (**Supplementary Fig. S3K**). For example, within the homeostatic microglia subclass, the
215 CECR2 subtype expressed *CD99* and *ITGB3*, while the PICALM subtype expressed *CLEC4C*
216 and *TNFRSF13C* proteins as their markers. Likewise, the PVM cluster showed distinct surface
217 markers, *CD163* and *CCR4*, while the ADAM cluster was specific for *CD9* and *CD44* proteins.
218 In summary, we used both external and independent datasets, as well as multi-omic
219 modalities, to validate that the taxonomy is robust and consistent irrespective of the tissue
220 source.
221
222
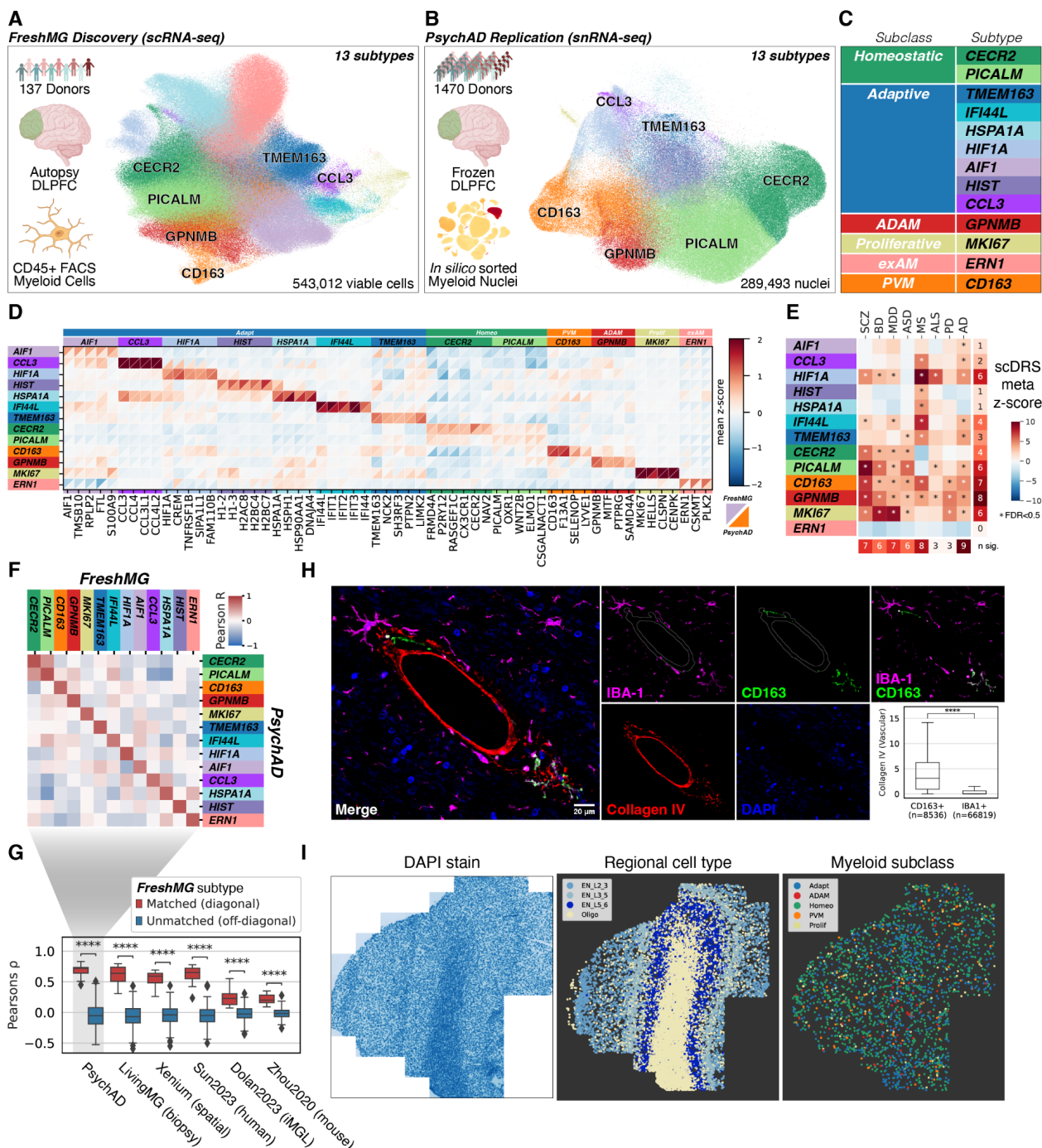
Figure 1. Overview of the human myeloid single-cell atlas. **(A)** the *FreshMG* discovery cohort (scRNA-seq) using live human myeloid cells from postmortem PFC and **(B)** the *PsychAD* replication cohort (snRNA-seq) using flash-frozen PFC tissues and *in-silico* sorted for microglia and PVMs. **(C)** Unified taxonomy of human myeloid subtypes. **(D)** Subtype-specific marker gene expression. Z-score normalized. Upper-triangle: *FreshMG*. Lower-triangle: *PsychAD*. **(E)** Enrichment of heritable disease risk (scDRS) by subtype using GWAS of 8 brain diseases. Meta-analysis between FreshMG and PsychAD. The asterisk denotes FDR < 0.05. SCZ: schizophrenia, BD: bipolar disorder, MDD: major depressive disorder, ASD: autism spectrum

232   disorder, MS: multiple sclerosis, ALS: amyotrophic lateral sclerosis, and PD: Parkinson's

233   disease. **(F)** Pairwise Pearson correlation of the subtype-level taxonomy between *FreshMG* and

234   *PsychAD* datasets using highly variable genes common in both datasets. **(G)** Validation of

235   human myeloid taxonomy using independent, multi-modal, and published datasets. Human

236   (*14*), iMGL: iPSC-derived microglia (*23*), and Mouse (*27*). Pairwise comparison of subtype-level

237   taxonomy against the FreshMG annotation. Mann–Whitney U test between matched (diagonal)

238   and unmatched (off-diagonal) subtypes. ****: $p \leq 1.0e-4$. **(H)** Representative image of Akoya

239   PhenoCycler multiplex immunofluorescence results showing CD163^{+}/IBA-1^{+} cells are enriched

240   near blood vessels (outlined by gray line), labeled by Collagen IV. Scale bar 20 μm. **(I)**

241   Representative slide of Xenium *in situ* spatial transcriptomics data. Left: DAPI, Middle: laminar

242   distribution of neuronal cell types, Right: distribution of myeloid cells annotated by subclasses.

243

244

Variation in human myeloid subtype composition on aging and AD

After determining 13 distinct subtypes of human brain myeloid cells, we examined the compositional variation of myeloid subtypes that are associated with aging in a subset of neurotypical donors who were free of dementia and diagnostic neuropathology from the FreshMG and PsychAD datasets. We normalized the subtype count ratio data using the centered log-ratio transformation and modeled using a linear mixed model, accounting for technical and demographic variables (**Methods**). Notably, the two homeostatic microglia subtypes displayed opposing trajectories with respect to aging (**Figs 2A left, D**). The CECR2 subtype showed progressive decline while the PICALM subtype showed a gradual increase with age. In addition, we saw an overall increase in the proportions of the ADAM and PVM subtypes with age. These findings were replicated using published human microglia snRNA-seq dataset (*14*) (**Supplementary Fig. S4C**). In contrast, we observed an age-related decline in the CCL3 subtype, indicating a possible reduction of chemotactic microglia in older brains. In parallel, we investigated sex-dependent variation in human myeloid subtypes, with or without taking age into consideration, but did not find any statistically significant compositional differences between males and females (**Figs. 2A middle, right**).

Next, we examined the variation of subtype composition during onset and progression of AD. To minimize the effect of younger brains, we limited the analysis to donors 40 years and older, resulting in a dataset composed of 134 donors from the FreshMG and 1,314 donors from the PsychAD cohort. We first evaluated the involvement of myeloid subtypes using the centered log-ratio transformed count ratio data after accounting for technical and demographic variables (**Methods**). Overall, irrespective of different measures of AD phenotypes (dx_AD, CERAD, Braak, and Dementia), we observed robust changes in subtype proportions in both FreshMG and PsychAD cohorts (**Fig. 2B**). Similar to normal aging, two homeostatic subtypes showed opposing trends, where the CECR2 subtype showed a progressive decline with increasing AD burden while the PICALM subtype showed a gradual increase. While the trends were observed during the early stages of AD, a more substantial divergence occurred after Braak stage 3 (**Fig. 2E**). Likewise, we observed a consistent increase in the proportion of the PVM subtype. The most notable difference in the compositional variation of AD phenotypes compared to aging was the GPNMB subtype. The GPNMB subtype was an outlier and showed the largest effect size across all 4 AD phenotypes, suggesting that proliferation of the GPNMB subtype is a hallmark of AD (**Fig. 2C**). We further supported our findings by replicating the compositional variation analysis with previously published data (*14*). Consistent with our findings, we observed the GPNMB subtype was increasing in proportion while Homeo_CECR2 was decreasing with severe AD neuropathology (**Supplementary Figs. S4C-E**).

**Causal mediation analysis of polygenic AD risk scoring and myeloid subtypes**

Having established that certain myeloid subtypes are enriched for AD genetic risk (**Fig. 1E**) and that their compositional landscape shifts in the presence of AD (**Fig. 2B**), we next sought to evaluate the association of per-cell polygenic AD risk scores with the compositional variation

286   observed in AD (`scDRS`; **Methods**, **Supplementary Fig. S3B**). We observed a positive

287   correlation (Pearson's r = 0.55) indicating that the ratio of subtypes with higher polygenic AD

288   risk scores increases in AD (**Fig. 2F; Supplementary Fig. S4F**). This also suggested heritable

289   risks might play a role in driving the compositional changes of myeloid subtypes.

290   Next, we leveraged our population-scale cohort to calculate per-donor AD polygenic risk

291   scores (PRS; **Methods**) and to assess how the interindividual variation in AD risk impact

292   changes in myeloid subtype composition (**Supplementary Fig. S3B**). The proportion of the

293   GPNMB subtype was significantly increased with AD PRS (**Supplementary Fig. S4G**). We

294   observed a similar compositional variation between AD phenotype (dx_AD) and PRS (**Fig. 2G**

295   **circle**), which was not driven by the AD status alone as the same compositional variation was

296   observed using a disease-free subset (**Fig. 2G triangle**).

297   To further dissect the relationships between genetic risk for AD and the observed changes

298   in GPNMB subtype composition, we conducted a series of causal mediation analyses using

299   the PRS as an instrumental variable (**Methods**). By examining the indirect effects of AD PRS on

300   the GPNMB subtype composition, we aimed to clarify whether the observed cellular changes

301   were driven by genetic predisposition or were a downstream consequence of AD pathology

302   (plaque). Our analysis revealed a significant indirect effect of AD PRS on the GPNMB subtype,

303   mediated through accumulation of Aβ plaques (Average Causal Mediated Effect (ACME) =

304   0.0254, 95%CI = [0.0137, 0.04], pval<2e-16). This indirect effect accounted for 60.5% of the

305   total effect (pval = 0.034). These findings suggest that the GPNMB subtype variation is more

306   likely a consequence of AD pathology. Furthermore, we observed a significant mediation effect

307   of the GPNMB subtype variation on severity of dementia (8.29% of the total effect mediated,

308   pval = 0.00096), suggesting that modification of this subtype via therapeutics could be a

309   feasible treatment strategy for AD.

310

311
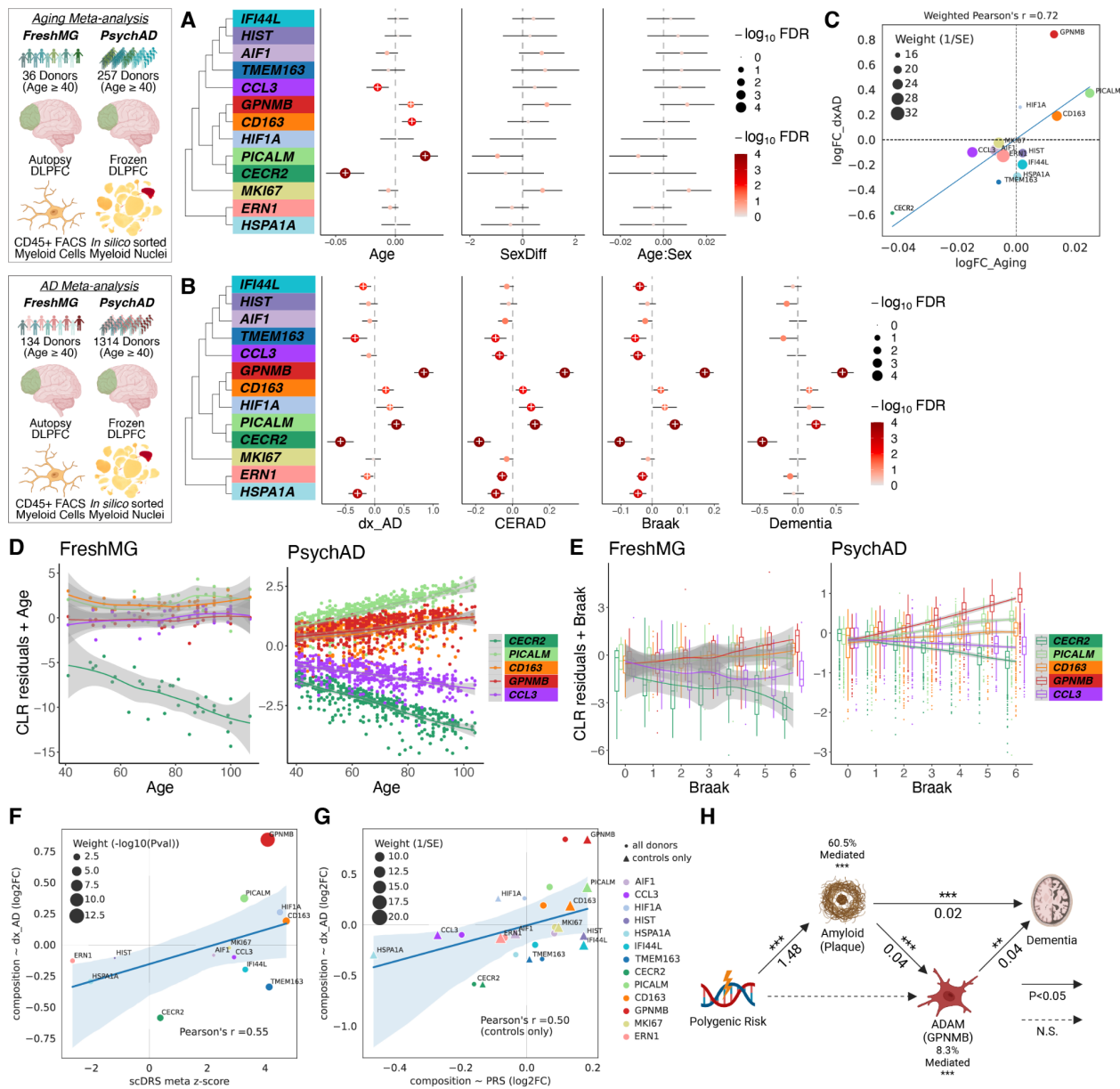
Figure 2. Variation in human myeloid subtype composition. **(A)** Compositional variation of myeloid subtypes by age, sex, and the interaction between age and sex using disease-free subset. CLR transformed composition data was modeled using a linear mixed model accounting for technical batch effects including tissue sources and sequencing pools and donor effects including age, sex, genetic ancestry, and PMI (see **Methods** on `crumblr`). Fixed effect meta-analysis using results from FreshMG and PsychAD cohorts. **(B)** Compositional variation of myeloid subtypes by four different neuropathological measures of the AD progression; diagnosis (dx_AD), CERAD, Braak staging, and dementia status, after accounting for technical and donor-level covariates. Fixed effect meta-analysis using both FreshMG and PsychAD cohorts. **(C)** Comparison of compositional variation between disease-free aging and AD. Subtypes were weighted by the inverse of standard error. **(D)** Covariate adjusted compositional variation with disease-free aging. CLR: centered-log-ratio. **(E)** Covariate

325   adjusted compositional variation with Braak staging. **(F)** Correlation between `scDRS` meta z-

326   scores and `crumblr` estimate of compositional variation by dx_AD as a coefficient. Weighted

327   Pearson's correlation using average -log10(P-value) as weights. **(G)** Correlation between

328   `crumblr` estimate of compositional variation by PRS as a coefficient against `crumblr`

329   estimate of compositional variation by dx_AD as a coefficient. Weighted Pearson's correlation

330   using inverse of average of standard error as weights. Circle denotes `crumblr` analysis using

331   all donors while triangle denotes `crumblr` analysis using controls only. **(H)** Causal mediation

332   analysis using PRS, Aβ plaque, composition of the GPNMB subtype, and clinical dementia

333   status. ***: p ≤ 1.0e-3, **: p ≤ 1.0e-2, NS: p > 0.05.

334

335

Variation in transcriptional regulation of human myeloid cells on aging and AD

336
337

338   We investigated the transcriptional regulation of human myeloid cells by examining the
339   differential gene expression patterns associated with normal aging, and during the onset and
340   progression of AD. In normal aging (**Supplementary Fig. S5A**), we discovered the increase in
341   expression of the *MS4A6A* gene, a member of the MS4A family of cell membrane proteins,
342   which are involved in the regulation of calcium signaling and have been implicated in
343   neurodegenerative processes (*28*). The age-related gene expression changes for both
344   homeostatic subtypes were enriched with actin filament-based process and actin cytoskeleton
345   organization pathways, supporting their proposed roles in cell adhesion and migration
346   (**Supplementary Fig. S5B**). The CD163 subtype was associated with the increase of cell
347   adhesion processes as well as pathways related to cell proliferation. The gene signatures in the
348   GPNMB subtype were enriched with immune response and activation. Overall, the increased
349   involvement of PVM and ADAM subclasses indicated an upregulation of inflammatory
350   responses in older individuals.
351   Next, we evaluated genes exhibiting differential expression patterns across four different
352   measures of AD phenotypes (dx_AD, CERAD, Braak, and Dementia) (**Fig. 3A**). Our analysis led
353   us to discover a set of AD-associated genes, including *PTPRG*, *DPYD*, and *IL15*, which
354   displayed upregulation across all phenotypes capturing more severe AD stages. Pathway
355   enrichment analysis revealed the PICALM and GPNMB subtypes share common pathways
356   related to the regulation of cell adhesion (**Supplementary Fig. S5C**). In contrast, both the
357   CECR2 and CD163 subtypes appear to be associated with negative regulation of cell
358   projection organization.
359   Given the strong compositional shifts and gene signatures for AD phenotypes, we tested
360   the presence of AD signatures in bulk microglia RNA-seq data (BulkMG; **Methods**). First, we
361   created myeloid subtype signatures from both the FreshMG and PsychAD datasets by
362   aggregating gene expression by subtype. We then compared the resulting subtype signatures
363   to BulkMG gene expression data, stratified by AD case and control status. Interestingly, the
364   Pearson correlation between subtypes and AD diagnosis clearly reflected the compositional
365   shifts we observed across multiple AD phenotypes (**Supplementary Fig. S5D**). The CECR2,
366   TMEM163, CCL3, and HSPA1A signatures closely correlated with the BulkMG from controls,
367   while the PICALM, CD163, GPNMB, and HIF1A signatures closely matched those from AD
368   cases. These results independently reproduce the observed changes in the myeloid
369   transcriptome during the onset and progression of AD.
370   To model the dynamic changes that take place during the onset and progression of AD at a
371   molecular level, we expanded our analysis from using discrete donor-level clinical variables to
372   a continuous pseudotime measure by ordering cells along a disease trajectory. We estimated
373   Braak-stage-informed ancestor-progenitor relations between observations through transport
374   maps between neighboring disease stages using Moscot (*29*). We then quantified cell-cell
375   transition probabilities, computed putative drivers, and constructed the disease-stage-
376   informed pseudotime with CellRank 2 (*30*) (**Supplementary Fig. S5E**; **Methods;**

377   **Supplementary Information**). As expected, we observed an increase in pseudotime with

378   disease progression (**Supplementary Fig. S5F**). Stratified by subtypes, we observed that

379   PICALM homeostatic microglia were assigned larger pseudotime values (late), compared to

380   CECR2 homeostatic cells (early; p-value < 0.001, **Supplementary Fig. S5G**), indicating their

381   association with disease progression and aligning with the compositional variation of AD

382   phenotypes observed earlier. To identify potentially critical stages in disease progression, we

383   compared changes in pseudotime across disease stages for each myeloid subtype (**Methods**).

384   This analysis revealed that the change was most pronounced starting from Braak stage 3

385   (**Supplementary Fig. S5H**), which was also the critical time point the subtype composition

386   diverged in AD.

387

388   **Upstream regulators of AD genes in human myeloid cells**

389   After identifying potential AD risk genes, we analyzed myeloid gene regulatory networks

390   (GRNs) to discover key upstream transcriptional regulators. Using SCENIC (*31, 32*), we

391   constructed GRNs based on expression data and known transcription factor (TF) binding

392   motifs and defined units of regulatory hierarchy (regulons) (**Fig. 3B, Supplementary Table**

393   **S12**). Subsequently, we assessed the enrichment of the regulon for each myeloid subtype

394   independently (**Supplementary Table S13**, **Methods**), revealing high concordance between

395   the FreshMG and PsychAD cohorts (**Fig. 3C**). We then derived combined regulon enrichment

396   scores using meta-analysis (**Methods**) and observed strong regulon subtype-specificity (**Fig.**

397   **3D**). The CECR2 and PICALM homeostatic subtypes were defined by enrichment of *KLF12*,

398   *GLIS3*, and *BACH2* regulons, while the PICALM, CD163, and GPNMB subtypes displayed

399   exclusive enrichment of *MITF* regulon. To link inferred regulons to differentially expressed AD

400   genes, we performed enrichment tests using 4 different types of AD risk signatures (**Methods**).

401   Notably, the target genes of *MITF*, *KLF12*, and *GLIS3* TFs were significantly associated with

402   AD risk profiles in the PICALM, CECR2, GPNMB, and HIF1A subtypes (**Fig. 3E**). *MITF* was

403   preferentially enriched with upregulated AD signatures, whereas *KLF12* and *GLIS3* were more

404   preferentially associated with downregulated AD signatures. Visualization of the joint *MITF-*

405   *KLF12-GLIS3* regulon network with AD risk genes revealed coordinated modulation of both up

406   and down-regulated candidate risk genes (**Fig. 3F**). These findings collectively suggest the

407   coordinated activity of *MITF*, *KLF12*, and *GLIS3* in regulating AD risk gene expression in

408   disease-associated microglia states. Functional enrichment analysis revealed that *MITF*,

409   *KLF12*, and *GLIS3* target genes were involved in key biological processes for microglia

410   function such as phagocytosis, cytokine production, and cellular response (**Supplementary**

411   **Fig. S6A**). Our findings that *MITF* distinctly regulates phagocytic-related pathways are in line

412   with previous findings from *in-vitro* models (*23*). In summary, by integrating differentially

413   expressed genes in AD with GRNs, we nominate *MITF*, *KLF12*, and *GLIS3* as potential

414   upstream master regulators of gene expression changes relevant to AD pathogenesis.

415

416   **Regulation of phagocytosis by MITF and GPNMB**

417   We prioritized *MITF* as a potential upstream regulator of AD-associated gene expression

418   critical for phagocytosis and the GPNMB subtype as the myeloid phenotype linked to AD. To

419   better understand the mechanistic relationship between them, we devised a lentiviral CRISPR
420   activation (CRISPRa) approach to activate genes in HMC3-VPR cell lines and measured the
421   level of phagocytosis under different substrate conditions (**Fig. 3G**). We first discovered that
422   the activation of *MITF* led to increased mRNA expression of *GPNMB* detected by qPCR but
423   not the other way around (**Supplementary Fig. S6D**), indicating that *MITF* is the upstream
424   regulator of *GPNMB* and validating our results using the GRN inference. Furthermore, we
425   observed that the activation of either *GPNMB* or *MITF* led to increased phagocytosis
426   regardless of substrate types **(Fig. 3H)**. Activating *MITF* was more effective at increasing
427   phagocytosis except under the myelin condition. When we added a drug (ML329) that inhibits
428   the *MITF* pathway, the phagocytosis was significantly reduced in all substrate conditions
429   (**Supplementary Fig. S6E**). Our results demonstrate the activation of phagocytosis requires a
430   cascade of regulatory events that involves *MITF* and *GPNMB* in AD.
431
432

Figure 3. Transcriptional regulation of human myeloid cells. **(A)** Differentially expressed genes
by four different measures of AD neuropathology adjusted for technical and donor-level
covariates. Fixed effect meta-analysis using both FreshMG and PsychAD cohorts. **(B)**
Schematic overview of GRN inference and TF-gene regulon enrichment for prioritization of

438   upstream master regulators of AD. **(C)** Concordance of normalized regulon activity scores

439   (AUCell) between FreshMG and PsychAD cohorts. Pairwise Pearson correlation. **(D)**

440   Enrichment of regulon by subtypes. Meta-analysis of consensus regulon enrichment Z-score

441   with Stouffer's correction between FreshMG and PsychAD cohorts. Top 3 regulons per each

442   subtype shown. **(E)** Enrichment of AD gene signatures by regulons. Fisher's exact tests for

443   enrichment of differentially expressed gene signatures in regulon target genes across myeloid

444   subtypes. **(F)** TFs that modulate AD risk genes. Gene regulatory network visualization of

445   *KLF12*, *MITF*, and *GLIS3* TFs and downstream target risk genes. Node colors represent gene

446   expression changes from `dreamlet` analysis. Edge weights represent importance scores

447   inferred from the SCENIC pipeline. **(G)** Schematic of phagocytosis assay. **(H)** Relative level of

448   phagocytosis after CRISPR activation in HMC3 cell line.

449

450

Non-cell-autonomous mechanisms affecting AD-associated microglia

To gain mechanistic insights into how different human myeloid subtypes communicate with each other and mediate AD risk through non-cell-autonomous mechanisms, we investigated the change of cell-to-cell interactions (CCIs) at different stages of AD using the LIANA framework (*33*) (**Supplementary Fig. S7A, Supplementary Table S14**). This approach allows us to dissect how myeloid cell signaling influences neighboring cells, potentially driving disease progression and highlighting targets for therapeutic intervention. For each individual, we inferred the magnitude, specificity, and directionality of cell-to-cell communication using gene expression profiles and known ligand-receptor interactions. We observed strong concordance between the magnitude of CCI activities from the FreshMG and the PsychAD cohorts (**Fig. 4A**), primarily for the homeostatic, PVM, and ADAM subtypes, whereas rare subtypes like MKI67 and CCL3 were less reproducible. By evaluating the CCI magnitude scores as a function of all 4 AD phenotypes using a linear mixed model, we identified differential CCIs associated with AD (**Fig. 4B, Supplementary Fig. S7B**), which were highly concordant across all 4 AD phenotypes (**Supplementary Fig. S7C**). We identified a total of 1,015 CCIs at FDR of 5% that were upregulated or downregulated in AD. The *APOE-SORL1* and *APOE-TREM2* interaction scores were higher in AD and were prioritized as the top AD-relevant CCIs, while *MRC1-PTPRC* interactions were down-regulated in AD. To test for genetic association, we performed the gene-set enrichment analyses on CCI pairs with increased scores in AD using GWAS data (*34*) (**Fig. 4C, Methods**). We observed AD-associated receptors had a strong association with AD risk but not with ligands. Visualizing the CCIs as directional networks in the context of different myeloid subtypes placed the GPNMB subtype as the most affected hub for CCIs that were upregulated in AD (**Fig. 4D**). Notably, the GPNMB subtype served as the receiving node for the *APOE-TREM2* interaction. To better understand the downstream effect of genes participating in AD-associated CCIs, we performed pathway enrichment analysis, uncovering that GPNMB-related CCIs were enriched with lipid metabolism and regulation of proteolysis (**Fig. 4E**).

TREM2-dependent regulation of phagocytosis by AD-associated microglia

Previous studies have shown that *TREM2*, a myeloid cell receptor, plays a crucial role in the activation of disease-associated microglia, with variants increasing AD risk (*5, 27, 35–40*). Given the higher expression of *APOE-TREM2* CCI in the GPNMB subtype, we hypothesized that GPNMB expansion in AD is partially *TREM2*-dependent. To investigate this hypothesis, we first examined the impact of highly penetrant *TREM2* variants for AD (R47H; rs75932628; n = 21 and R62H; rs143332484; n = 26) (*39*) on changes of the microglia subtype composition. We found that carriers of these *TREM2* mutations did not exhibit an expansion of the GPNMB subtype during progression of AD (**Fig. 4F**), supporting a potentially protective role of this subtype in phagocytosis and the amelioration of AD pathology. To further explore this, we utilized the published snRNA-seq dataset on Trem2-deficient 5XFAD mice (*27*) (**Fig.4G**). Similar to the human data, in the 5XFAD mouse model, we show an increase in the proportion of the GPNMB subtype, which was absent in the Trem2-deficient 5XFAD mice.

492 Finally, we utilized isogenic induced pluripotent stem cell (iPSC)-derived microglia that were
493 wild-type (WT), heterozygous (HZ), or homozygous (HO) for *TREM2*. *TREM2* knockout cells (HZ
494 and HO) showed approximately 50% lower *GPNMB* and *MITF* mRNA expression compared to
495 WT (**Supplementary Fig. S7D**). Phagocytosis assays using Aβ, myelin, and synaptic protein as
496 substrates revealed significant reduction in phagocytic activity for both HZ and HO lines
497 compared to WT (**Fig. 4I, Supplementary Fig. S7E**). Furthermore, inhibiting the *MITF* pathway
498 (with ML329) leads to a significant reduction in Aβ phagocytosis in WT cells. We used FACS to
499 separate microglia into high- and low-phagocytosing populations based on the fluorescence of
500 pHrodo-labeled substrates (**Fig. 4H, Supplementary Fig. S7F**). *GPNMB* protein levels were
501 higher in cells with high phagocytic activity (**Fig. 4J**). Similarly, RT-qPCR revealed that high-
502 phagocytosing cells exhibited higher levels of *GPNMB* mRNA than low-phagocytosing cells
503 across all substrate conditions.
504
505

Figure 4. Non-cell-autonomous mechanisms. **(A)** Concordance of CCI scores among human myeloid cells between the FreshMG and the PsychAD cohorts. Pairwise Spearman correlation

509   using aggregated CCI scores by subtype. Row labels correspond to the sender or ligand-

510   producing cell. Column labels correspond to the receiver or receptor-producing cell. **(B)**

511   Differential CCI analysis based on Braak stages. Meta-analysis of linear mixed model

512   regression using both FreshMG and PsychAD cohorts. Estimated log fold change corresponds

513   to increased representation in the high Braak stage (red) vs. the low Braak stage (blue). **(C)**

514   MAGMA enrichment analysis on differential CCI, stratified by direction of regulation (AD vs CTRL)

515   and role of interaction (ligands, receptors, or both). **(D)** Directed network visualization of the top

516   CCI pairs. Top: AD-associated, Bottom: controls-associated CCIs. Nodes represent each

517   subtype and directional edge weights represent the importance of interaction. The edge color

518   represents the estimated log fold change from differential CCI analysis. **(E)** Gene set

519   enrichment analysis of CCI pairs using Gene Ontology Biological Processes. CCIs aggregated

520   by subtype, direction of regulation (AD vs CTRL), and role of interaction (ligands or receptors).

521   The color scale represents the normalized enrichment score (NES). The dot size represents the

522   FDR significance. + marks FDR < 0.05. **(F)** Compositional variation of myeloid subtypes by AD

523   using *TREM2* missense mutation (R47H or R62H) carriers. Shared disease-free controls

524   without TREM2 mutations were compared against AD cases with *TREM2* WT (+/+) and *TREM2*

525   missense carriers (+/-). AD cases were sampled to match the size of *TREM2* mutation carriers.

526   **(G)** Compositional variation of myeloid subtypes by AD using Trem2-deficient 5XFAD mice.

527   Trem2+/+ 5XFAD and Trem2–/– 5XFAD mice were compared to disease-free control mice

528   (Trem2+/+). **(H)** Schematic of isolating highly phagocytosing microglial cells using flow

529   cytometry. **(I)** Relative level of phagocytosis among WT, *TREM2* heterozygous, and

530   homozygous knockouts in iPSC-derived microglia using Aβ as substrates. **(J)** Relative mRNA

531   expression of *GPNMB* measured by RT-qPCR for high and low phagocytosing microglia using

532   Aβ as substrates.

533

534

Discussion

535

536   The cell atlas presented here underscores the importance of the functional plasticity of
537 human myeloid cells throughout life, reflecting their ability to dynamically adapt to their
538 microenvironment. Our comprehensive analyses uncover striking similarities between normal
539 aging and AD pathology. We speculate that the natural aging process is accelerated in AD, and
540 follows a similar trend for all subtypes, with the exception of the AD-associated microglia,
541 ADAM. ADAM is characterized by elevated expression of *GPNMB* transcripts and *CD44*
542 protein. *GPNMB* is a multifaceted transmembrane protein involved in the regulation of
543 inflammation and is implicated in several neurodegenerative diseases (*41–45*). When cleaved
544 by proteases into its soluble form, *GPNMB* signals by binding to the *CD44* receptor to drive
545 anti-inflammatory responses (*42*, *46*, *47*). Based on the following three main outcomes, our
546 results collectively suggest that ADAM is involved in anti-inflammatory responses and confer
547 neuroprotective benefits in AD.
548   First, ADAM shows a marked increase in prevalence with AD progression and correlates
549 significantly with polygenic AD risk scores. It suggests that individuals with higher AD genetic
550 predisposition may naturally exhibit increased activation of this subtype, positioning it as a
551 potential biomarker for disease progression and reflecting an adaptive, though limited,
552 neuroprotective response to neurodegenerative changes. This is consistent with small-scale
553 studies supporting *GPNMB* as a cerebrospinal fluid biomarker for the early diagnosis and
554 prognosis of AD (*48*, *49*). The significant increase in ADAM, driven by polygenic AD risk and
555 mediated by Aβ accumulation, reveals the intricate interplay between genetic predisposition
556 and cellular responses during AD progression. This association underscores the potential for
557 targeted therapeutic strategies that modulate the ADAM subtype, potentially altering disease
558 progression by mitigating the downstream effects of Aβ accumulation.
559   Second, we investigated cell-intrinsic factors that distinguish transcriptomic profiles
560 between AD cases and controls. Through GRN analysis, we prioritized *MITF* as the master
561 regulator of AD risk signatures, governing the expression of numerous AD-associated genes,
562 including *APOE*, *DPYD*, *TREM2*, and *PTPRG* (*12*, *50*, *51*). The *MITF* network is notably enriched
563 with markers of phagocytic activity and has been recognized as a crucial regulator of
564 homeostatic microglial functions, particularly in promoting autophagic states and enabling
565 microglia to migrate, detect, and clear Aβ/Tau proteinopathies (*22*, *23*, *52–54*). We confirmed
566 that *MITF* is the upstream regulator of *GPNMB* and demonstrated that the activation of
567 *GPNMB* is linked to increased phagocytosis. Prior work demonstrating the expression of
568 *GPNMB* is dependent on phagocytosis of CNS-substrates (*23*), indicative of a positive
569 feedback loop between *GPNMB* expression and phagocytosis.
570   Third, we examined non-cell-autonomous mechanisms that distinguish interactions and
571 communication pathways influencing AD progression. The significant enrichment of AD genetic
572 risk loci (*APP*, *TREM2*, *SORL1*, *SORT1*, *ABCA1*, *TSPAN14*) within the prioritized receptors of
573 AD-associated CCIs suggests potential mechanisms behind their contribution to AD. We
574 prioritize ADAM as a central hub in AD progression, participating in the highest number of AD-
575 associated ligand-receptor interactions among microglia subtypes. Motivated by the AD-
576 associated upregulation of *APOE-TREM2* ligand-receptor interactions in ADAM, we

577   subsequently found that *TREM2* mutations diminish ADAM microglia, highlighting the

578   dependency of this subtype on *TREM2* function. Corroborating previous observations (*23*, *35*),

579   we demonstrate that phagocytosis is *TREM2*-dependent and regulated through *MITF*-

580   mediated activation of *GPNMB*, reinforcing the importance of this pathway in maintaining

581   microglial function and neuroprotection.

582   In conclusion, our study advances the field by providing a high-resolution view of human

583   myeloid cell diversity and their adaptive roles in aging and AD. The identification of subtype-

584   specific GRNs, including the *MITF-GPNMB* axis, that are *TREM2*-dependent, highlights

585   promising therapeutic avenues for modulating microglial functions to potentially slow disease

586   progression. Future studies should aim to validate these pathways in humanized models and

587   explore pharmacological strategies that enhance neuroprotective myeloid subtypes, potentially

588   altering the trajectory of AD and related diseases.

589

Methods

Sources and description of human biosamples

All brain specimens were obtained through informed consent via brain donation programs at the respective organizations. All procedures and research protocols were approved by the respective ethical committees of our collaborator's institutions. The FreshMG samples (n = 137) were taken from 96 fresh postmortem autopsy samples obtained at the Mount Sinai/JJ Peters VA Medical Center NIH Brain and Tissue Repository (NBTR) in the Bronx, NY. An additional set of 41 fresh postmortem autopsy samples was obtained from participants in the Religious Orders Study or Rush Memory and Aging Project (ROSMAP) at Rush Alzheimer's Disease Center (RADC) in Chicago, IL. Both studies were approved by an Institutional Review Board of Rush University Medical Center and all participants signed informed and repository consents and an Anatomic Gift Act (55). The PsychAD cohort comprises 1,470 donors from three brain banks, Mount Sinai NIH Brain Bank and Tissue Repository (MSSM; 1,023 samples), NIMH Human Brain Collection Core (HBCC; 295 samples), and ROSMAP (RUSH; 152 samples). Finally, LivingMG biopsies were collected from patients undergoing procedures for intracerebral hemorrhage evacuation (STUDY-18-01012A), as described previously (9).

Collection and harmonization of clinical, pathological, and demographic metadata

Since the brain tissue specimens were collected from three different sites, the available clinical data varies as a function of source. As such, we used the following scheme to harmonize available clinical, pathological, and demographic metadata: the CERAD scoring scheme for neuritic plaque density (19) was harmonized for consistency across multiple brain banks, where the scores range from 1 to 4, with increasing CERAD number corresponding to an increase in AD burden; 1 = no neuritic plaque (normal brain), 2 = sparse (possible AD), 3 = moderate (probable AD), 4 = frequent (definite AD). Samples from ROSMAP used consensus summary diagnosis of no cognitive impairment (NCI), mild cognitive impairment (MCI), and dementia and its principal cause, Alzheimer's dementia (56–58). MSSM/VA samples used clinical dementia rating (CDR), which was based on a scale of 0-5; 0 = no dementia, 0.5 = questionable dementia (very mild), 1 = mild dementia, 2 = moderate dementia, 3=severe dementia, 4 = profound dementia, 5 = terminal dementia. After consulting with clinicians, we created a harmonized ordinal variable where dementia is categorized into three levels of cognitive decline, independent of AD diagnosis; 0 = no cognitive impairment, 0.5 = MCI (mild cognitive impairment), and 1 = dementia. In addition to AD phenotype, we collected comprehensive demographic (age, sex, and genetic ancestry) and technical variables (brain bank, sequencing facility, sequence pooling information, postmortem interval (PMI; measured in minutes), APOE genotype) to describe each cohort (**Supplementary Fig. S1**, **Supplementary Table S3-4**).

Clinical diagnosis of AD

For analysis comparing donors with AD cases and neurotypical controls, a binary clinical diagnosis variable for AD, **dx_AD**, was defined as follows. Individuals with CERAD 2, 3, or 4, Braak ≥ 3, and CDR ≥ 1 for MSSM/VA or Alzheimer's dementia for ROSMAP were classified as AD cases. Controls were defined as individuals with CERAD 1 or 2 and Braak 0, 1, or 2.

Measuring AD neuropathology

For analysis comparing donors with pathologic AD, the following variables were used to measure the severity of AD neuropathology. **CERAD score** (*19*). A quantitative measure of Aβ plaque density where 1 is normal, 2 is possible AD, 3 is probable AD, and 4 is definite AD (*56*). **Braak AD-staging score** measuring progression of neurofibrillary tangle neuropathology (Braak & Braak-score, or BBScore). A quantitative measure of the regional patterns of neurofibrillary tangle (NFT) density across the brain, where 0 is normal and asymptotic, 1-2 indicate initial stages where NFT begins to appear in the locus coeruleus and the transentorhinal region, 3-4 indicate progression to limbic regions, such as the hippocampus and amygdala, and 5-6 indicate NFT are widespread, affecting multiple cortical regions (*59–61*).

Measuring cognitive impairment

For analysis comparing donors with AD-related dementia, the following variable was used to measure the severity of cognitive impairment. **Clinical assessment of dementia.** A harmonized variable of cognitive status based on CDR scale for MSSM/VA or NCI, MCI, Alzheimer's dementia for ROSMAP. We used the three-level ordinal categories of clinical dementia to measure the severity of dementia, in which 0 indicates no dementia, 0.5 indicates minor cognitive impairment, and 1.0 indicates definite clinical dementia.

Isolation and fluorescence-activated cell sorting (FACS) of microglia from fresh brain specimens (FreshMG and LivingMG)

Fresh brain tissue specimens were placed in tissue storage solution (Miltenyi Biotech, #130-100-008) and stored at 4 ˚C for ≤ 48hrs before processing using the Adult Brain Dissociation Kit (Miltenyi Biotech, #130-107-677), according to the manufacturer's instructions. RNase inhibitors (Takara Bio, #2313B) were used throughout cell preparation. Following de-myelination (Miltenyi Myelination removal beads - Miltenyi Biotech, #130-096-433) cells were incubated in antibody (CD45: BD Pharmingen, Clone HI30, #555483 and CD11b: BD Pharmingen, Clone ICRF44, #560914) at 1:500 for 1 hour in the dark at 4 ˚C with end-over-end rotation. Prior to fluorescence-activated cell sorting (FACS), DAPI (Thermoscientific, #62248) was added to facilitate the selection of viable cells. Viable (DAPI negative) CD45/CD11b positive cells were isolated by FACS using a FACSAria flow cytometer (BD Biosciences). Following FACS, cellular concentration and viability were confirmed using a Countess automated cell counter (Life technologies).

Isolation and fluorescence-activated nuclear sorting (FANS) of nuclei from frozen brain specimens (PsychAD), with hashing

All buffers were supplemented with RNAse inhibitors (Takara, #2313B). 25 mg of frozen postmortem human brain tissue was homogenized in cold lysis buffer (0.32 M Sucrose, 5 mM $CaCl_2$, 3 mM Magnesium acetate, 0.1 mM, EDTA, 10 mM Tris-HCl, pH8, 1 mM DTT, 0.1% Triton X-100) and filtered through a 40 µm cell strainer. The flow-through was underlaid with sucrose solution (1.8 M Sucrose, 3 mM Magnesium acetate, 1 mM DTT, 10 mM Tris-HCl, pH8) and centrifuged at 107,000 g for 1 hour at 4 ℃. Pellets were resuspended in PBS supplemented with 0.5% bovine serum albumin (BSA). 6 samples were processed in parallel. Up to 2 M nuclei from each sample were pelleted at 500 g for 5 minutes at 4 ℃. Nuclei were re-suspended in 100 µl staining buffer (2% BSA, 0.02% Tween-20 in PBS) and incubated with 1 µg of a unique TotalSeq-A nuclear hashing antibody (Biolegend) for 30 min at 4 ℃. Prior to FANS, volumes were brought up to 250 µl with PBS and 7aad (Invitrogen, #00-6993-50) added according to the manufacturer's instructions. 7aad positive nuclei were sorted into tubes pre-coated with 5% BSA using a FACSAria flow cytometer (BD Biosciences).

scRNA-seq and CITE-seq library preparation (FreshMG and LivingMG)

Following FACS, 10,000 cells were processed using 10x Genomics single cell 3' capture reagents (10x Genomics, #1000268), according to the manufacturer's instructions. In parallel, CITE-seq was performed on a subset of samples (n = 3 donors, n = 8 replicates per donor) using the TotalSeq™-A Human Universal Cocktail (BioLegend, #399907) with 154 unique cell surface antigens, including principal lineage antigens, and includes 9 isotype control antibodies to survey surface antigens. CITE-seq was performed according to the manufacturer's instructions. For the CITE-seq experiment, a total of 80,000 cells were loaded on 10x Genomics B chips (10,000 of each uniquely barcoded sample aliquot per B chip lane), with a total targeted recovery of around 40,000 cells.

snRNA-seq and hashing library preparation (PsychAD)

Following FANS, nuclei were subjected to 2 washes in 200 µl staining buffer, after which they were re-suspended in 15 µl PBS and quantified (Countess II, Life Technologies). Concentrations were normalized and equal amounts of differentially hash-tagged nuclei were pooled. A total of 60,000 (10,000 each) pooled nuclei were processed using 10x Genomics single cell 3' v3.1 reagents (10x Genomics, #1000268). Each pool was run across x2 10x Genomics lanes to create a technical replicate. At the cDNA amplification step (step 2.2) during library preparation, 1 µl 2 µm HTO cDNA PCR "additive" primer v3.1 was added (*62*). After cDNA amplification, supernatant from 0.6x SPRI selection was retained for HTO library generation. cDNA library was prepared according to the 10x Genomics protocol. HTO libraries were prepared as previously described(*62*). cDNA and HTO libraries were sequenced at NYGC using the Novaseq platform (Illumina).

Processing of scRNA-seq data (FreshMG and LivingMG)

710
711 We developed a tracking platform to record all technical covariates (such as 10x Genomics
712 kit lotnumber, dates of different preparations, viable cell counts, etc.) and quality metrics
713 derived from data preprocessing. **Alignment**. Paired-end scRNA-seq reads were aligned to the
714 hg38 reference genome and the count matrix was generated using 10x cellranger count
715 (v7.0.0). Subsequently, we used the CellBender (*63*) to carefully separate out true cells from
716 empty droplets with ambient RNA from raw unfiltered cellranger output. **QC**. We performed the
717 downstream analysis by aggregating gene-count matrices of multiple samples. A battery of QC
718 tests was performed to filter low-quality libraries and non-viable cells within each library using
719 Pegasus (v1.7.0)(*64*). Viable cells were retained based on UMI ($1{,}000 \leq$ n_UMI $\leq 40{,}000$), gene
720 counts ($500 \leq$ n_genes $\leq 8{,}000$), and percentage of mitochondrial reads (percent_mito ≤ 20).
721 We also checked for possible contamination from ambient RNA, a fraction of reads mapped to
722 non-mRNA like rRNA, sRNA, pseudogenes, and known confounding features such as lncRNA
723 MALAT1. Further filtering was carried out by removing doublets using the Scrublet method
724 (*65*). After filtering, the retained count matrix was normalized and log-transformed. Batch
725 correction. We assessed the correlation between all pairs of technical and biological variables
726 using Canonical Correlation Analysis and used the Harmony method (*66*) to regress out
727 unwanted confounding variables such as the source of brain tissue. Clustering. From the kNN
728 graph calculated from the PCA, we clustered cells in the same cell state using Leiden (*67*)
729 clustering. We use UMAP (*68*) for the visualization of resulting clusters. Cells identified as T
730 cells, NK cells, monocytes, neutrophils, oligodendrocytes, and astrocytes were removed, and
731 those identified as microglia and PVMs were carried forward for subsequent taxonomic
732 analysis. **Annotation of LivingMG**. After subsetting the data for microglia and PVMs, we used
733 myeloid taxonomy from the FreshMG dataset as reference to annotate the LivingMG dataset.
734 We used the same set of highly variable genes from the FreshMG dataset and employed
735 scANVI (*69*) to transfer both subclass and subtype level annotations (**Supplementary Fig.**
736 **S3J**).
737
738 **Processing of snRNA-seq data (PsychAD)**
739 **Alignment**. Samples were multiplexed by combining 6 donors in each nuclei pool using
740 hashing, and each biosample was processed in duplicate to produce technical replicates.
741 Paired-end snRNA-seq libraries were aligned to the hg38 reference genome using STAR solo
742 (*70, 71*) and multiplexed pools were demultiplexed using genotype matching via vireoSNP (*72*).
743 After per-library count matrices were generated, the downstream processing was performed
744 using pegasus v1.7.0 (*64*) and scanpy v1.9.1 (*73*). **QC**. We applied rigorous three-step QC to
745 remove ambient RNA and retain nuclei for subsequent downstream analysis. First, the QC is
746 applied at the individual nucleus level. A battery of QC tests was performed to filter low-quality
747 nuclei within each library. Poor-quality nuclei were detected by thresholding based on UMI
748 ($1{,}179 \leq$ n_UMI $\leq 200{,}000$; determined based on median absolute deviation of n_UMI
749 distribution), gene counts ($986 \leq$ n_genes $\leq 15{,}000$; determined based on median absolute
750 deviation of n_genes distribution), and percentage of mitochondrial reads (percent_mito ≤ 1).
751 We also checked for possible contamination from ambient RNA, the fraction of reads mapped

752   to non-mRNA like rRNA, sRNA, and pseudogenes, as well as known confounding features,

753   such as the lncRNA MALAT1. Second, the QC was applied at the feature level. We removed

754   features that were not robustly expressed in at least 0.05% of nuclei. Lastly, the QC was

755   applied at the donor level. We removed donors with very low nuclei counts, which can

756   introduce more noise to the downstream analysis. We also removed donors with low genotype

757   concordances. Further filtering was carried out by removing doublets using the Scrublet

758   method (*65*). **Batch correction**. We assessed the correlation between all pairs of technical

759   variables using Canonical Correlation Analysis and used the Harmony method (*66*) to regress

760   out unwanted variables such as the effect of brain tissue sources. **Clustering**. Highly variable

761   features were selected from mean and variance trends, and we used the k-nearest-neighbor

762   (kNN) graph calculated on the basis of harmony-corrected PCA embedding space to cluster

763   nuclei in the same cell type using Leiden (*67*) clustering algorithms. We used UMAP (*68*) for the

764   visualization of the resulting clusters. **Isolation of myeloid cells**. Identified cell-type clusters

765   were annotated based on manual curation of known gene marker signatures obtained from

766   Human Cell Atlas and human DLPFC study (*74*). Classes of immune cells, including Microglia

767   and PVM, were isolated and subjected to myeloid subtype annotation and downstream

768   analysis.

769

770   **Processing of bulk RNA-seq data (BulkMG)**

771   RNA was extracted from aliquots of up to 100,000 FACS-sorted CD45+ microglia using the

772   Arcturus PicoPure RNA isolation kit (Applied Biosystems). RNA-sequencing libraries were

773   generated using the SMARTer Stranded Total RNA-Seq Kit v2 (Takara Bio USA, #634411).

774   Libraries were quantified by Qubit HS DNA kit (Life Technologies, #Q32851) and by quantitative

775   PCR (KAPA Biosystems, #KK4873) before sequencing on the Hi-Seq2500 (Illumina) platform

776   obtaining 2x100 paired-end reads.

777   Count matrices were generated using Kallisto pseudo-mapping (*75*) using the standard

778   Genecode v38 reference (starting with 235,227 transcripts for 60,535 unique genes). For gene-

779   level analyses, 21,856 features were retained for downstream analyses after filtering for

780   features with CPM > 1 in at least 15% of samples. Correct identity of the samples was

781   confirmed by concordance between the genetic variants obtained from RNA-seq with those

782   obtained from ATAC-seq, or directly available genotypes, as available.

783

784   **Spatial validation using Akoya PhenoCycler**

785   FFPE sections from both AD and control cases were used for the Akoya PhenoCycler

786   experiment. The experiments were performed according to the manufacturer's protocol, with

787   the Neuroinflammation Module, Neuroscience Core Panel and Immune Module provided by

788   Akoya. Briefly, samples were deparaffinized and hydrated. For antigen retrieval, samples were

789   boiled in Tris-EDTA pH 9 for 20 minutes in a programmable pressure cooker. Samples were

790   stained in Antibody Cocktail Solution containing antibodies (**Supplementary Table S5**) and

791   PhenoCycler Blocking Buffer. Following staining, samples were washed, fixed, and loaded on

792   the PhenoCycler, with data generated using the automatic workflow. Akoya PhenoCycler

793   results were saved as .qpproj files. and protein expression quantified using QuPath (*76*). After

794   the sections were annotated, cells were segmented with the QuPath extension StarDist

795   fluorescent cell detection script, with dsb2018_paper.pb as a training model. Protein

796   expression was quantified using raw channel intensity with spatial boundaries of cells inferred

797   by export measurement and export detection commands using QuPath.

798

799   **Spatial transcriptomic characterization using Xenium *in situ***

800   **Custom panel design**. Xenium Human Brain Gene Expression Panel (10x Genomics,

801   #1000599) and a custom panel of 100 genes (**Supplementary Table 16**) were selected for the

802   Xenium experiment. The 100-gene custom panel consisted mainly of subclass markers

803   selected based on specificity and gene expression level. The custom gene list was sent to 10X

804   genomics and the probe design was performed using their in-house pipeline. **Tissue**

805   **preparation**. Fresh frozen tissue specimens of DLPFC were dissected into small blocks on ice.

806   Tissue blocks were snap frozen by submerging in an isopentane (Sigma-Aldrich, #320404-1L)

807   bath chilled with dry ice and stored at -80 ℃. Before cryosectioning, tissue blocks were

808   allowed to equilibrate to the cryostat (Microm, #HM505) chamber temperature, and were

809   mounted with OCT (Tissue-Tek® O.C.T. Compound, Sakura Finetek USA, #4583). After

810   trimming, good quality 10 µm sections were flattened on the cryostat stage and placed on pre-

811   equilibrated Xenium slides (Xenium Slides & Sample Prep Reagents, 10x Genomics,

812   #1000460). 2-3 sections were placed on each slide. Sections were further adhered to by

813   placing a finger on the backside of the slide for a few seconds and were then refrozen in the

814   cryostat chamber. Slides were sealed in 50 ml tubes and stored at -80℃ until Xenium sample

815   preparation. **Sample preparation**. Xenium sample preparation was performed according to the

816   manufacturer's protocol; "*Xenium In Situ for Fresh Frozen Tissues – Fixation &*

817   *Permeabilization, CG000581, Rev C*" and *"Xenium In Situ Gene Expression - Probe*

818   *Hybridization, Ligation & Amplification, User Guide, CG000582, Rev C*''. Briefly, fresh frozen

819   sections mounted on Xenium slides from the previous step were removed from -80 ℃ storage

820   on dry ice prior to incubation at 37 ℃ for 1 min. Samples were then fixed in 4%

821   paraformaldehyde (Formaldehyde 16% in aqueous solution, VWR, #100503-917) in PBS for 30

822   min. After rinsing in PBS, the samples were permeabilized in 1% SDS (sodium dodecyl sulfate

823   solution) for 2 min and then rinsed in PBS before being immersed in the pre-chilled 70%

824   methanol and incubated for 60 min on ice. After rinsing the samples in PBS, the Xenium

825   Cassettes were assembled on the slides. Samples were incubated with a probe hybridization

826   mix containing both the Xenium Human Brain Gene Expression Panel (10x Genomics,

827   #1000599) and the 100 custom gene panel at 50 ℃ overnight to allow the probes to hybridize

828   to targeted mRNAs. After probe hybridization, samples were rinsed with PBST, and incubated

829   with Xenium Post Hybridization Wash Buffer at 37 ℃ for 30 min. Samples were then rinsed with

830   PBST and a ligation mix was added. Ligation was performed at 37 ℃ for 2 hrs to circularize the

831   hybridized probes. After rinsing the samples with PBST, Amplification Master Mix was added

832   to enzymatically amplify the circularized probes at 30 ℃ for 2 hrs. After washing with TE buffer,

833   auto-fluorescence was quenched according to the manufacturer's protocol and nuclei stained

834   with DAPI prior to Xenium *in situ* analysis. Nuclear segmentation. The prepared samples were

835   loaded into the Xenium analyzer and run according to manufacturer's instructions "*Xenium*

836   *Analyzer User Guide CG000584 Rev B*". After the Xenium analyzer was initiated, the correct
837   gene panel was chosen, and decoding consumables (Xenium Decoding Consumables, 10x
838   Genomics, #1000487) and reagents (Xenium Decoding Reagents, 10x Genomics, #1000461)
839   were loaded. The bottom of the slides was carefully cleaned with ethanol prior to loading. Once
840   the samples were loaded and the run was initiated, the instrument scanned the whole sample
841   area of the slides using the DAPI channel, and regions of interest were selected to maximize the
842   capture area. Results were generated by the instrument using default settings. By default, the
843   Xenium analyzer uses 15 µm nuclei expansion distance for segmentation of cells. To test the
844   idea of nuclei only segmentation, we resegment the results with 0 µm nuclei expansion, by
845   using the Xenium ranger and the following scripts:

```
846  xeniumranger resegment --id=demo --xenium-bundle=/path/to/xenium/files
847  --expansion-distance=0 --resegment-nuclei=True
```

848   **Identification of myeloid cells**. After generating the cell-by-gene count matrices based on
849   nuclear segmentation, nuclei were filtered by the number of detected transcripts (n_counts ≥
850   30). The count matrices from all samples were merged, log-normalized, and subjected to PCA,
851   kNN graph calculation, and Leiden clustering. To assign major cell type labels to each cell, we
852   combined this unsupervised clustering approach with supervised label transfer with scANVI
853   (*69*). In short, nuclei from the RADC dataset (a subset of the full PsychAD study) with known
854   labels for eight major CNS cell types and 27 subclass labels were used as a reference to
855   assign labels to all cells in the unfiltered Xenium dataset. Then, we assigned labels to each
856   Leiden cluster according to the following criteria - any cluster containing >90% of cells with a
857   single label was assigned that label; all other clusters were removed from further analysis. In
858   addition, cells within retained clusters were removed if their individual scANVI label did not
859   match the label assigned to their cluster. To retain a pure microglia and PVM nuclei population,
860   we first filtered the Xenium data for the Immune class. This population was further filtered
861   based on the label transfer of PsychAD subclasses, to retain only nuclei with the "Microglia"
862   and "PVM" subclass labels. This filtered data (~24,000 nuclei) was then re-processed and
863   normalized up to PCA computation, followed by integration with batch correction using
864   harmony (*66*), with the batch label set as the ID of the Xenium slide (each slide contained 2-3
865   tissue samples), and corrected for variation in the number of detected transcripts per nucleus.
866   The top 30 harmony-corrected PCs were then used for neighbor graph calculation, UMAP
867   visualization, and Leiden clustering. **Taxonomy of myeloid cells**. To identify subtypes of
868   myeloid cells in the Xenium data, we relied on the scANVI label transfer method. We used the
869   PsychAD cohort as a reference since we expected it to be more similar to our Xenium data
870   than the FreshMG cohort (since the PsychAD cohort was also frozen *in situ*, and contains only
871   nuclear transcripts). Label transfer was performed for subclass (subtype) annotation as
872   described below. However, due to the high degree of transcriptional similarity between
873   microglia sub-populations, as well as the relative sparsity of measured informative genes, we
874   adopted a more stringent approach and assigned microglia subclass (subtype) labels based on
875   the stability of obtained predictions. We ran scANVI for subclass (subtype) label transfer 23 (21)
876   independent times, differing only by a randomly generated initial condition. Then, we defined

877 stably-predicted nuclei as those that had 17 (16) predictions in internal agreement, and
878 assigned "unstable" labels to nuclei whose combined predictions did not fulfill this condition.
879 Subclass predictions were subsequently refined to obtain stable subtype prediction by
880 subsetting the dataset to Homeo (or Adapt) stably predicted nuclei and running 10
881 independent subtype-level predictions per subset, with predictions being accepted as stable
882 with 8 or more consistent "votes". **Consensus subclass and subtype labels from stability**
883 **analysis.** To further strengthen the reliability of our predictions, we attempted to combine our
884 microglia subclass and subtype prediction into a single consensus. Of note, consensus labels
885 could be either at the subclass or subtype level, depending on the set of predicted labels
886 obtained for a given nucleus. Our consensus voting process began by assigning pseudo-
887 subclasses to nuclei from the subtype predictions, by asking whether at least 16 (out of 21)
888 subtype predictions agree for a given nucleus at the subclass level (even if the subtype
889 prediction was "unstable"). Next, cells were assigned a subclass label if the 2 subclass
890 predictions did not contradict each other (i.e., they either agreed, or one method had a stable
891 prediction and the other was unstable). Cells with stable subclass predictions by this
892 methodology were then further assigned a subtype if their subtype predictions were similarly
893 stable and consistent. Based on these criteria, ~76% of microglia were stably assigned a
894 subclass. Subtype annotation, however, proved more challenging, and many cells were not
895 stably assigned to a single subtype in this analysis. **Label transfer from snRNA-seq data**
896 **using scANVI.** Throughout this work, we utilize scANVI to perform reference-based label
897 transfer as a way to assist in identifying pre-defined populations on cells. In each such
898 instance, we performed the following steps. First, snRNA-seq gene expression data was
899 subset to the genes also measured in our Xenium data. Next, we used the scvi-tools package
900 (*77, 78*) to train machine learning models for dimensionality reduction based on the reference
901 dataset and its assigned labels (e.g., class and subclass labels from the PsychAD cohort).
902 Unless stated otherwise, model training was run with the following parameters. scVI models
903 were run with 5 layers and 20 latent variables (30 for microglia sub-populations) and were
904 trained for 50 (75) epochs; scANVI models were trained for 50 epochs with a minimal sample of
905 100 cells per cluster per epoch; transfer models were trained for 100 epochs. Following
906 training, the model was applied to query Xenium data to assign labels. To assess the
907 performance of each transfer model, we performed a "self label transfer", predicting labels in
908 the reference data (using the subset gene pool) and evaluated the rate of correct prediction
909 and biases in label misassignment for each predicted category. Where appropriate, we also
910 computed the Pearson correlation coefficients for gene expression between the reference and
911 query data, limited to the shared subset of genes across predicted labels.
912

913 **Preparation of phagocytosis substrates**
914   **Myelin**. Human myelin was isolated from human brain tissue using a modified protocol (*23,*
915 *79*). Dissecting media [RPMI (Sigma, #R8758), 10% FBS (Avantor, #97068-091), 0.4 mg/mL
916 collagenase (Sigma, #10269638001), 2 mg/mL DNAse I (Sigma, #10104159001)] was
917 preheated in a 12-well tissue culture plate (Corning, #3513) in a 37 ˚C incubator. Using a
918 scalpel, 75-125 mg of human brain white matter was minced and transferred to the preheated

919   dissecting media and incubated at 37 ℃ for 30 minutes, pipetting the solution after 15 minutes.
920   After 30 minutes, brain homogenate was transferred to a 2 mL Dounce homogenizer (Kimble,
921   #885302) on ice, homogenized, sieved using a 40 μm cell strainer (Greiner, #542040) and
922   transferred to a 15 mL conical tube. The homogenate was centrifuged at 400 x g for 10
923   minutes at 4 ℃ and the resulting pellet resuspended in 1.5 mL Ca^{2+}/Mg^{2+}-free DPBS (Gibco,
924   #14200075). This was combined with 500 μL of fresh isotonic percoll solution [1 part
925   Ca^{2+}/Mg^{2+}-free DPBS, 9 parts Percoll (Cytiva, #17-0891-02)] and mixed by pipetting. 2 mL of
926   DPBS was gently layered on top of the Percoll-homogenate solution creating two separate
927   layers. The solution was then centrifuged at 3000 x g for 10 minutes at 4 ℃ resulting in a disc
928   of myelin between the lower and upper layers of Percoll and DPBS. The myelin was transferred
929   to a new 1.5 mL tube and centrifuged at max speed for 10 minutes at 4 ℃. The myelin pellet
930   was washed twice with DPBS and protein concentration measured using the Pierce Rapid
931   Gold BCA Protein Assay Kit (Pierce, #A53225). **Synaptic protein**. Human synaptic protein was
932   isolated from fresh human brain tissue using the Syn-PER Synaptic Protein Extraction Reagent
933   protocol (ThermoFisher, #87793). Human brain tissue was homogenized in Syn-PER Reagent
934   and synaptic protein isolated by centrifugation. **Amyloid beta**. Amyloid-β (Aβ) was aggregated
935   using the Beta Amyloid (1-42) Aggregation Kit (rPeptide, #A-1170-025) according to the
936   manufacturer's protocol. In brief, lyophilized Aβ was reconstituted and incubated at 37 ℃
937   overnight to allow for protein aggregation. After 24 hours, aggregates were collected by
938   centrifugation and the pellet was rinsed once in 1 mL Ca^{2+}/Mg^{2+}-free DPBS (Gibco, #14200075)
939   before being resuspend in 200 μL of filtered 0.1 M sodium bicarbonate (Sigma, #S5761) for
940   pHrodo labeling. **pHrodo Labeling.** Isolated myelin, synaptic protein, and aggregated amyloid-
941   beta was labeled using 1 μL (10.2 mM) pHrodo Red SE (Fisher, #P36600) per 1 mg of protein
942   and incubated for 1 hour at room temperature protected from light. Labeled protein was then
943   washed three times with DPBS before resuspending in PBS to a 100x stock concentration
944   (1.25 mg/mL) and stored at -20 ℃ until further use. **Apoptotic neurons**. Apoptotic neurons
945   were prepared using a modified protocol (*23, 80*). SH-SY5Y neurons (ATCC, #CRL-2266) were
946   seeded in 6-well tissue culture-treated corning plates and grown to confluence. To induce
947   apoptosis, SH-SY5Y cells were placed inside a tissue culture biosafety cabinet without the
948   plate cover and exposed to 60 lux of UV light for 1 min. UV lux was determined by Digital Lux
949   Meter (Dr. Meter, # LX1010B). Neurons were harvested by pipetting with 1 mL Ca^{2+}/Mg^{2+}-free
950   DPBS (Gibco, #14200075) and washed twice in PBS. Cell pellets were resuspended in 1 mL
951   PBS supplemented with 2 μL (10.2 mM) pHrodo Red SE (Fisher, #P36600) and incubated for
952   15 minutes at room temperature in the dark. Labeled neurons were washed twice in PBS
953   +20% FBS to remove any unbound pHrodo, resuspended in PBS, and counted using a
954   Countess II FL automated cell counter (ThermoFisher). Aliquots of labeled apoptotic neurons
955   were stored at -80 ℃ until used.
956

Validation of GPNMB and MITF

958   **HMC3 Cell Line Maintenance**. The HMC3 human immortalized microglia line (ATCC,
959   #CRL-3304) was maintained in Minimum Essential Medium (MEM) (Gibco, #11095098)
960   supplemented with 10% heat inactivated Fetal Bovine Serum (FBS) (Avantor, #97068-091) and

961 100 U/mL Penicillin-Streptomycin (Gibco, #15140122). Cells were maintained in 10 cm dishes

962 (ThermoFisher, #150466) and passaged by trypsinization (Gibco, #25200072). **Lentiviral**

963 **Transduction of dCas9-VPR**. The dCas9-VPR effector system was expressed in HMC3 cells

964 via lentiviral transduction. The lenti-EF1a-dCas9-VPR-Puro (Addgene, #99373) plasmid was

965 packaged into lentivirus using the VectorBuilder lentiviral packaging service, and stable cell

966 lines were generated according to the manufacturer's instructions

967 (https://www.addgene.org/protocols/generating-stable-cell-lines/). Parent lines expressing the

968 dCas9-VPR system were clonalized, and dCas9 expression confirmed by qPCR. **Guide RNA**

969 **Design and Preparation**. Guide RNA design and preparation protocols were adapted from the

970 previously established protocols by Li and colleagues (*81*). Guide RNA (gRNA) sequences for

971 MITF and GPNMB were identified by searching the CRISPR-ERA database for "gene

972 activation" using the most up-to-date human reference genome (Human GRCh37/h19). Genes

973 were searched indicating "U6 promoter" given our specific gRNA cloning vector. gRNA

974 sequences with the highest efficiency and specificity ("E+S") scores were selected and

975 confirmed to have no off-target binding using the Cas-OFFinder database

976 (http://www.rgenome.net/cas-offinder/). gRNA sequences were then cloned into the

977 lentiGuide-Hygro-mTagBFP2 (Addgene, #99374) backbone using Golden Gate Assembly for

978 digestion and ligation. Competent e. coli (NEB, #C3019I) were transformed using the gRNAs

979 cloned into the lentiGuide-Hygro-mTagBFP2 (Addgene, #99374) plasmid vector according to

980 the manufacturer's protocol for heat shock transformation. Transformed bacterial colonies

981 were grown on Ampicillin Agar (InvivoGen, #FAS-AM-S) at 37 ˚C overnight prior to inoculation

982 of liquid cultures (InvivoGen, #FAS-AM-B). Plasmid DNA was isolated using the Plasmid Mini

983 Kit (Qiagen, #12125) and subjected to sanger sequencing (Genewiz Azenta Life Sciences) to

984 confirm the presence of gRNA sequences. **Lentivirus Preparations**. Human embryonic kidney

985 cells (HEK293T) were used to package gRNA plasmids into lentivirus. Lentiviral production was

986 completed using a polyethyleneimine (PEI) (Polysciences, #23966-2) transfection strategy as

987 described by Li and colleagues (*81*). Transfections in HEK293T cells were performed in 15 cm

988 plates (Nunc, #150468) when cells reached approximately 80% confluency. A "PEI

989 transfection-mixture" of 110 µL PEI to 250 µL Opti-MEM (Gibco, #31985-062) was combined in

990 a 1:1 ratio with a "DNA-mixture" containing 250 µL Opti-MEM, 8.1 µg pMDLg/pRRE (Addgene,

991 #12251), 3.1 µg pRSV-Rev (Addgene, #12253), 4.1 µg pCMV-VSV-G (Addgene, #8454) and

992 12.2 µg gRNA plasmid DNA. PEI-mixture and DNA-mixtures were mixed and incubated at

993 room-temperature for 15 minutes. After incubation, 700 µL of the mixture was added to the

994 HEK293T cells and incubated at 37 ˚C for 6 hours before being replaced with 15 mL complete

995 media. After 48 hours of incubation, viral media was collected, stored at 4 ˚C and fresh HEK

996 media was replaced for an additional 24 hours incubation. Viral media was collected a second

997 time before concentrating with Lenti-X Concentrator (Takara, #631232) according to the

998 manufacturer protocol. Viral quantification was completed by isolating viral RNA using the

999 NucleoSpin RNA Virus Kit (Takara, #740956), and viral copies determined using the Lenti-X

1000 qRT-PCR Titration Kit (Takara, #631235). **CRISPR activation of MITF and GPNMB**. HMC3

1001 cells were plated in 96-well plates at a seeding density of 10,000 cells per well. After adhering

1002 overnight, cells were treated with gRNA-containing lentivirus at a final concentration of 3225

1003   viral copies/µL (based on qPCR). Cells were transduced with virus for 24 hours before

1004   removing vial media and replacing with hygromycin (1 mg/mL) antibiotic selection media for 48

1005   hours. **Phagocytosis**. Seventy-two hours after transduction, pHrodo-labeled substrate; myelin

1006   (5 µg/mL), amyloid-beta (5 µg/mL) or SHSY5Y Apoptotic Neurons (5000 cells/well) was added,

1007   and plates were imaged by Incucyte. Fluorescent intensity was recorded, capturing four

1008   images per well across two replicate wells. All conditions were plated in triplicate across two

1009   replicate plates and imaged after 24 hours. For RNA isolation and quantification of target genes

1010   by RT-qPCR, cells in replicate wells were harvested and pooled to increase RNA yield. **RT-**

1011   **qPCR**. HMC3 cells were harvested by trypsinization and RNA isolated using the Arcturus

1012   PicoPure RNA Isolation Kit (Applied Biosystems, #12204-01). RNA was quantified by

1013   NanoDrop (ThermoScientific, #840274100). RT-qPCR was performed using the Power SYBR

1014   Green RNA-to-CT 1-Step Kit (Applied Biosystems, #4389986) on the QuantStudio 5 Real-Time

1015   PCR System (Applied Biosystems, #A28135). qPCR primers were obtained from Integrated

1016   DNA Technologies (IDT), sequences for the PrimeTime qPCR Primers can be found in

1017   **Supplementary Table S16**.

1018

1019   **TREM2 validation using iPSC-derived microglia**

1020   **Preparation of iPSC-derived microglia**. Isogenic TREM2 wild-type (WT) (FujiFilm,

1021   #C1110), heterozygous knockout (HZ) (FujiFilm, #C1134), and homozygous knockout (HO)

1022   (FujiFilm, #C1136) lines were obtained from FujiFilm and maintained in iCell Culture media

1023   according to the manufacturer's protocols. TREM2 WT, HZ, and HO iCell microglia were plated

1024   at 125,000 cells/mL in Poly-D-Lysine (Gibco, #A3890401) coated plates according to the

1025   manufacturer's protocol. **Phagocytosis**. Cells were maintained in culture media for 72 hours

1026   before addition of phagocytosis substrates: amyloid-beta (5 µg/mL), myelin (5 µg/mL), synaptic

1027   protein (5 ug/mL), or apoptotic neurons (35,000/mL), with or without the MITF pathway

1028   inhibitor, ML329 (2 µM, MedChemExpress, #HY-101464)(*23, 82*). Phagocytosis was assessed

1029   using the Sartorius Incucyte S3 Live-Cell Analysis System by imaging four fields per well. RFP

1030   was used to visualize and measure phagocytosed pHrodo-labeled substrate, while bright-field

1031   was used to estimate cell confluency. Phagocytosis was analyzed 24 hours after introduction

1032   of the substrate using the Incucyte analysis software. Statistical analyses were conducted in

1033   GraphPad Prism using two-tailed t-tests to compare phagocytosis across cell lines. **RT-qPCR**.

1034   For RT-qPCR analyses, cells were harvested by pipetting and prepared for RNA isolation using

1035   the Arcturus PicoPure RNA Isolation Kit (Applied Biosystems, #12204-01). RNA was quantified

1036   by NanoDrop (ThermoScientific, #840274100). RT-qPCR was performed on isolated RNA using

1037   the Power SYBR Green RNA-to-CT 1-Step Kit (Applied Biosystems, #4389986) on the

1038   QuantStudio 5 Real-Time PCR System (Applied Biosystems, #A28135). qPCR primers were

1039   obtained from Integrated DNA Technologies (IDT), sequences for the PrimeTime qPCR Primers

1040   can be found in **Supplementary Table S16**. **FACS**. For analysis of phagocytosis by flow

1041   cytometry, cells were harvested by pipetting before incubating with GPNMB Monoclonal

1042   antibody (Proteintech, #66926-1) at 1:1000 for 1 hour, followed by Goat anti-Mouse IgG (H+L)

1043   Cross-Adsorbed Secondary Antibody, Alexa Fluor™ 750 (ThermoFisher, #A-21037) at 1:1000

1044   for 30 minutes. Just prior to FACS, DAPI (ThermoFisher, #62248) was added at 1:10,000. Cells

1045   were then analyzed by flow cytometry for fluorescence of pHrodo-positive phagocytosed

1046   substrate and for the presence of GPNMB protein. Cells were sorted into low and high

1047   substrate populations for RNA isolation and qPCR, as previously described.

1048

1049   **Compositional variation analysis**

1050   We applied `crumblr` method (https://diseaseneurogenomics.github.io/crumblr) for testing

1051   the variation of cell type composition. Analysis of count ratio data (i.e., fractions) requires

1052   special consideration since data is non-normal, heteroskedastic, and spans a low-rank space.

1053   While counts can be considered directly using Poisson, negative binomial, or Dirichlet-

1054   multinomial models for simple regression applications, these can be problematic since they 1)

1055   can be very computationally expensive, 2) can produce poorly calibrated hypothesis tests, and

1056   3) are challenging to extend to other applications. The widely used centered log-ratio (CLR)

1057   transform from compositional data analysis makes count ratio data more normal and enables

1058   use the of linear models and other standard methods. Yet CLR-transformed data is still highly

1059   heteroskedastic: the precision of measurements varies widely. This important factor is not

1060   considered by existing methods. `crumblr` uses a fast asymptotic normal approximation of

1061   CLR-transformed counts from a Dirichlet-multinomial distribution to model the sampling

1062   variance of the transformed counts. `crumblr` enables incorporating the sampling variance as

1063   precision weights to linear (mixed) models in order to increase power and control the false

1064   positive rate. `crumblr` also uses a variance stabilizing transform (vst) based on the precision

1065   weights to improve the performance of PCA and clustering.

1066

1067   **Differential gene expression analysis**

1068   We applied `dreamlet` for differential expression analysis. Building from the previously

1069   developed statistical tool Dream (*83*), it applies linear mixed models to the differential

1070   expression problem in single-cell omics data. It starts by aggregating cells by the donor using a

1071   pseudobulk approach (*84, 85*) and fits a regression model and cell. For each feature and cell

1072   cluster, the following mixed model was applied: `Gene expression ~ Intercept + age +`

1073   `(1|sex) + (1|ancestry) + PMI + (1|batch) + (1|source) + phenotype,`

1074   where categorical and numerical variables were modeled as random and fixed effects,

1075   respectively. We ran gene set analysis using the full spectrum of gene-level t-statistics (*86*).

1076

1077   **Mediation analysis**

1078   Causal Mediation Analysis was performed using the mediation R package (*87*). From

1079   PsychAD cohort, we subsetted to 645 individuals with European ancestry who have AD

1080   phenotype variables and PRS calculations from the latest AD GWAS(*8*). For each regression,

1081   we used the following covariates:

1082

1083   `Age + Sex + PMI + PC1 + PC2 + PC3 + PC4 + PC5 + PC6 + PC7 + PC8 + PC9`

1084   `+ PC10`

1085

1086   where PC1-10 indicate genotype PCs. For the subtype composition, we used CLR-transformed

1087   cell count fractions obtained from `crumblr` analysis. For bootstrapping, we used 10,000

1088   simulations with 50th percentiles of the treatment variable used as the control condition and
1089   90th percentile of the treatment variable used as the treatment condition.
1090

1091 Constructing gene regulatory networks

1092   We inferred gene regulatory networks with the pySCENIC (v 0.12.1)(*31, 32*) pipeline using a
1093   concatenated dataset of FreshMG and PsychAD microglia cohorts. We followed the standard
1094   SCENIC expression preprocessing; log normalizing expression counts and selecting highly
1095   variable genes (3,192 total) while accounting for batch correction between datasets with
1096   scanpy (v1.9.3). The pySCENIC's GRNboost2 (arboreto v0.1.6) method was utilized for gene
1097   regulatory network inference. The pySCENIC's cisTarget function with Human motif database
1098   v10 (https://resources.aertslab.org/cistarget/motif2tf/motifs-v10nr_clust-nr.hgnc-m0.001-
1099   o0.0.tbl) was used to enrich for gene signatures and pruned based on *cis*-regulatory cues
1100   using default settings. The "aucell" positional argument was utilized to find the enrichment of
1101   regulons across single cells.
1102   To compare regulon enrichment between subtypes, the resulting AUCell matrix was z-
1103   score normalized. To assess the concordance between regulon enrichment across subtypes
1104   between FreshMG and PsychAD cohorts, we computed the Pearson correlations between
1105   normalized z-scores using the pandas `corrwith` function. For each dataset, we computed the
1106   normalized regulon enrichment Z-score, and performed a meta-analysis between two datasets
1107   using Stouffer's method.
1108   To test whether there is a significant association between the target genes of a TF and
1109   disease signatures, we performed Fisher's exact tests between SCENIC GRN target genes and
1110   AD risk gene signatures, based on `Dreamlet` DEG analysis. Disease-associated genes with
1111   FDR < 0.05 were selected based on four different measures of AD severity, namely, case-
1112   control diagnosis, Braak, CERAD, and dementia status. The top 3 regulons were prioritized
1113   based on the overall enrichment of the AD DEG signature. The similarity between target genes
1114   of regulons was evaluated using the Jaccard similarity index. We found the target genes of the
1115   top 3 TFs shared high similarity and clustered distinctly from other regulons (**Supplementary**
1116   **Fig. S6B**). Node centrality was calculated using PageRank analysis, which measures a ranking
1117   of the nodes in the graph based on the structure of the incoming links (**Supplementary Fig.**
1118   **S6C**). The mean estimate and -log10FDR of target risk genes in SCENIC regulons are
1119   visualized using the importance score edge weights from GRNboost2 with networkX (v3.1). For
1120   each regulon, a list of SCENIC GRN TF target genes after cisTarget pruning were obtained and,
1121   using gseapy (v1.0.5)(*88*), tested for gene-set enrichment based on the Gene Ontology
1122   Biological Processes 2023 reference (*88*). GO terms were clustered based on their Ward
1123   distance between -log10FDR values.
1124

1125 Constructing a pseudotemporal trajectory of AD

1126   We followed the same steps when constructing Braak-stage-informed pseudotimes for the
1127   FreshMG and PsychAD datasets, respectively. First, cells that were not assigned a Braak stage
1128   were excluded and the data subsetted to contain either only cells annotated as adaptive,
1129   homeostatic, ADAM, or PVM. We then computed a k-nearest-neighbor graph using Scanpy

1130   (*73*) (`scanpy.pp.neighbors`, k = 30, n_pcs = 15) on the PCA embedding, regressed with

1131   Harmony. Finally, transport maps were computed between pairs of consecutive disease stages

1132   using moscot's TemporalProblem (*29*).

1133

1134   **Identification of driver genes with CellRank 2**

1135   To identify drivers of disease progression within each cell type, we first estimated a cell-cell

1136   transition matrix T using the `RealTimeKernel` implemented in the CellRank framework (*30*).

1137   Disease stage heterogeneity within each Braak stage was accounted for by including cell-cell

1138   similarity (`conn_weight=0.1`). Since moscot relies on entropical regularization to solve the

1139   underlying optimal transport problem, it returns dense transport maps, leading to negligible

1140   transition probabilities and large memory requirements when computing the transition matrix.

1141   To render our downstream analysis computationally feasible, we thresholded the constructed

1142   transition matrix using the `RealTimeKernel`'s automatic thresholding scheme

1143   (`threshold="auto"`).

1144   Based on the `RealTimeKernel`-derived transition matrix, we estimated terminal states

1145   with the GPCCA estimator (*30*, *89*). In the case of adaptive and homeostatic cells, we

1146   computed terminal states at the resolution of subclasses (MG_Adapt, MG_Homeo), for the

1147   PVM subset based on the subtype (PVM_CD163, ADAM_GPNMB) annotation. We confirmed

1148   the estimated terminal states as biologically plausible by quantifying the cell type and disease

1149   stage purity, respectively. Given n cells (n = 30 in this study) identifying a terminal state, the

1150   disease stage purity is defined as

1151

$$\frac{|C \cap B_j|}{n},$$

1152

1153

1154   with C denoting the set of cells identifying the terminal state, B_j the set of cells with Braak

1155   stage j, and $|\cdot|$ the cardinality of the set. Cell type purity is defined similarly.

1156   We computed fate probabilities towards each terminal state next and identified driver

1157   genes by correlating gene expression with fate probabilities as outlined in the corresponding

1158   CellRank tutorial. To compare the gene ranking between the FreshMG and PsychAD cohorts,

1159   we subsetted to genes present in both datasets and computed the Pearson correlation

1160   coefficient between the gene-specific correlations $r_{\text{FMG}}^{(g)}$ and $r_{\text{PAD}}^{(g)}$ by CellRank:

1161

$$r = \frac{\sum_g \left(r_{\text{FMG}}^{(g)} - \bar{r}_{\text{FMG}}^{(g)} \right) \left(r_{\text{PAD}}^{(g)} - \bar{r}_{\text{PAD}}^{(g)} \right)}{\sqrt{\sum_g \left(r_{\text{FMG}}^{(g)} - \bar{r}_{\text{FMG}}^{(g)} \right)^2} \sqrt{\sum_g \left(r_{\text{FMG}}^{(g)} - \bar{r}_{\text{FMG}}^{(g)} \right)^2}},$$

1162

1163

1164   with sample mean $\bar{r}$.

1165

Pseudotime construction

DPT (*90*) is traditionally calculated on a symmetric connectivity matrix, the constructed transition matrix T is, however, non-symmetric. To compute DPT based on our Braak-stage-informed transition matrix, we, thus, symmetrized T via $\frac{1}{2}(T + T^{\mathrm{T}})$ and row-normalized entries. Following, we computed diffusion pseudotime using SCANPY's `scanpy.tl.dpt` function with default values. The corresponding initial cells were identified via extreme points in diffusion components (*91*). To verify that the constructed pseudotime recapitulates our findings that homeostatic CECR2 cells decline with disease progression, while the number of homeostatic PICALM cells increases, we stratified pseudotime by subtype (**Fig. 5C**). Next, we performed a Welch's t-test to validate that homeostatic CECR2 cells are assigned significantly smaller pseudotime values compared to the set of homeostatic PICALM. We performed similar Welch's t-tests to assess the change between consecutive Braak stages. For each dataset, we first computed the T-statistics from Welch's t-test and then combined them across datasets using Stouffer's method: Considering T-statistics T^{freshMG} and T^{psychAD}, the reported T-statistic T given by

$$T = \frac{T^{\mathrm{freshMG}} + T^{\mathrm{psychAD}}}{2}.$$

As a final analysis, we correlated fate probabilities with gene expression for each lineage to identify putative driver genes for each lineage. Here, we included genes present in both datasets. To confirm concordance between the two independent cohorts, we computed the Spearman correlation between the two rankings.

Inferring cell-to-cell interactions

CCI analysis relies on inference of ligand-receptor interactions given a gene expression matrix with annotated cell types. By comparing to a known set of ligand-receptor (LR) pairs (reference "resource"), CCI can be inferred and scored through a variety of methods. LR pairs across cell types that are expressed above a set threshold and are differentially co-expressed, are inferred to represent interactions between the cell types. The `LIANA` (*33*) framework combines several established CCI inference methods and reference resources. We used the Python implementation of `LIANA` (v0.1.8). For each donor in FreshMG and PsychAD, we separately ran the standard rank_aggregate pipeline (resource_name = 'consensus', expr_prop = 0.1, min_cells = 5, n_perms = 1000). This utilizes the RobustRankAggregate (*92*) algorithm for aggregating scores from several methods (CellPhoneDB, Connectome, log2FC, NATMI, SingleCellSignalR, and CellChat)(*33*, *93–97*) into a single magnitude score for each CCI. We used the standard "consensus" CCI reference resource provided by `LIANA`. For a given pair of cell types and pair of genes to be considered for CCI scoring, each gene must be found in the reference resource, and be expressed in at least 10% of each involved cell type and in at least 5 cells. We evaluated CCI using the rank aggregate magnitude score for cell types annotated at the subtype level. We negative log-transformed these scores so that low magnitude CCI are

1206   scored close to 0 and normalized the score distribution. Additional post-processing was then
1207   performed to filter out CCI that were not expressed in both FreshMG and PsychAD.
1208   To assess the concordance between FreshMG and PsychAD CCI scores, we first
1209   computed the average CCI score for each CCI across donors within each cohort. We then
1210   grouped the average scores by each possible pair of subtypes and measured the Spearman
1211   rank correlation. We additionally computed an activity z-score for the frequency of CCI
1212   involving each subtype pair (**Fig. 4A**).
1213   To determine whether CCI are differentially expressed in AD, we applied Dream[13] to
1214   construct a linear mixed model and account for technical and biological covariates (batch, age,
1215   sex). Linear mixed model regression was performed separately for FreshMG and PsychAD
1216   across four measures of AD progression: diagnosis (dx_AD), CERAD score, Braak stage, and
1217   dementia status. We then also used Dream to meta-analyze CCI that are significantly
1218   differentially expressed across both cohorts and to estimate the log fold change effect of each
1219   CCI for each AD progression measure (**Fig. 4B, Supplementary Fig. S7C**).
1220   To evaluate whether significantly differentially expressed CCI are enriched in AD genome-
1221   wide association studies (GWAS), we utilize the Multi-marker Analysis of GenoMic Annotation
1222   (MAGMA)(*34*). The MAGMA gene set was constructed from significantly differentially expressed
1223   CCI LR pairs. These include CCI with at least a false discovery rate (FDR) of 0.05 significance,
1224   as determined by the Dream regression meta-analyses across each AD progression measure.
1225   We normalized the log2 fold change (log2FC) values for these CCI for each progression
1226   measure and split the CCI into AD (log2FC > 0) and CTRL (log2FC < 0) groups. Top LR pairs
1227   for AD and CTRL were then ranked by selecting the LR pairs involved in the CCI with the
1228   largest absolute normalized log2FC values. The ranked AD and CTRL LR pair gene sets were
1229   analyzed by the MAGMA for enrichment across several GWAS (**Fig. 4C**). We generated a
1230   network diagram to highlight the top-ranked three AD and CTRL CCI in our gene set (**Fig. 4D**).
1231   To investigate the biological processes AD-relevant CCI are involved in, we performed a
1232   gene set enrichment analysis using the cell2cell (*98*) package and the human Gene Ontology
1233   Biological Processes 2023 reference (*99, 100*) The AD-relevant CCI gene set was constructed
1234   in the same way as the MAGMA analysis gene set. We aggregated these CCI by the sender and
1235   receiver subtype to improve statistical power, and then computed normalized enrichment
1236   scores for each process based on our AD-relevant LR pair gene set. We prioritized processes
1237   that pass the 0.05 FDR significance threshold (**Fig. 4E**).
1238
1239   **Analysis of genetic heritability of AD polygenic risk**
1240   We established a standardized pipeline for Multi-marker Analysis of GenoMic Annotation
1241   (MAGMA) followed by single-cell Disease-Relevance Scoring (scDRS). MAGMA incorporates the
1242   association p-values of genetic variants from the latest AD genome-wide association study
1243   (GWAS)(*8*). We applied MAGMA using a standard window of 35 kbp upstream and 10 kbp
1244   downstream around the gene body. We executed scDRS using the top 1000 gene weights,
1245   sorted by Z score. The MAGMA and scDRS pipeline was run separately on FreshMG and
1246   PsychAD single-cell cohorts using the following parameters. MAGMA was run using -snp-loc
1247   g1000_eur.bim (SNP location file corresponding to the Phase 3 1000 Genome Project) and -

1248 `-gene-loc NCBI38.gene.loc` (gene location file from NCBI build 38). Both files were

1249 obtained from https://ctg.cncr.nl/software/magma.

1250 To justify the use of the top 1000 genes for `scDRS`, genes were sorted by `MAGMA` z-score

1251 and top 200, 500, and 1000 genes were used for testing the concordance between cohorts in

1252 subsequent `scDRS` analysis. `scDRS` command `scdrs.preprocess` was run with the default

1253 parameters of `n_mean_bin=20, n_var_bin=20w`, while `scdrs.score_cell` was run using

1254 `n_ctrl=100`. Best concordance between FreshMG and PsychAD cohorts of average `scDRS`

1255 scores (per myeloids subtype) was achieved using top 1000 genes (Pearson's R of top n

1256 `MAGMA` genes; n = 200 was 0.85, n = 500 was 0.94, n = 1000 was 0.97, hence we proceeded

1257 with the analysis using top 1000 `MAGMA` genes).

1258 We tested the following GWAS summary stats in `scDRS`/`MAGMA` pipeline: AD (*8*), MS (*101*),

1259 PD (*102*), MDD (*103*), ASD (*104*), BD (*105*), SCZ (*106*) and ALS (*107*). The `scDRS` scores were

1260 highly reproducible between the FreshMG and PsychAD cohorts, with AD having the greatest

1261 correlation (r = 0.97), followed by MS (r = 0.92), PD (r = 0.83), MDD (r = 0.79), ASD (r = 0.71)

1262 and ALS (r = 0.66). The lowest correlation was noted for BD (r = 0.60) and SCZ (r = 0.42), both

1263 of which are neuropsychiatric diseases. This emphasized a high reproducibility of myeloid cell

1264 heritability estimates in AD, MS, and PD, all of which are neurodegenerative diseases with

1265 progressive damage to neuronal cell types, and whose primary pathogenic mechanisms

1266 involve non-neuronal cells, including microglia and PVM. Neuropsychiatric diseases such as

1267 SCZ and BD, whose primary risks are enriched in synaptic dysfunctions of neurons, had lower

1268 correlations (**Supplementary Fig. S3C**). Per cluster association z-scores (`scDRS` assoc_mcz)

1269 were obtained using `scdrs.method.downstream_group_analysis` function. Stouffer's

1270 method for meta-analysis was used to combine FreshMG and PsychAD `scDRS` association z-

1271 scores using the number of cells per cell cluster as cluster weights. For each cohort, `scDRS`

1272 permutation p-values per cluster were combined using Stouffer's method on p-values with

1273 weights (cell counts of clusters). Meta p-values were further corrected for multiple testing using

1274 FDR correction (both per cell type and using all cell types combined). A more stringent

1275 correction was achieved using the per-cell type method hence we applied this correction.

1276

1277 **Case-control residual analysis of heritability estimates**

1278 To test for concordance in heritability estimates, we separated cases and controls and

1279 repeated `MAGMA`/`scDRS` pipe for both FreshMG and PsychAD single-cell cohorts. We

1280 calculated meta z-scores for cases and controls separately using Stouffer's method with

1281 weights (cluster's cell counts). We correlated meta-z-scores of cases and controls using linear

1282 regression and derived residuals as a deviation from the regression line, indicative of per-cell

1283 cluster heritability. For both cohorts, per-cell pseudotime scores were correlated with per-cell

1284 `scDRS` scores for every microglia subtype and the correlation coefficient was calculated using

1285 Spearman's test. FreshMG and PsychAD coefficients were combined in a meta value by

1286 applying Stouffer's method and the number of cells per cell cluster as cluster weights.

1287

Processing of genotypes

1289   The FreshMG cohort genotype data consisted of samples from the Mount Sinai and Rush
1290 brain banks, as has been previously described(*9*). The PsychAD cohort genotype data
1291 consisted of samples from the Mount Sinai brain bank. For both cohorts, DNA extraction and
1292 genotyping were performed as described previously(*9*). In brief, genomic DNA was extracted
1293 from buffy coat or frozen brain tissue using the QIAamp DNA Mini Kit (Qiagen), according to
1294 the manufacturer's instructions. Samples were genotyped using the Infinium Psych Chip Array
1295 (Illumina) at the Mount Sinai Sequencing Core. Pre-imputation processing consisted of running
1296 the quality control script HRC-1000G-check-bim.pl from the McCarthy Lab Group
1297 (https://www.well.ox.ac.uk/~wrayner/tools/), using the Trans-Omics for Precision Medicine
1298 (TOPMed) reference(*108*). Genotypes were then phased and imputed on the TOPMed
1299 Imputation Server (https://imputation.biodatacatalyst.nhlbi.nih.gov). Samples with a mismatch
1300 between one's self-reported and genetically inferred sex, suspected sex chromosome
1301 aneuploidies, high relatedness as defined by the KING kinship coefficient (*109*) (KING > 0.177),
1302 and outlier heterozygosity (+/- 3SD from mean) were removed. Additionally, samples with a
1303 sample-level missingness > 0.05 were removed and calculated within a subset of high-quality
1304 variants (variant-level missingness ≤ 0.02).
1305   Samples of European (EUR) ancestry, as defined by assignment to the EUR
1306 superpopulation described by the 1000 Genomes Project (*110, 111*), were isolated using a 3SD
1307 ellipsoid method. Genotypes were first merged with GRCh38 v2a 1000 Genomes Project data
1308 (https://wellcomeopenresearch.org/articles/4-50)(*111*) using BCFtools version 1.9 (*112*). PLINK
1309 2.0 (*113*) was then used to calculate the merged genotypes' principal components (PCs),
1310 following filtering (minor allele frequency (MAF) ≥ 0.01, Hardy-Weinberg equilibrium (HWE) p-
1311 value≥1×10^{-10}, variant-level missingness ≤ 0.01, regions with high linkage disequilibrium (LD)
1312 removed) and LD pruning (window size = 1000 kb, step size = 10, r2 = 0.2) steps. An ellipsoid
1313 with a radius of 3SD, corresponding to the 1000 Genomes Project EUR superpopulation, was
1314 constructed using the first three genotype PCs. Only samples that fell within this ellipsoid
1315 (FreshMG: n = 178, PsychAD: n = 759) were retained for subsequent variant-level filtering.
1316 Autosomal bi-allelic variants with an imputation R^2 > 0.8, HWE p-value≥1×10^{-6}, and variant-
1317 level missingness ≤ 0.02 were retained. Genotypes were then annotated with ancestry-specific
1318 MAF values from the National Center for Biotechnology Information's Allele Frequency
1319 Aggregator (ALFA) (https://ftp.ncbi.nih.gov/snp/population_frequency/latest_release/). Only
1320 variants with an ancestry-specific ALFA MAF ≥ 0.01 (FreshMG: n = 10,828,658, PsychAD: n =
1321 18,490,352) were retained.
1322
PRS calculation

1324   Polygenic risk scores (PRS) were calculated on the FreshMG and PsychAD cohort samples
1325 using AD GWAS summary statistics (*8*). The PRS-CS-auto method (*114*) was used to apply
1326 continuous shrinkage priors to the effect sizes from these summary statistics. A EUR LD
1327 reference panel provided by the developers of PRS-CS was utilized
1328 (https://github.com/getian107/PRScs), which draws from 1000 Genomes Project data (*111*).
1329 The following PRS-CS default settings were used: parameter a in the γ-γ prior = 1, parameter b

1330   in the γ-γ prior = 0.5, MCMC iterations = 1000, number of burn-in iterations = 500, and thinning
1331   of the Markov chain factor = 5. The global shrinkage parameter phi was set using a fully
1332   Bayesian determination method. Individual-level PRS were calculated using PLINK 2.0 (*113*).
1333

Transcriptional variation with PRS

1335   PRS analysis was performed using the `dreamlet` package (v0.99) that applies a linear
1336   mixed model with precision weights to fit a regression model. Instead of applying a fixed
1337   contrast between two coefficients, we used AD polygenic risk scores (PRS) as a continuous
1338   variable to test for the presence of non-linear effects on variance. We subtracted admixed
1339   donors from this analysis using the PCA analysis of the first 5 genotype PCs (2 individuals were
1340   removed from PsychAD and 1 from the FreshMG cohort as clear outliers in the PCA plots). In
1341   addition, we removed a cluster of 200 individuals that were clustering separately on the
1342   PC1/PC2 plot in psychAD as admixed individuals with a percentage of a non-EUR ancestry
1343   ranging from 2.5%-10% (mainly AFR ancestry). Similarly, we removed 6 more donors from
1344   FreshMG that were outliers and showed decreased EUR and increased AFR ancestry. The
1345   removal of admixed individuals allowed us to achieve a high level of concordance in `Dreamlet`
1346   PRS analysis between FreshMG and PsychAD cohorts. For the PsychAD cohort, we
1347   considered the following covariates to model the variance: source, log(n_counts), PMI, age,
1348   AD_Bellenguez PRS, sex, dx, genotype PCs 1-5. For the FreshMG cohort, we used the same
1349   set of covariates, in addition to the sequencing batch as a covariate. We further performed a
1350   fixed-effect meta-analysis with the R metafor package using effect sizes and standard error
1351   from the `dreamlet` output (metafor `rma` function with parameters: `yi = logFC, sei =`
1352   `logFC / t, method = "FE"`). Meta p-values were further corrected for multiple testing
1353   using FDR correction (using the per-cell type correction).
1354   To test whether the observed cell proportions change with PRS as a continuous variable,
1355   we applied the `crumblr` R package to each cohort and performed analysis of count ratio data
1356   with precision-weighted linear mixed models. Similar to the `Dreamlet` analysis, we modeled
1357   PRS as a continuous variable and tested for non-linear effects. FreshMG and PsychAD effect
1358   sizes were combined in a meta value using Stouffer's method and the number of cells per cell
1359   cluster as cluster weights.
1360

Supplementary Information

Assessment of *ex-vivo* activation in Microglia

Microglia are highly reactive cells and prolonged exposure to non-physiological conditions could induce unintended responses (*115, 116*). It has previously been shown that enzymatic dissociation of brain tissue performed at elevated temperatures can stimulate microglial cells, termed *ex-vivo* activated microglia (exAM)(*17, 79, 117*). Failing to account for dissociation-induced changes can compromise the interpretation of microglial biology (*118*). Although artificially induced, we wondered if the proportion of exAM might reflect microglial reactivity to pathological lesions and, as such, could provide valuable insights into disease mechanisms. In this study, we are uniquely positioned to interrogate the impact of exAM as myeloids from the FreshMG cohort were isolated via enzymatic dissociation at 37°C while samples from the PsychAD cohort, consisting of flash frozen tissue, were processed using an ice-cold, enzyme free, dissociation buffer. Assessing the extent and prevalence of the exAM signature in our datasets, we observed a distinct subtype in the FreshMG dataset, called MG_exAM_ERN1, which accounts for about 14.8% of all myeloid cells, and shows up-regulation of genes implicated in cell-cell adhesion, including ERN1, PLK2 (serine/threonine-protein kinase), CSKMT, and SNHG5. Notably, PLK2 is an enzyme regulating synaptic activity and has been implicated in stimulating Aβ production (*119, 120*). We note that the PsychAD dataset had very few cells identified as the ERN1 subtype, which belongs to the exAM subclass. This result suggests a number of possibilities. Given that the transcripts in the PsychAD dataset originate from the nuclear fraction of frozen nuclei and are free from enzymatic treatment or dissociation bias, it's possible that the exAM cluster is predominantly derived from fresh tissue and is artificially induced during processing (*17*). In addition, the transcripts that define the ERN1 subtype may be predominantly cytoplasmic and are, thus, missing from the PsychAD samples. Moreover, we acknowledge that we observe a substantial compositional variation among three different cohorts. However, to properly assess the extent of compositional variation, we need to model this by accounting for various technical effects, including the dissection bias. In conclusion, this comparative analysis confirmed the robustness of the human microglial taxonomy, independent of tissue source, agonal state, and postmortem interval (PMI).

Disease trajectory of human myeloid cells

Understanding the dynamic changes that take place during the onset and progression of AD at a molecular-level requires modeling of gene expression change along the measures of disease progression and identifying corresponding putative drivers. Analyses solely based on donor-level clinical covariate, such as CERAD scores or Braak staging, are limited due to the discrete nature of these variables. However, we reasoned that each labeled disease stage contains observations spanning the range of disease development and sought to identify drivers and order cells along a disease pseudotime trajectory.

Trajectory inference allows us to expand our ability to describe molecular changes at single-cell resolution. Trajectory inference methods have been remarkably successful in describing normal developmental processes faithfully and identifying regulatory mechanisms

1402   based on single-cell sequencing data (*90*, *121*, *122*). Classical pseudotime algorithms order
1403   cells along a developmental axis, with early and late cells being assigned low and high
1404   pseudotime values, respectively. To take advantage of advances in experimental design and
1405   different sources of information, alternative methods have been developed. To link
1406   observations across experimental time points, optimal transport-based solutions have been
1407   proposed to assign each measurement from one experimental time point its likely future state
1408   in the following via a probabilistic assignment in the form of transport maps (*29*, *123*). These
1409   couplings can then be used to quantify cellular change and determine the fate and putative
1410   drivers using CellRank 2's *RealTimeKernel (30)*. Using it together with and GPCCA estimator
1411   (*30*, *89*), we automatically inferred the terminal states of the disease dynamics. As AD onset
1412   and progression do not result in the emergence or disappearance of novel cell types, we
1413   expected to recover the major subclasses of the data, *i.e.*, adaptive, homeostatic, ADAM, or
1414   PVM. In concordance with this ground truth, we recovered the terminal states accordingly and
1415   observed a high terminal state purity defined by the fraction of cells with the correct cell type
1416   and Braak stage six (terminal state purity was 1.0 for all subclasses used). Following, we
1417   computed driver genes of these respective fates by correlating gene expression with fate
1418   probabilities (**Methods**). We replicated the same analysis using the PsychAD and observed
1419   high concordance between the correlations between gene expression and fate probabilities
1420   associated with each gene (**Supplementary Fig. S5I**). While CellRank 2 identifies putative
1421   lineage drivers, it does not align cells along the disease trajectory. To construct this orthogonal
1422   information, we used the transition matrix computed by the *RealTimeKernel* to compute a
1423   Braak-stage-informed pseudotime for the two subsets of the data in a similar fashion as
1424   previously proposed for experimental time points by the CellRank 2 study (*30*) (**Methods**). We
1425   tested if the gene expression changes over pseudotime inferred on the FreshMG cohort agrees
1426   with the corresponding change in the PsychAD dataset. As expected, the inferred change in
1427   gene expression showed high concordance between the two independent cohorts for both
1428   homeostatic and adaptive lineages (**Supplementary Figs. S5J-K**).

1429

Data availability

The single-cell dataset, clinical metadata, and analysis outputs are available via the AD Knowledge Portal (https://adknowledgeportal.org). The AD Knowledge Portal is a platform for accessing data, analyses, and tools generated by the Accelerating Medicines Partnership (AMP-AD) Target Discovery Program and other National Institute on Aging (NIA)-supported programs to enable open-science practices and accelerate translational learning. The data, analyses, and tools are shared early in the research cycle without a publication embargo on secondary use. Data is available for general research use according to the following requirements for data access and data attribution (https://adknowledgeportal.org/DataAccess/Instructions). For access to data described in this manuscript see: https://www.synapse.org/#!Synapse:syn52795287.

Code availability

All the source codes used in this study are available via GitHub:
https://github.com/DiseaseNeuroGenomics/scMyeloidAD

Acknowledgments

Author contributions

Conceptualization: DL, VH, JFF, PR.
Methodology: DL, GEH, JFF, PR.
Investigation: JV, XW, KP, PM, EH, JMF, SPK, ZS, SA, MA, CC, AH, JFF.
Formal analysis: DL, CP, CS, MP, SK, PW, RK, JB, PNM, SZ, KT, DM.
Validation: JV, XW, JMF, JFF.
Resources: KGB, RS, CPK, DAB, VH.
Writing: DL, JFF, PR, with contributions from all authors.
Visualization: DL, JV.

1465 Supervision: DL, GCY, GV, FJT, GEH, VH, JFF, PR.

1466 Project administration: DL, PR.

1467 Funding acquisition: DL, VH, PR.

1468 All authors read and approved the final draft of the paper.

Competing interests

1470 FJT consults for Immunai Inc., Singularity Bio B.V., CytoReason Ltd, Omniscope Ltd, Cellarity,
1471 and has ownership interests in Dermagnostix GmbH and Cellarity. The remaining authors
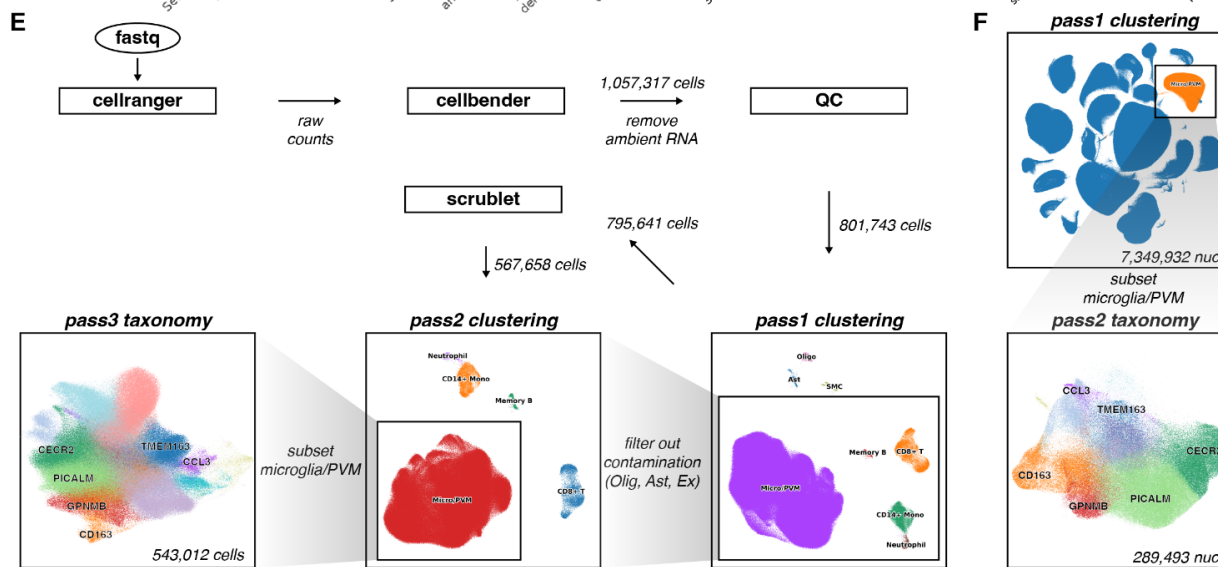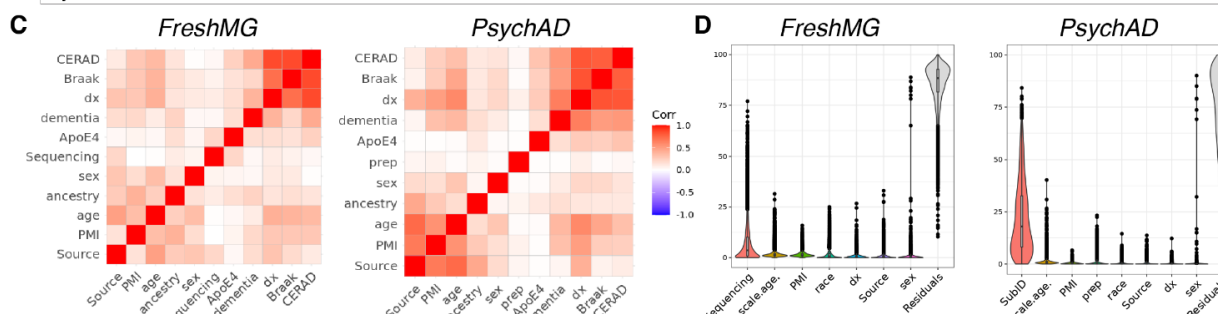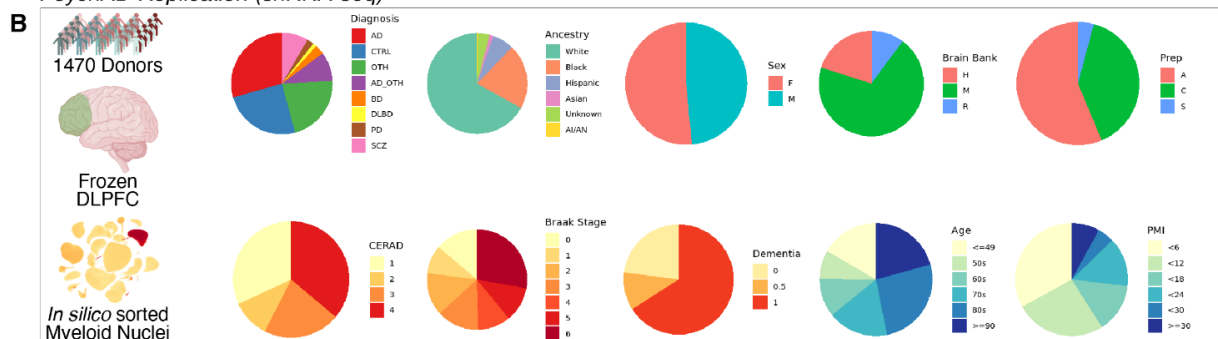1472 declare no competing interests.

Materials & Correspondence

1474 Correspondence to Donghoon Lee and Panos Roussos.

1475

1476   **Supplementary Figures**

1477
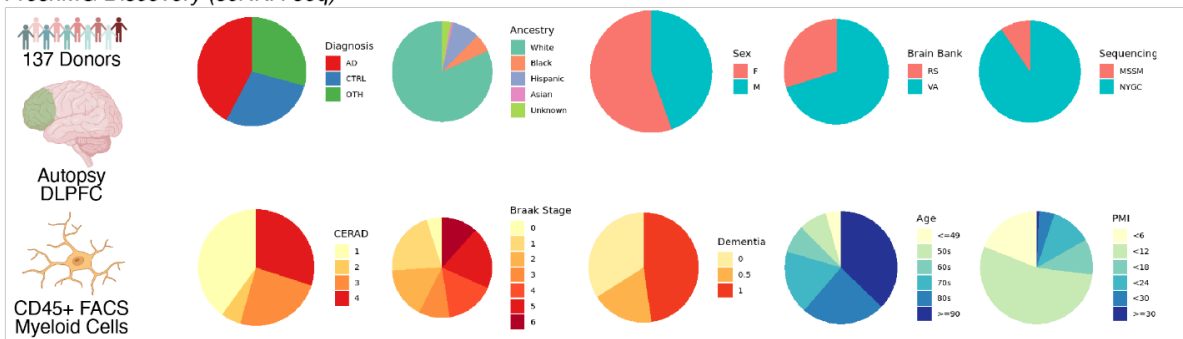
1478   **Supplementary Figure S1**. **(A)** Demographic and clinical metadata of the FreshMG cohort. **(B)**
1479   Demographic and clinical metadata of the PsychAD cohort. **(C)** Pairwise correlation of donor-
1480   level clinical variables. **(D)** Partition of gene expression variance using technical and donor-
1481   level covariates used in the study. **(E)** Schematic overview of the FreshMG single-cell data
1482   processing. **(F)** Schematic overview of the PsychAD single-cell data processing.
1483
1484
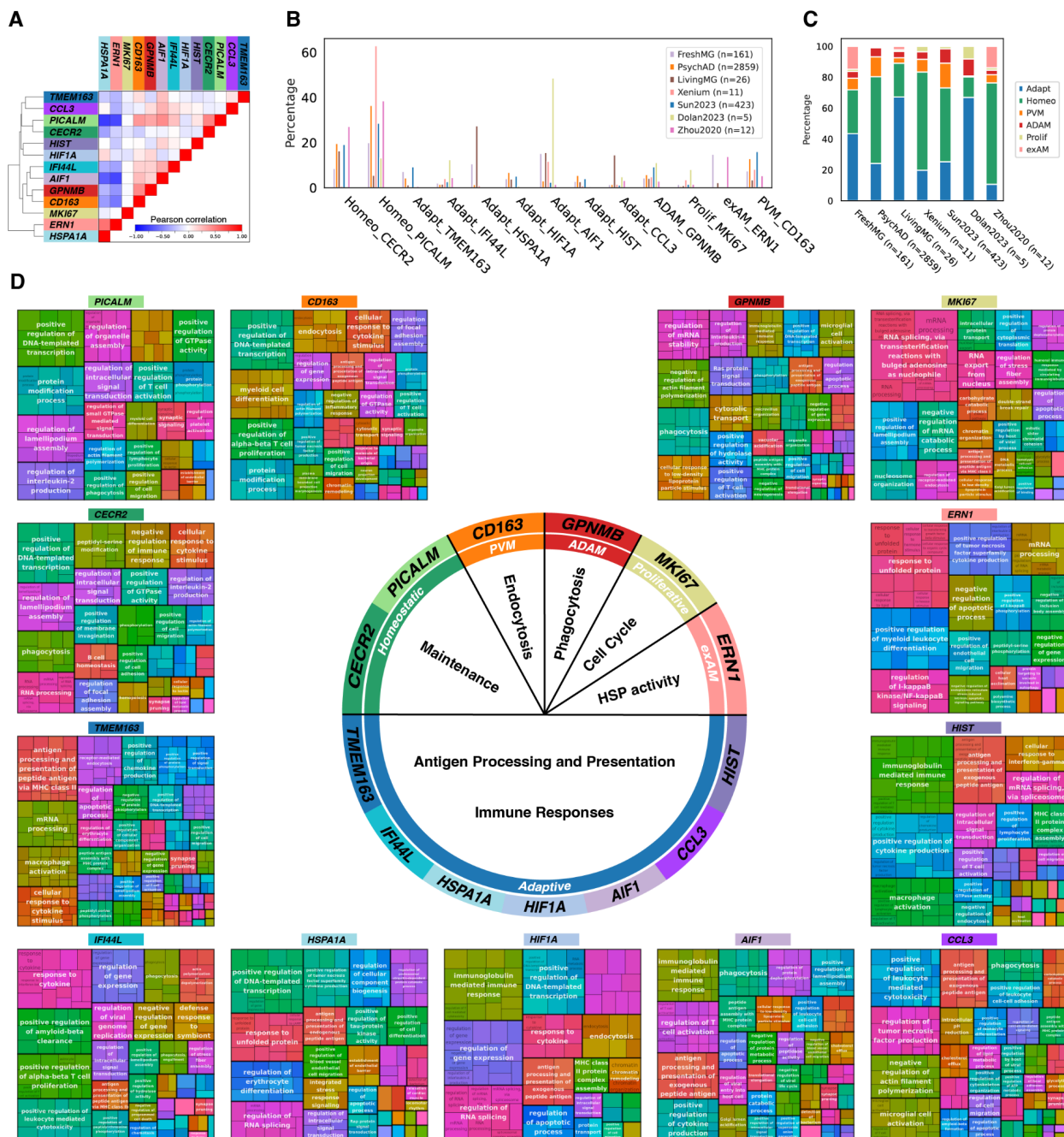
Supplementary Figure S2. **(A)** Pairwise Pearson correlation between FreshMG and PsychAD myeloid subtypes. **(B)** Compositional differences of myeloid subtypes across independent (*LivingMG* sourced from biopsy specimens and represents living brains) and published datasets; Sun2023 (*14*), Dolan2023 (*23*), and Zhou2020 (*27*). **(C)** Compositional differences of myeloid subclasses. **(D)** Pathway enrichment analysis of human myeloid subtypes using GO biological process database. Subtype-specific genes were prioritized using Mann–Whitney U tests of one-vs-the-rest subsets.
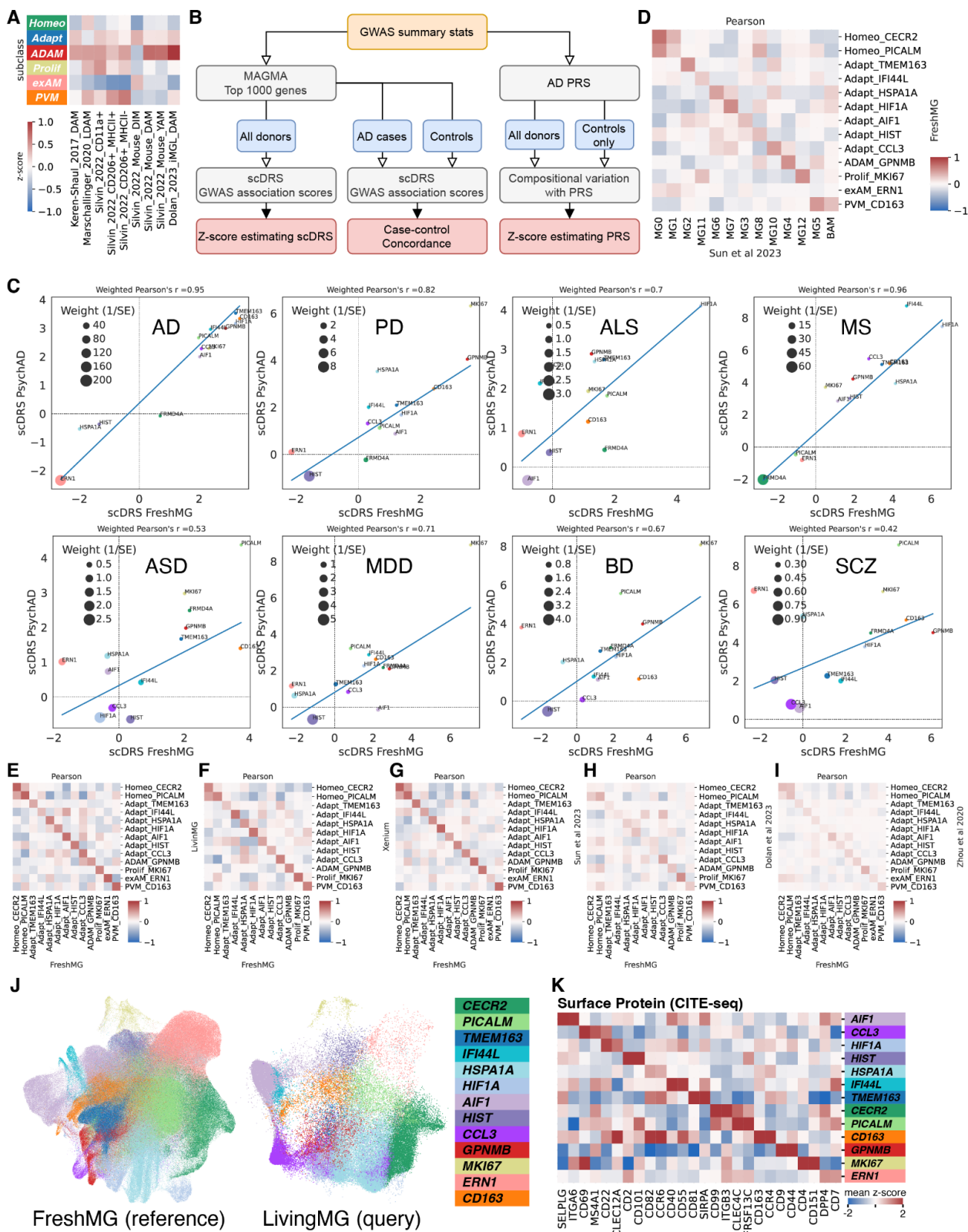
1493
Supplementary Figure S3. **(A)** Enrichment of gene signatures from published studies. DAM:
disease-associated microglia, LDAM: lipid-droplet accumulating microglia, DIM: disease

1496 inflammatory macrophages, YAM: youth-associated microglia, iMGL: human stem-cell-

1497 differentiated microglia.

1498 **(B)** Schematic overview of the `scDRS` and PRS methods for evaluating heritability of AD risk.

1499 **(C)** Correlation of the scDRS scores between the FreshMG and PsychAD cohorts across

1500 human brain disorders. **(D)** Comparison of myeloid subtypes to microglial states defined in Sun

1501 *et al*. 2023 dataset. **(E)** Pairwise Pearson correlation between FreshMG and LivingMG myeloid

1502 subtypes. **(F)** Pairwise Pearson correlation between FreshMG and Xenium myeloid subtypes.

1503 **(G)** Pairwise Pearson correlation between FreshMG and Sun *et al*. 2023 myeloid subtypes. **(H)**

1504 Pairwise Pearson correlation between FreshMG and Dolan *et al*. 2023 myeloid subtypes. **(I)**

1505 Pairwise Pearson correlation between FreshMG and Zhou *et al*. 2020 myeloid subtypes. **(J)**

1506 Annotation of the LivingMG (biopsies) dataset using the FreshMG as the reference annotation.

1507 **(K)** Subtype-specific surface protein markers from the CITE-seq antibody derived tags (ADT).

1508
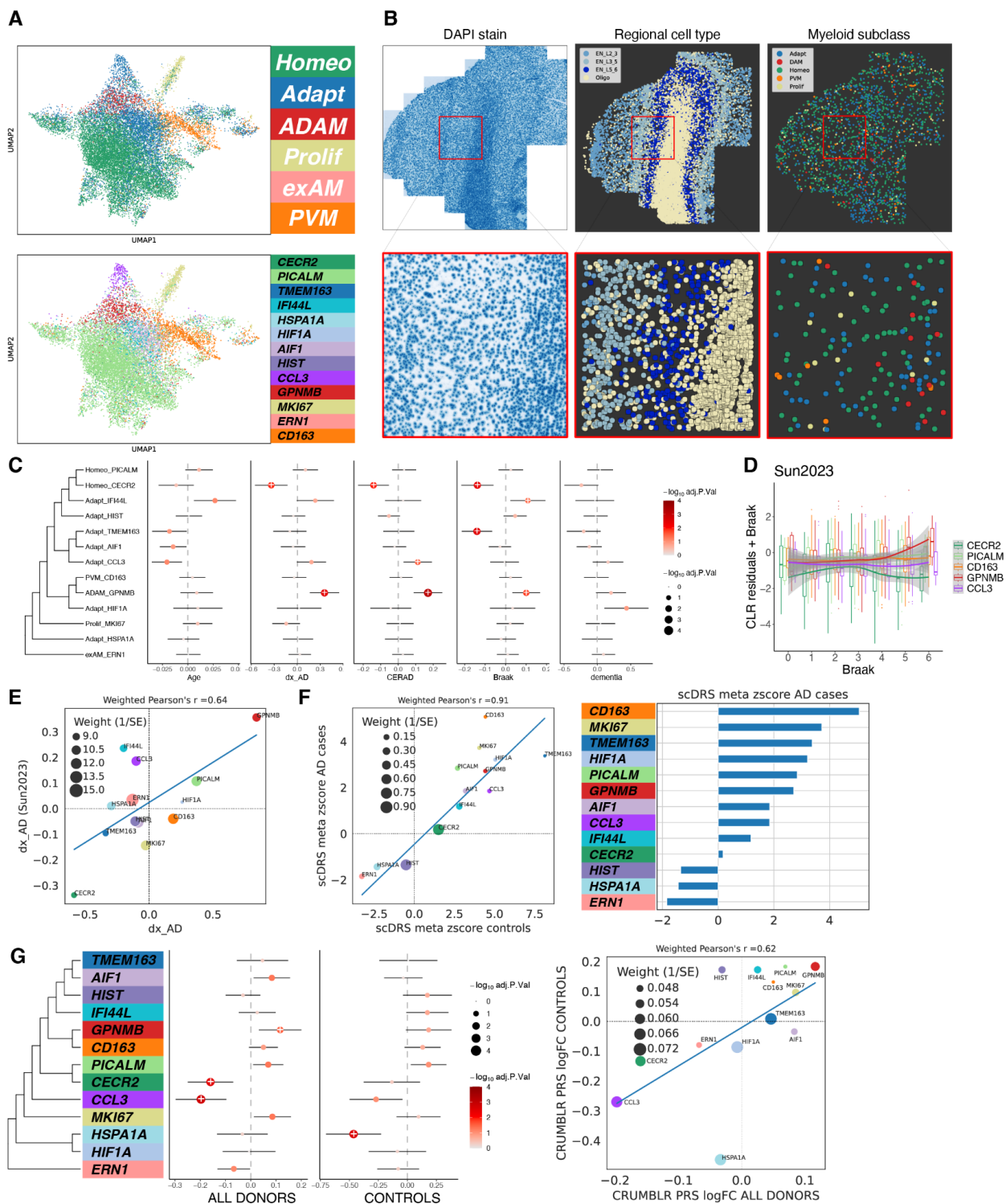
1509

1510 **Supplementary Figure S4**. **(A)** UMAP of myeloid subclasses and subtypes from the Xenium *in*

1511 *situ* spatial transcriptomics dataset. **(B)** Representative slide of Xenium *in situ* spatial

1512 transcriptomics data with zoomed in region of interest. Left: DAPI stain, Middle: laminar

1513 distribution of neuronal cell types, Right: distribution of myeloid cells annotated by subclasses.

1514 **(C)** Compositional variation of aging and AD phenotypes using Sun *et al*. 2023 dataset. **(D)**

1515   Covariate adjusted compositional variation with Braak staging using Sun *et al*. 2023 dataset. **(E)**

1516   Comparison of compositional variation of dx_AD between this study and Sun *et al*. 2023. **(F)**

1517   Correlation of `scDRS` z-scores between AD cases and controls. **(G)** Compositional variation of

1518   PRS, side-by-side comparison between one using all donors and another using control donors

1519   only. Weighted Pearson's correlation using inverse of average of standard error as weights.

1520
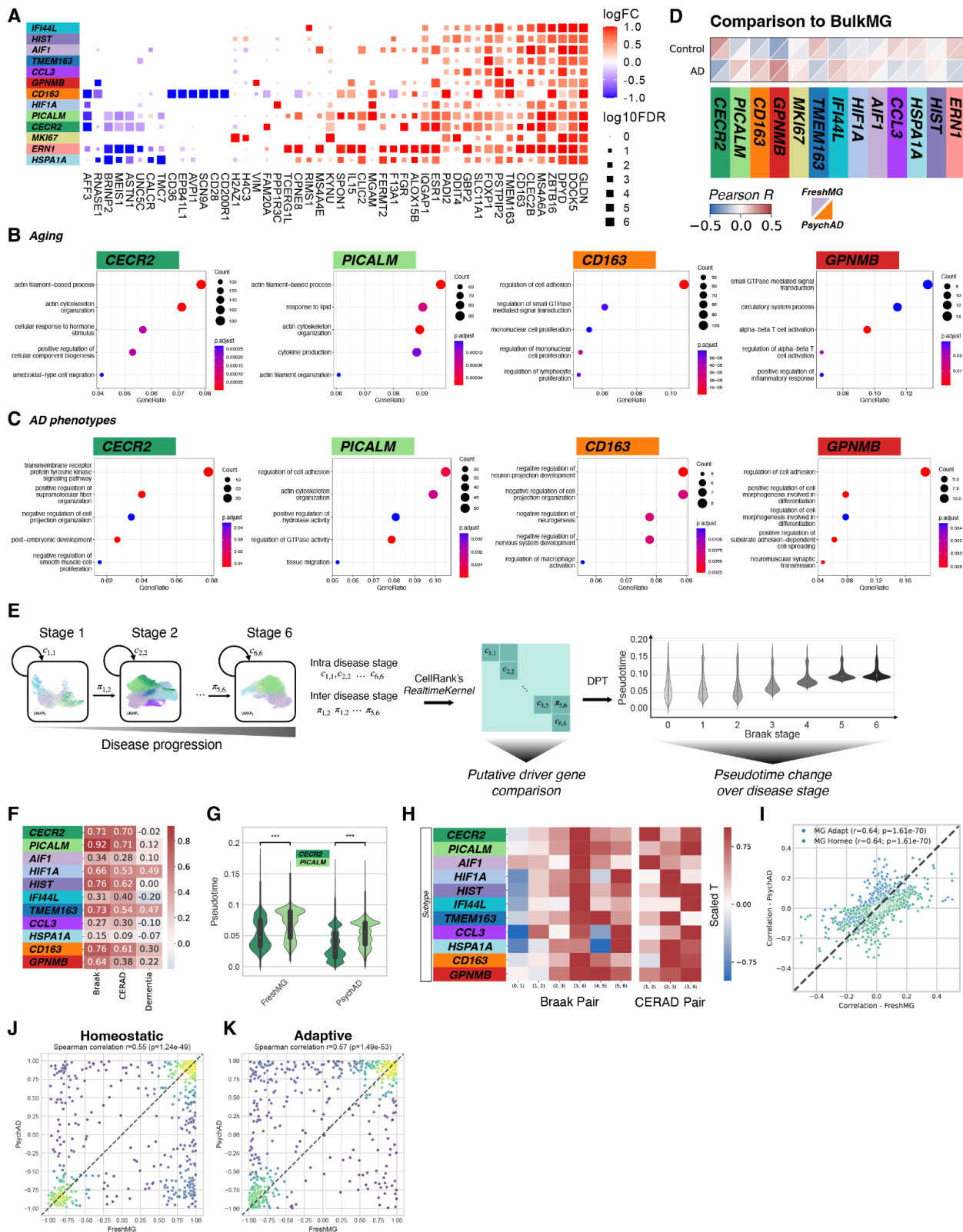
Supplementary Figure S5. (A) Differentially expressed genes by myeloid subtypes associated with disease-free aging. **(B)** Pathway enrichment analysis using the GO biological process database for disease-free aging. **(C)** Pathway enrichment analysis using the GO biological

1525 process database for AD phenotypes. **(D)** Comparison of myeloid subtypes to homogenate

1526 bulk RNA-seq expression stratified by AD diagnosis. **(E)** Schematic overview of the pseudotime

1527 inference based on Braak staging. State transition matrix inferred using the optimal transport

1528 algorithm (Moscot). **(F)** Spearman correlations between inferred disease pseudotime and

1529 different measures of AD phenotypes. **(G)** Distribution of disease pseudotime between two

1530 homeostatic subtypes. **(H)** Magnitude of changes in disease pseudotime between two adjacent

1531 disease stages measured by Braak and CERAD. **(I)** Concordance of the putative drivers of two

1532 fates (adaptive and homeostatic) between FreshMG and PsychAD cohorts. Putative drivers are

1533 defined by correlating gene expression with fate probabilities. **(J)** Correlation between gene

1534 expression change and inferred disease pseudotime showing the concordance of the

1535 correlation between FreshMG and PsychAD cohorts for homeostatic and **(K)** adaptive lineages.

1536

1537
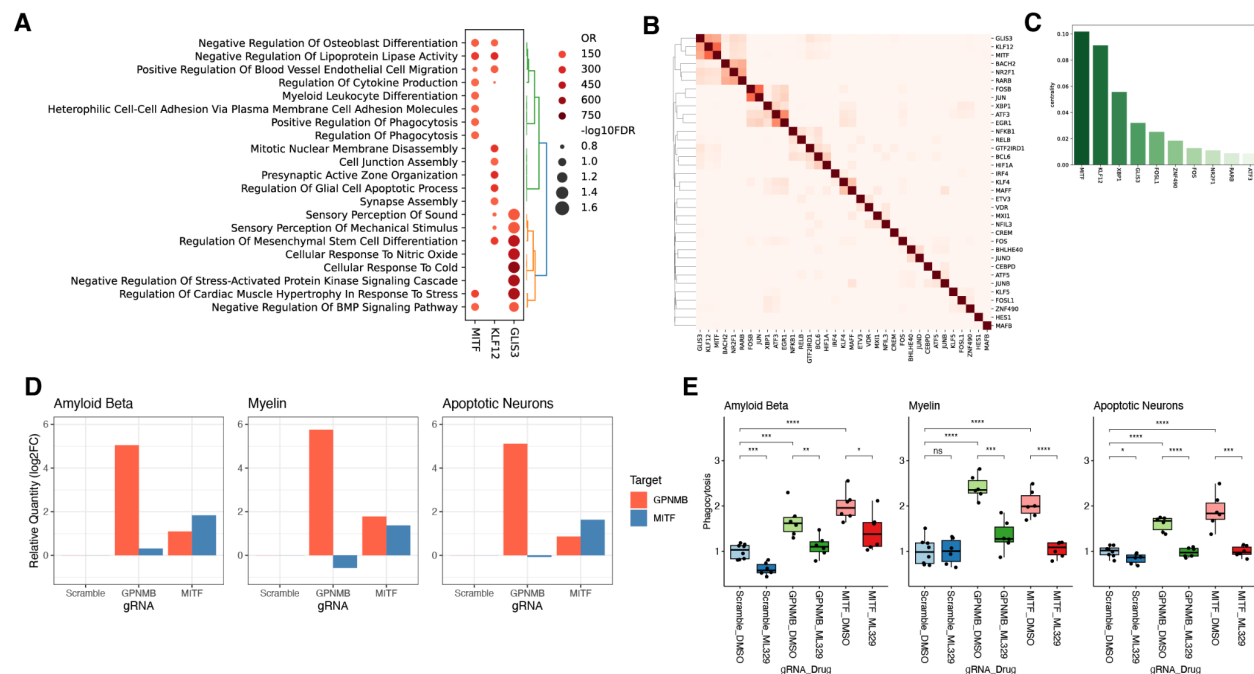
1538

1539 **Supplementary Figure S6**. **(A)** Pathway enrichment analysis of *KLF12*, *MITF*, and *GLIS3*

1540 regulons using GO biological process database. **(B)** Jaccard Index of SCENIC regulon target

1541 genes. **(C)** PageRank centrality scores of the GRN nodes. **(D)** RT-qPCR of *GPNMB* and *MITF*

1542 after CRISPR activation in HMC3 cell line. **(E)** Relative level of phagocytosis after CRISPR

1543 activation in HMC3 cell line with or without the *MITF* pathway inhibitor ML329.

1544
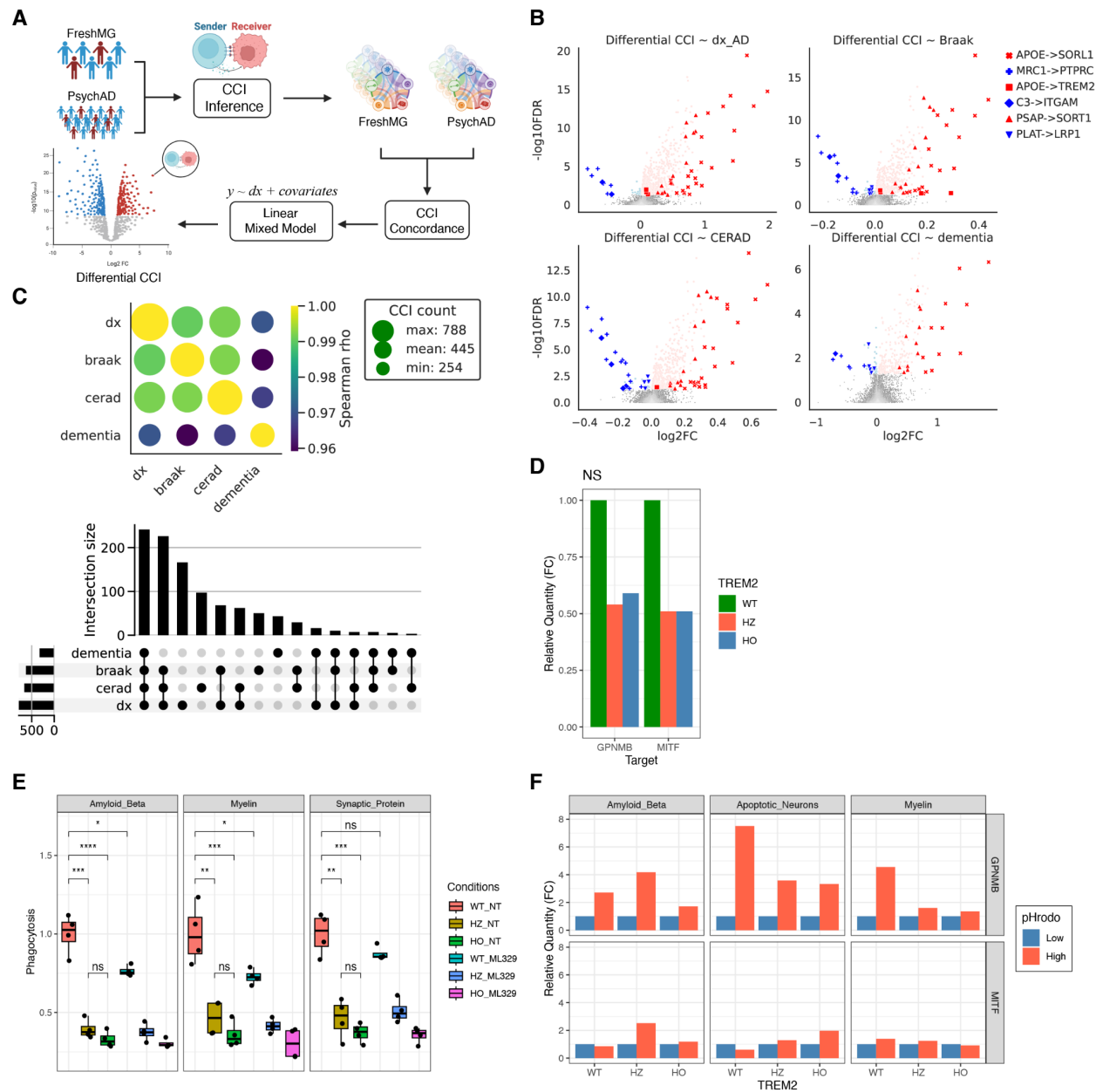
1545

Supplementary Figure S7. **(A)** Schematic overview of the methods for inferring disease-associated CCI. **(B)** Differential CCI using 4 different measures of AD phenotypes; AD cases vs controls (dx_AD), CERAD, Braak, and dementia. **(C)** Concordance of differential CCIs among different measures of AD phenotypes. **(D)** Relative mRNA expression of *GPNMB* and *MITF* measured by RT-qPCR for *TREM2* knockouts. **(E)** Relative level of phagocytosis among WT, TREM2 heterozygous, and homozygous knockouts in iPSC-derived microglia using Aβ, myelin, and synaptic protein as substrates. **(F)** Relative mRNA expression of *GPNMB* and *MITF* measured by RT-qPCR for high and low phagocytosing microglia using Aβ, myelin, and synaptic protein as substrates.

Supplementary Tables

Supplementary Table S1. Myeloid taxonomy of the FreshMG dataset with de-identified individual ID.

Supplementary Table S2. Myeloid taxonomy of the PsychAD dataset with de-identified individual ID.

Supplementary Table S3. Clinical metadata of the FreshMG dataset with de-identified individual ID and age ranges.

Supplementary Table S4. Clinical metadata of the PsychAD dataset with de-identified individual ID and age ranges.

Supplementary Table S5. List of Akoya antibodies.

Supplementary Table S6. Compositional variation meta-analysis for Aging.

Supplementary Table S7. Compositional variation meta-analysis for AD phenotypes.

Supplementary Table S8. Differential gene expression meta-analysis for Aging.

Supplementary Table S9. Differential gene expression meta-analysis for AD phenotypes.

Supplementary Table S10. Pseudotime estimates for the FreshMG dataset.

Supplementary Table S11. Pseudotime estimates for the PsychAD dataset.

Supplementary Table S12. GRN adjacencies.

Supplementary Table S13. Regulon enrichment analysis for AD signatures.

Supplementary Table S14. Differential CCI meta-analysis.

Supplementary Table S15. scDRS scores from meta-analysis.

Supplementary Table S16. List of probes for the Xenium custom panel

Supplementary Table S17. qPCR Primers for targeted proteins

Reference

1. J. M. Long, D. M. Holtzman, Alzheimer Disease: An Update on Pathobiology and Treatment Strategies. *Cell* **179**, 312–339 (2019).

2. S. Hickman, S. Izzy, P. Sen, L. Morsett, J. El Khoury, Microglia in neurodegeneration. *Nat. Neurosci.* **21**, 1359–1369 (2018).

3. F. Leng, P. Edison, Neuroinflammation and microglial activation in Alzheimer disease: where do we go from here? *Nat. Rev. Neurol.* **17**, 157–172 (2021).

4. S. De Schepper, J. Z. Ge, G. Crowley, L. S. S. Ferreira, D. Garceau, C. E. Toomey, D. Sokolova, J. Rueda-Carrasco, S.-H. Shin, J.-S. Kim, T. Childs, T. Lashley, J. J. Burden, M. Sasner, C. Sala Frigerio, S. Jung, S. Hong, Perivascular cells induce microglial phagocytic states and synaptic engulfment via SPP1 in mouse models of Alzheimer's disease. *Nat. Neurosci.* **26**, 406–415 (2023).

5. H. Keren-Shaul, A. Spinrad, A. Weiner, O. Matcovitch-Natan, R. Dvir-Szternfeld, T. K. Ulland, E. David, K. Baruch, D. Lara-Astaiso, B. Toth, S. Itzkovitz, M. Colonna, M. Schwartz, I. Amit, A Unique Microglia Type Associated with Restricting Development of Alzheimer's Disease. *Cell* **169**, 1276–1290.e17 (2017).

6. T. Jonsson, H. Stefansson, S. Steinberg, I. Jonsdottir, P. V. Jonsson, J. Snaedal, S. Bjornsson, J. Huttenlocher, A. I. Levey, J. J. Lah, D. Rujescu, H. Hampel, I. Giegling, O. A. Andreassen, K. Engedal, I. Ulstein, S. Djurovic, C. Ibrahim-Verbaas, A. Hofman, M. A. Ikram, C. M. van Duijn, U. Thorsteinsdottir, A. Kong, K. Stefansson, Variant of TREM2 associated with the risk of Alzheimer's disease. *N. Engl. J. Med.* **368**, 107–116 (2013).

7. R. Guerreiro, A. Wojtas, J. Bras, M. Carrasquillo, E. Rogaeva, E. Majounie, C. Cruchaga, C. Sassi, J. S. K. Kauwe, S. Younkin, L. Hazrati, J. Collinge, J. Pocock, T. Lashley, J. Williams, J.-C. Lambert, P. Amouyel, A. Goate, R. Rademakers, K. Morgan, J. Powell, P. St George-Hyslop, A. Singleton, J. Hardy, Alzheimer Genetic Analysis Group, TREM2 variants in Alzheimer's disease. *N. Engl. J. Med.* **368**, 117–127 (2013).

8. C. Bellenguez, F. Küçükali, I. E. Jansen, L. Kleineidam, S. Moreno-Grau, N. Amin, A. C. Naj, R. Campos-Martin, B. Grenier-Boley, V. Andrade, P. A. Holmans, A. Boland, V. Damotte, S. J. van der Lee, M. R. Costa, T. Kuulasmaa, Q. Yang, I. de Rojas, J. C. Bis, A. Yaqub, I. Prokic, J. Chapuis, S. Ahmad, V. Giedraitis, D. Aarsland, P. Garcia-Gonzalez, C. Abdelnour, E. Alarcón-Martín, D. Alcolea, M. Alegret, I. Alvarez, V. Álvarez, N. J. Armstrong, A. Tsolaki, C. Antúnez, I. Appollonio, M. Arcaro, S. Archetti, A. A. Pastor, B. Arosio, L. Athanasiu, H. Bailly, N. Banaj, M. Baquero, S. Barral, A. Beiser, A. B. Pastor, J. E. Below, P. Benchek, L. Benussi, C. Berr, C. Besse, V. Bessi, G. Binetti, A. Bizarro, R. Blesa, M. Boada, E. Boerwinkle, B. Borroni, S. Boschi, P. Bossù, G. Bråthen, J. Bressler, C. Bresner, H. Brodaty, K. J. Brookes, L. I. Brusco, D. Buiza-Rueda, K. Bûrger, V. Burholt, W. S. Bush, M. Calero, L. B. Cantwell, G. Chene, J. Chung, M. L. Cuccaro, Á. Carracedo, R. Cecchetti, L. Cervera-Carles, C. Charbonnier, H.-H. Chen, C. Chillotti, S. Ciccone, J. A. H. R. Claassen, C. Clark, E. Conti, A. Corma-Gómez, E. Costantini, C. Custodero, D. Daian, M. C. Dalmasso, A. Daniele, E. Dardiotis, J.-F. Dartigues, P. P. de Deyn, K. de Paiva Lopes, L. D. de Witte, S. Debette, J. Deckert, T. Del Ser, N. Denning, A. DeStefano, M.

Dichgans, J. Diehl-Schmid, M. Diez-Fairen, P. D. Rossi, S. Djurovic, E. Duron, E. Düzel, C. Dufouil, G. Eiriksdottir, S. Engelborghs, V. Escott-Price, A. Espinosa, M. Ewers, K. M. Faber, T. Fabrizio, S. F. Nielsen, D. W. Fardo, L. Farotti, C. Fenoglio, M. Fernández-Fuertes, R. Ferrari, C. B. Ferreira, E. Ferri, B. Fin, P. Fischer, T. Fladby, K. Fließbach, B. Fongang, M. Fornage, J. Fortea, T. M. Foroud, S. Fostinelli, N. C. Fox, E. Franco-Macías, M. J. Bullido, A. Frank-García, L. Froelich, B. Fulton-Howard, D. Galimberti, J. M. García-Alberca, P. García-González, S. Garcia-Madrona, G. Garcia-Ribas, R. Ghidoni, I. Giegling, G. Giorgio, A. M. Goate, O. Goldhardt, D. Gomez-Fonseca, A. González-Pérez, C. Graff, G. Grande, E. Green, T. Grimmer, E. Grünblatt, M. Grunin, V. Gudnason, T. Guetta-Baranes, A. Haapasalo, G. Hadjigeorgiou, J. L. Haines, K. L. Hamilton-Nelson, H. Hampel, O. Hanon, J. Hardy, A. M. Hartmann, L. Hausner, J. Harwood, S. Heilmann-Heimbach, S. Helisalmi, M. T. Heneka, I. Hernández, M. J. Herrmann, P. Hoffmann, C. Holmes, H. Holstege, R. H. Vilas, M. Hulsman, J. Humphrey, G. J. Biessels, X. Jian, C. Johansson, G. R. Jun, Y. Kastumata, J. Kauwe, P. G. Kehoe, L. Kilander, A. K. Ståhlbom, M. Kivipelto, A. Koivisto, J. Kornhuber, M. H. Kosmidis, W. A. Kukull, P. P. Kuksa, B. W. Kunkle, A. B. Kuzma, C. Lage, E. J. Laukka, L. Launer, A. Lauria, C.-Y. Lee, J. Lehtisalo, O. Lerch, A. Lleó, W. Longstreth Jr, O. Lopez, A. L. de Munain, S. Love, M. Löwemark, L. Luckcuck, K. L. Lunetta, Y. Ma, J. Macías, C. A. MacLeod, W. Maier, F. Mangialasche, M. Spallazzi, M. Marquié, R. Marshall, E. R. Martin, A. M. Montes, C. M. Rodríguez, C. Masullo, R. Mayeux, S. Mead, P. Mecocci, M. Medina, A. Meggy, S. Mehrabian, S. Mendoza, M. Menéndez-González, P. Mir, S. Moebus, M. Mol, L. Molina-Porcel, L. Montrreal, L. Morelli, F. Moreno, K. Morgan, T. Mosley, M. M. Nöthen, C. Muchnik, S. Mukherjee, B. Nacmias, T. Ngandu, G. Nicolas, B. G. Nordestgaard, R. Olaso, A. Orellana, M. Orsini, G. Ortega, A. Padovani, C. Paolo, G. Papenberg, L. Parnetti, F. Pasquier, P. Pastor, G. Peloso, A. Pérez-Cordón, J. Pérez-Tur, P. Pericard, O. Peters, Y. A. L. Pijnenburg, J. A. Pineda, G. Piñol-Ripoll, C. Pisanu, T. Polak, J. Popp, D. Posthuma, J. Priller, R. Puerta, O. Quenez, I. Quintela, J. Q. Thomassen, A. Rábano, I. Rainero, F. Rajabli, I. Ramakers, L. M. Real, M. J. T. Reinders, C. Reitz, D. Reyes-Dumeyer, P. Ridge, S. Riedel-Heller, P. Riederer, N. Roberto, E. Rodriguez-Rodriguez, A. Rongve, I. R. Allende, M. Rosende-Roca, J. L. Royo, E. Rubino, D. Rujescu, M. E. Sáez, P. Sakka, I. Saltvedt, Á. Sanabria, M. B. Sánchez-Arjona, F. Sanchez-Garcia, P. S. Juan, R. Sánchez-Valle, S. B. Sando, C. Sarnowski, C. L. Satizabal, M. Scamosci, N. Scarmeas, E. Scarpini, P. Scheltens, N. Scherbaum, M. Scherer, M. Schmid, A. Schneider, J. M. Schott, G. Selbæk, D. Seripa, M. Serrano, J. Sha, A. A. Shadrin, O. Skrobot, S. Slifer, G. J. L. Snijders, H. Soininen, V. Solfrizzi, A. Solomon, Y. Song, S. Sorbi, O. Sotolongo-Grau, G. Spalletta, A. Spottke, A. Squassina, E. Stordal, J. P. Tartan, L. Tárraga, N. Tesí, A. Thalamuthu, T. Thomas, G. Tosto, L. Traykov, L. Tremolizzo, A. Tybjærg-Hansen, A. Uitterlinden, A. Ullgren, I. Ulstein, S. Valero, O. Valladares, C. Van Broeckhoven, J. Vance, B. N. Vardarajan, A. van der Lugt, J. Van Dongen, J. van Rooij, J. van Swieten, R. Vandenberghe, F. Verhey, J.-S. Vidal, J. Vogelgsang, M. Vyhnalek, M. Wagner, D. Wallon, L.-S. Wang, R. Wang, L. Weinhold, J. Wiltfang, G. Windle, B. Woods, M. Yannakoulia, H. Zare, Y. Zhao, X. Zhang, C. Zhu, M. Zulaica, EADB, GR@ACE, DEGESCO, EADI, GERAD, Demgene, FinnGen, ADGC, CHARGE, L. A. Farrer, B. M. Psaty, M. Ghanbari, T. Raj, P. Sachdev, K. Mather, F. Jessen, M. A. Ikram, A. de Mendonça, J. Hort, M. Tsolaki, M. A. Pericak-Vance, P. Amouyel, J. Williams, R. Frikke-Schmidt, J. Clarimon, J.-F. Deleuze, G. Rossi, S. Seshadri, O. A. Andreassen, M. Ingelsson, M. Hiltunen, K. Sleegers, G. D. Schellenberg, C. M. van Duijn, R. Sims, W. M. van der Flier, A. Ruiz, A. Ramirez, J.-C. Lambert, New insights into the genetic etiology of Alzheimer's disease and related dementias. *Nat. Genet.* **54**, 412–436 (2022).

9. R. Kosoy, J. F. Fullard, B. Zeng, J. Bendl, P. Dong, S. Rahman, S. P. Kleopoulos, Z. Shao, K. Girdhar, J. Humphrey, K. de Paiva Lopes, A. W. Charney, B. H. Kopell, T. Raj, D. Bennett, C. P. Kellner, V. Haroutunian, G. E. Hoffman, P. Roussos, Genetics of the human microglia regulome refines Alzheimer's disease risk loci. *Nat. Genet.* **54**, 1145–1154 (2022).

10. Y. Chen, M. Colonna, Two-faced behavior of microglia in Alzheimer's disease. *Nat. Neurosci.* **25**, 3–4 (2022).

11. M. Olah, V. Menon, N. Habib, M. F. Taga, Y. Ma, C. J. Yung, M. Cimpean, A. Khairallah, G. Coronas-Samano, R. Sankowski, D. Grün, A. A. Kroshilina, D. Dionne, R. A. Sarkis, G. R. Cosgrove, J. Helgager, J. A. Golden, P. B. Pennell, M. Prinz, J. P. G. Vonsattel, A. F. Teich, J. A. Schneider, D. A. Bennett, A. Regev, W. Elyaman, E. M. Bradshaw, P. L. De Jager, Single cell RNA sequencing of human microglia uncovers a subset associated with Alzheimer's disease. *Nat. Commun.* **11**, 6129 (2020).

12. H. Mathys, J. Davila-Velderrain, Z. Peng, F. Gao, S. Mohammadi, J. Z. Young, M. Menon, L. He, F. Abdurrob, X. Jiang, A. J. Martorell, R. M. Ransohoff, B. P. Hafler, D. A. Bennett, M. Kellis, L.-H. Tsai, Single-cell transcriptomic analysis of Alzheimer's disease. *Nature* **570**, 332–337 (2019).

13. T. Masuda, R. Sankowski, O. Staszewski, C. Böttcher, L. Amann, Sagar, C. Scheiwe, S. Nessler, P. Kunz, G. van Loo, V. A. Coenen, P. C. Reinacher, A. Michel, U. Sure, R. Gold, D. Grün, J. Priller, C. Stadelmann, M. Prinz, Spatial and temporal heterogeneity of mouse and human microglia at single-cell resolution. *Nature* **566**, 388–392 (2019).

14. N. Sun, M. B. Victor, Y. P. Park, X. Xiong, A. N. Scannail, N. Leary, S. Prosper, S. Viswanathan, X. Luna, C. A. Boix, B. T. James, Y. Tanigawa, K. Galani, H. Mathys, X. Jiang, A. P. Ng, D. A. Bennett, L.-H. Tsai, M. Kellis, Human microglial state dynamics in Alzheimer's disease progression. *Cell* **186**, 4386–4403.e29 (2023).

15. R. C. Paolicelli, A. Sierra, B. Stevens, M.-E. Tremblay, A. Aguzzi, B. Ajami, I. Amit, E. Audinat, I. Bechmann, M. Bennett, F. Bennett, A. Bessis, K. Biber, S. Bilbo, M. Blurton-Jones, E. Boddeke, D. Brites, B. Brône, G. C. Brown, O. Butovsky, M. J. Carson, B. Castellano, M. Colonna, S. A. Cowley, C. Cunningham, D. Davalos, P. L. De Jager, B. de Strooper, A. Denes, B. J. L. Eggen, U. Eyo, E. Galea, S. Garel, F. Ginhoux, C. K. Glass, O. Gokce, D. Gomez-Nicola, B. González, S. Gordon, M. B. Graeber, A. D. Greenhalgh, P. Gressens, M. Greter, D. H. Gutmann, C. Haass, M. T. Heneka, F. L. Heppner, S. Hong, D. A. Hume, S. Jung, H. Kettenmann, J. Kipnis, R. Koyama, G. Lemke, M. Lynch, A. Majewska, M. Malcangio, T. Malm, R. Mancuso, T. Masuda, M. Matteoli, B. W. McColl, V. E. Miron, A. V. Molofsky, M. Monje, E. Mracsko, A. Nadjar, J. J. Neher, U. Neniskyte, H. Neumann, M. Noda, B. Peng, F. Peri, V. H. Perry, P. G. Popovich, C. Pridans, J. Priller, M. Prinz, D. Ragozzino, R. M. Ransohoff, M. W. Salter, A. Schaefer, D. P. Schafer, M. Schwartz, M. Simons, C. J. Smith, W. J. Streit, T. L. Tay, L.-H. Tsai, A. Verkhratsky, R. von Bernhardi, H. Wake, V. Wittamer, S. A. Wolf, L.-J. Wu, T. Wyss-Coray, Microglia states and nomenclature: A field at its crossroads. *Neuron* **110**, 3458–3483 (2022).

16. N. Thrupp, C. Sala Frigerio, L. Wolfs, N. G. Skene, N. Fattorelli, S. Poovathingal, Y. Fourne, P. M. Matthews, T. Theys, R. Mancuso, B. de Strooper, M. Fiers, Single-Nucleus RNA-Seq Is Not Suitable for Detection of Microglial Activation Genes in Humans. *Cell Rep.* **32**, 108189 (2020).

17. S. E. Marsh, A. J. Walker, T. Kamath, L. Dissing-Olesen, T. R. Hammond, T. Y. de Soysa, A. M. H. Young, S. Murphy, A. Abdulraouf, N. Nadaf, C. Dufort, A. C. Walker, L. E. Lucca, V. Kozareva, C. Vanderburg, S. Hong, H. Bulstrode, P. J. Hutchinson, D. J. Gaffney, D. A. Hafler, R. J. M. Franklin, E. Z. Macosko, B. Stevens, Dissection of artifactual and confounding glial signatures by single-cell sequencing of mouse and human brain. *Nat. Neurosci.* **25**, 306–316 (2022).

18. M. Stoeckius, C. Hafemeister, W. Stephenson, B. Houck-Loomis, P. K. Chattopadhyay, H. Swerdlow, R. Satija, P. Smibert, Simultaneous epitope and transcriptome measurement in single cells. *Nat. Methods* **14**, 865–868 (2017).

19. S. S. Mirra, A. Heyman, D. McKeel, S. M. Sumi, B. J. Crain, L. M. Brownlee, F. S. Vogel, J. P. Hughes, G. van Belle, L. Berg, The Consortium to Establish a Registry for Alzheimer's Disease (CERAD). Part II. Standardization of the neuropathologic assessment of Alzheimer's disease. *Neurology* **41**, 479–486 (1991).

20. H. Braak, E. Braak, Evolution of the neuropathology of Alzheimer's disease. *Acta Neurol. Scand. Suppl.* **165**, 3–12 (1996).

21. A. Ajoolabady, D. Lindholm, J. Ren, D. Pratico, ER stress and UPR in Alzheimer's disease: mechanisms, pathogenesis, treatments. *Cell Death Dis.* **13**, 706 (2022).

22. A. M. Smith, K. Davey, S. Tsartsalis, C. Khozoie, N. Fancy, S. S. Tang, E. Liaptsi, M. Weinert, A. McGarry, R. C. J. Muirhead, S. Gentleman, D. R. Owen, P. M. Matthews, Diverse human astrocyte and microglial transcriptional responses to Alzheimer's pathology. *Acta Neuropathol.* **143**, 75–91 (2022).

23. M.-J. Dolan, M. Therrien, S. Jereb, T. Kamath, V. Gazestani, T. Atkeson, S. E. Marsh, A. Goeva, N. M. Lojek, S. Murphy, C. M. White, J. Joung, B. Liu, F. Limone, K. Eggan, N. Hacohen, B. E. Bernstein, C. K. Glass, V. Leinonen, M. Blurton-Jones, F. Zhang, C. B. Epstein, E. Z. Macosko, B. Stevens, Exposure of iPSC-derived human microglia to brain substrates enables the generation and manipulation of diverse transcriptional states in vitro. *Nat. Immunol.* **24**, 1382–1390 (2023).

24. J. Marschallinger, T. Iram, M. Zardeneta, S. E. Lee, B. Lehallier, M. S. Haney, J. V. Pluvinage, V. Mathur, O. Hahn, D. W. Morgens, J. Kim, J. Tevini, T. K. Felder, H. Wolinski, C. R. Bertozzi, M. C. Bassik, L. Aigner, T. Wyss-Coray, Lipid-droplet-accumulating microglia represent a dysfunctional and proinflammatory state in the aging brain. *Nat. Neurosci.* **23**, 194–208 (2020).

25. A. Silvin, S. Uderhardt, C. Piot, S. Da Mesquita, K. Yang, L. Geirsdottir, K. Mulder, D. Eyal, Z. Liu, C. Bridlance, M. S. Thion, X. M. Zhang, W. T. Kong, M. Deloger, V. Fontes, A. Weiner, R. Ee, R. Dress, J. W. Hang, A. Balachander, S. Chakarov, B. Malleret, G. Dunsmore, O. Cexus, J. Chen, S. Garel, C. A. Dutertre, I. Amit, J. Kipnis, F. Ginhoux, Dual ontogeny of disease-associated microglia and disease inflammatory macrophages in aging and neurodegeneration. *Immunity* **55**, 1448–1465.e6 (2022).

26. A. C. Lieber, I. T. McNeill, J. Scaggiante, D. A. Nistal, M. Fowkes, M. Umphlett, J. Pan, P. Roussos, C. V. Mobbs, J. Mocco, C. P. Kellner, Biopsy During Minimally Invasive Intracerebral Hemorrhage Clot Evacuation. *World Neurosurg.*, doi:

1751   10.1016/j.wneu.2018.12.058 (2018).

1752   27. Y. Zhou, W. M. Song, P. S. Andhey, A. Swain, T. Levy, K. R. Miller, P. L. Poliani, M.
1753   Cominelli, S. Grover, S. Gilfillan, M. Cella, T. K. Ulland, K. Zaitsev, A. Miyashita, T. Ikeuchi,
1754   M. Sainouchi, A. Kakita, D. A. Bennett, J. A. Schneider, M. R. Nichols, S. A. Beausoleil, J.
1755   D. Ulrich, D. M. Holtzman, M. N. Artyomov, M. Colonna, Human and mouse single-nucleus
1756   transcriptomics reveal TREM2-dependent and TREM2-independent cellular responses in
1757   Alzheimer's disease. *Nat. Med.* **26**, 131–142 (2020).

1758   28. J. Ma, J.-T. Yu, L. Tan, MS4A Cluster in Alzheimer's Disease. *Mol. Neurobiol.* **51**, 1240–
1759   1248 (2015).

1760   29. D. Klein, G. Palla, M. Lange, M. Klein, Z. Piran, M. Gander, L. Meng-Papaxanthos, M.
1761   Sterr, A. Bastidas-Ponce, M. Tarquis-Medina, H. Lickert, M. Bakhti, M. Nitzan, M. Cuturi,
1762   F. J. Theis, Mapping cells through time and space with moscot, *bioRxiv* (2023)p.
1763   2023.05.11.540374.

1764   30. P. Weiler, M. Lange, M. Klein, D. Pe'er, F. J. Theis, Unified fate mapping in multiview
1765   single-cell data, *bioRxiv* (2023)p. 2023.07.19.549685.

1766   31. S. Aibar, C. B. González-Blas, T. Moerman, V. A. Huynh-Thu, H. Imrichova, G. Hulselmans,
1767   F. Rambow, J.-C. Marine, P. Geurts, J. Aerts, J. van den Oord, Z. K. Atak, J. Wouters, S.
1768   Aerts, SCENIC: single-cell regulatory network inference and clustering. *Nat. Methods* **14**,
1769   1083–1086 (2017).

1770   32. B. Van de Sande, C. Flerin, K. Davie, M. De Waegeneer, G. Hulselmans, S. Aibar, R.
1771   Seurinck, W. Saelens, R. Cannoodt, Q. Rouchon, T. Verbeiren, D. De Maeyer, J. Reumers,
1772   Y. Saeys, S. Aerts, A scalable SCENIC workflow for single-cell gene regulatory network
1773   analysis. *Nat. Protoc.* **15**, 2247–2276 (2020).

1774   33. D. Dimitrov, D. Türei, M. Garrido-Rodriguez, P. L. Burmedi, J. S. Nagai, C. Boys, R. O.
1775   Ramirez Flores, H. Kim, B. Szalai, I. G. Costa, A. Valdeolivas, A. Dugourd, J. Saez-
1776   Rodriguez, Comparison of methods and resources for cell-cell communication inference
1777   from single-cell RNA-Seq data. *Nat. Commun.* **13**, 3224 (2022).

1778   34. C. A. de Leeuw, J. M. Mooij, T. Heskes, D. Posthuma, MAGMA: generalized gene-set
1779   analysis of GWAS data. *PLoS Comput. Biol.* **11**, e1004219 (2015).

1780   35. Y. Wang, M. Cella, K. Mallinson, J. D. Ulrich, K. L. Young, M. L. Robinette, S. Gilfillan, G.
1781   M. Krishnan, S. Sudhakar, B. H. Zinselmeyer, D. M. Holtzman, J. R. Cirrito, M. Colonna,
1782   TREM2 lipid sensing sustains the microglial response in an Alzheimer's disease model.
1783   *Cell* **160**, 1061–1071 (2015).

1784   36. T. R. Jay, C. M. Miller, P. J. Cheng, L. C. Graham, S. Bemiller, M. L. Broihier, G. Xu, D.
1785   Margevicius, J. C. Karlo, G. L. Sousa, A. C. Cotleur, O. Butovsky, L. Bekris, S. M.
1786   Staugaitis, J. B. Leverenz, S. W. Pimplikar, G. E. Landreth, G. R. Howell, R. M. Ransohoff,
1787   B. T. Lamb, TREM2 deficiency eliminates TREM2+ inflammatory macrophages and
1788   ameliorates pathology in Alzheimer's disease mouse models. *J. Exp. Med.* **212**, 287–295
1789   (2015).

37. P. Yuan, C. Condello, C. D. Keene, Y. Wang, T. D. Bird, S. M. Paul, W. Luo, M. Colonna, D. Baddeley, J. Grutzendler, TREM2 haplodeficiency in mice and humans impairs the microglia barrier function leading to decreased amyloid compaction and severe axonal dystrophy. *Neuron* **90**, 724–739 (2016).

38. Y. Wang, T. K. Ulland, J. D. Ulrich, W. Song, J. A. Tzaferis, J. T. Hole, P. Yuan, T. E. Mahan, Y. Shi, S. Gilfillan, M. Cella, J. Grutzendler, R. B. DeMattos, J. R. Cirrito, D. M. Holtzman, M. Colonna, TREM2-mediated early microglial response limits diffusion and toxicity of amyloid plaques. *J. Exp. Med.* **213**, 667–675 (2016).

39. T. K. Ulland, M. Colonna, TREM2 - a key player in microglial biology and Alzheimer disease. *Nat. Rev. Neurol.* **14**, 667–675 (2018).

40. W. M. Song, S. Joshita, Y. Zhou, T. K. Ulland, S. Gilfillan, M. Colonna, Humanized TREM2 mice reveal microglia-intrinsic and -extrinsic effects of R47H polymorphism. *J. Exp. Med.* **215**, 745–760 (2018).

41. H. Tanaka, M. Shimazawa, M. Kimura, M. Takata, K. Tsuruma, M. Yamada, H. Takahashi, I. Hozumi, J.-I. Niwa, Y. Iguchi, T. Nikawa, G. Sobue, T. Inuzuka, H. Hara, The potential of GPNMB as novel neuroprotective factor in amyotrophic lateral sclerosis. *Sci. Rep.* **2**, 573 (2012).

42. M. L. Neal, A. M. Boyle, K. M. Budge, F. F. Safadi, J. R. Richardson, The glycoprotein GPNMB attenuates astrocyte inflammatory responses through the CD44 receptor. *J. Neuroinflammation* **15**, 73 (2018).

43. D. A. Kia, D. Zhang, S. Guelfi, C. Manzoni, L. Hubbard, R. H. Reynolds, J. Botía, M. Ryten, R. Ferrari, P. A. Lewis, N. Williams, D. Trabzuni, J. Hardy, N. W. Wood, United Kingdom Brain Expression Consortium (UKBEC) and the International Parkinson's Disease Genomics Consortium (IPDGC), Identification of Candidate Parkinson Disease Genes by Integrating Genome-Wide Association Study, Expression, and Epigenetic Data Sets. *JAMA Neurol.* **78**, 464–472 (2021).

44. C. S. Storm, D. A. Kia, M. M. Almramhi, S. Bandres-Ciga, C. Finan, International Parkinson's Disease Genomics Consortium (IPDGC), A. D. Hingorani, N. W. Wood, Finding genetically-supported drug targets for Parkinson's disease using Mendelian randomization of the druggable genome. *Nat. Commun.* **12**, 7342 (2021).

45. M. Hüttenrauch, I. Ogorek, H. Klafki, M. Otto, C. Stadelmann, S. Weggen, J. Wiltfang, O. Wirths, Glycoprotein NMB: a novel Alzheimer's disease associated marker expressed in a subset of activated microglia. *Acta Neuropathol. Commun.* **6**, 108 (2018).

46. M. Liguori, E. Digifico, A. Vacchini, R. Avigni, F. S. Colombo, E. M. Borroni, F. M. Farina, S. Milanesi, A. Castagna, L. Mannarino, I. Craparotta, S. Marchini, E. Erba, N. Panini, M. Tamborini, V. Rimoldi, P. Allavena, C. Belgiovine, The soluble glycoprotein NMB (GPNMB) produced by macrophages induces cancer stemness and metastasis via CD44 and IL-33. *Cell. Mol. Immunol.* **18**, 711–722 (2021).

47. Y. Lin, Y. Qi, M. Jiang, W. Huang, B. Li, Lactic acid-induced M2-like macrophages facilitate tumor cell migration and invasion via the GPNMB/CD44 axis in oral squamous

1830   cell carcinoma. *Int. Immunopharmacol.* **124**, 110972 (2023).

1831   48. J. Doroszkiewicz, A. Kulczyńska-Przybik, M. Dulewicz, R. Borawska, M. Zajkowska, A.
1832   Słowik, B. Mroczko, Potential utility of cerebrospinal fluid glycoprotein nonmetastatic
1833   melanoma protein B as a neuroinflammatory diagnostic biomarker in mild cognitive
1834   impairment and Alzheimer's disease. *J. Clin. Med.* **12** (2023).

1835   49. J. Doroszkiewicz, A. Kulczynska-Przybik, M. Dulewicz, R. Borawska, A. Slowik, B.
1836   Mroczko, The cerebrospinal fluid Glycoprotein Nonmetastatic Melanoma Protein B
1837   (GPNMB) concentration in Alzheimer's Disease (AD). *Alzheimers. Dement.* **19** (2023).

1838   50. K. Srinivasan, B. A. Friedman, A. Etxeberria, M. A. Huntley, M. P. van der Brug, O.
1839   Foreman, J. S. Paw, Z. Modrusan, T. G. Beach, G. E. Serrano, D. V. Hansen, Alzheimer's
1840   Patient Microglia Exhibit Enhanced Aging and Unique Transcriptional Activation. *Cell Rep.*
1841   **31**, 107843 (2020).

1842   51. T. Schwabe, K. Srinivasan, H. Rhinn, Shifting paradigms: The central role of microglia in
1843   Alzheimer's disease. *Neurobiol. Dis.* **143**, 104962 (2020).

1844   52. F. Agostini, R. Agostinis, D. L. Medina, M. Bisaglia, E. Greggio, N. Plotegher, The
1845   Regulation of MiTF/TFE Transcription Factors Across Model Organisms: from Brain
1846   Physiology to Implication for Neurodegeneration. *Mol. Neurobiol.* **59**, 5000–5023 (2022).

1847   53. J. Miao, H. Ma, Y. Yang, Y. Liao, C. Lin, J. Zheng, M. Yu, J. Lan, Microglia in Alzheimer's
1848   disease: pathogenesis, mechanisms, and therapeutic potentials. *Front. Aging Neurosci.*
1849   **15**, 1201982 (2023).

1850   54. B. A. Friedman, K. Srinivasan, G. Ayalon, W. J. Meilandt, H. Lin, M. A. Huntley, Y. Cao, S.-
1851   H. Lee, P. C. G. Haddick, H. Ngu, Z. Modrusan, J. L. Larson, J. S. Kaminker, M. P. van der
1852   Brug, D. V. Hansen, Diverse Brain Myeloid Expression Profiles Reveal Distinct Microglial
1853   Activation States and Aspects of Alzheimer's Disease Not Evident in Mouse Models. *Cell
1854   Rep.* **22**, 832–847 (2018).

1855   55. D. A. Bennett, A. S. Buchman, P. A. Boyle, L. L. Barnes, R. S. Wilson, J. A. Schneider,
1856   Religious Orders Study and Rush Memory and Aging Project. *J. Alzheimers. Dis.* **64**, S161–
1857   S189 (2018).

1858   56. D. A. Bennett, J. A. Schneider, Z. Arvanitakis, J. F. Kelly, N. T. Aggarwal, R. C. Shah, R. S.
1859   Wilson, Neuropathology of older persons without cognitive impairment from two
1860   community-based studies. *Neurology* **66**, 1837–1844 (2006).

1861   57. D. A. Bennett, R. S. Wilson, J. A. Schneider, D. A. Evans, L. A. Beckett, N. T. Aggarwal, L.
1862   L. Barnes, J. H. Fox, J. Bach, Natural history of mild cognitive impairment in older persons.
1863   *Neurology* **59**, 198–205 (2002).

1864   58. D. A. Bennett, J. A. Schneider, N. T. Aggarwal, Z. Arvanitakis, R. C. Shah, J. F. Kelly, J. H.
1865   Fox, E. J. Cochran, D. Arends, A. D. Treinkman, R. S. Wilson, Decision rules guiding the
1866   clinical diagnosis of Alzheimer's disease in two community-based cohort studies
1867   compared to standard practice in a clinic-based cohort study. *Neuroepidemiology* **27**,
1868   169–176 (2006).

1869   59. H. Braak, E. Braak, Neuropathological stageing of Alzheimer-related changes. *Acta*
1870   *Neuropathol.* **82**, 239–259 (1991).

1871   60. H. Braak, I. Alafuzoff, T. Arzberger, H. Kretzschmar, K. Del Tredici, Staging of Alzheimer
1872   disease-associated neurofibrillary pathology using paraffin sections and
1873   immunocytochemistry. *Acta Neuropathol.* **112**, 389–404 (2006).

1874   61. H. Braak, D. R. Thal, E. Ghebremedhin, K. Del Tredici, Stages of the pathologic process in
1875   Alzheimer disease: age categories from 1 to 100 years. *J. Neuropathol. Exp. Neurol.* **70**,
1876   960–969 (2011).

1877   62. M. Stoeckius, S. Zheng, B. Houck-Loomis, S. Hao, B. Z. Yeung, W. M. Mauck 3rd, P.
1878   Smibert, R. Satija, Cell Hashing with barcoded antibodies enables multiplexing and
1879   doublet detection for single cell genomics. *Genome Biol.* **19**, 224 (2018).

1880   63. S. J. Fleming, M. D. Chaffin, A. Arduini, A.-D. Akkad, E. Banks, J. C. Marioni, A. A.
1881   Philippakis, P. T. Ellinor, M. Babadi, Unsupervised removal of systematic background
1882   noise from droplet-based single-cell experiments using CellBender. *Nat. Methods* **20**,
1883   1323–1335 (2023).

1884   64. B. Li, J. Gould, Y. Yang, S. Sarkizova, M. Tabaka, O. Ashenberg, Y. Rosen, M. Slyper, M.
1885   S. Kowalczyk, A.-C. Villani, T. Tickle, N. Hacohen, O. Rozenblatt-Rosen, A. Regev,
1886   Cumulus provides cloud-based data analysis for large-scale single-cell and single-nucleus
1887   RNA-seq. *Nat. Methods* **17**, 793–798 (2020).

1888   65. S. L. Wolock, R. Lopez, A. M. Klein, Scrublet: Computational Identification of Cell Doublets
1889   in Single-Cell Transcriptomic Data. *Cell Syst* **8**, 281–291.e9 (2019).

1890   66. I. Korsunsky, N. Millard, J. Fan, K. Slowikowski, F. Zhang, K. Wei, Y. Baglaenko, M.
1891   Brenner, P.-R. Loh, S. Raychaudhuri, Fast, sensitive and accurate integration of single-cell
1892   data with Harmony. *Nat. Methods* **16**, 1289–1296 (2019).

1893   67. V. A. Traag, L. Waltman, N. J. van Eck, From Louvain to Leiden: guaranteeing well-
1894   connected communities. *Sci. Rep.* **9**, 5233 (2019).

1895   68. L. McInnes, J. Healy, J. Melville, UMAP: Uniform Manifold Approximation and Projection
1896   for Dimension Reduction, *arXiv [stat.ML]* (2018). http://arxiv.org/abs/1802.03426.

1897   69. C. Xu, R. Lopez, E. Mehlman, J. Regier, M. I. Jordan, N. Yosef, Probabilistic harmonization
1898   and annotation of single-cell transcriptomics data with deep generative models. *Mol. Syst.*
1899   *Biol.* **17**, e9620 (2021).

1900   70. A. Dobin, C. A. Davis, F. Schlesinger, J. Drenkow, C. Zaleski, S. Jha, P. Batut, M.
1901   Chaisson, T. R. Gingeras, STAR: ultrafast universal RNA-seq aligner. *Bioinformatics* **29**,
1902   15–21 (2013).

1903   71. B. Kaminow, D. Yunusov, A. Dobin, STARsolo: accurate, fast and versatile
1904   mapping/quantification of single-cell and single-nucleus RNA-seq data, *bioRxiv* (2021)p.
1905   2021.05.05.442755.

1906   72. Y. Huang, D. J. McCarthy, O. Stegle, Vireo: Bayesian demultiplexing of pooled single-cell

1907   RNA-seq data without genotype reference. *Genome Biol.* **20**, 273 (2019).

1908   73. F. A. Wolf, P. Angerer, F. J. Theis, SCANPY: large-scale single-cell gene expression data
1909   analysis. *Genome Biol.* **19**, 15 (2018).

1910   74. S. Ma, M. Skarica, Q. Li, C. Xu, R. D. Risgaard, A. T. N. Tebbenkamp, X. Mato-Blanco, R.
1911   Kovner, Ž. Krsnik, X. de Martin, V. Luria, X. Martí-Pérez, D. Liang, A. Karger, D. K.
1912   Schmidt, Z. Gomez-Sanchez, C. Qi, K. T. Gobeske, S. Pochareddy, A. Debnath, C. J.
1913   Hottman, J. Spurrier, L. Teo, A. G. Boghdadi, J. Homman-Ludiye, J. J. Ely, E. W. Daadi, D.
1914   Mi, M. Daadi, O. Marín, P. R. Hof, M.-R. Rasin, J. Bourne, C. C. Sherwood, G. Santpere,
1915   M. J. Girgenti, S. M. Strittmatter, A. M. M. Sousa, N. Sestan, Molecular and cellular
1916   evolution of the primate dorsolateral prefrontal cortex. *Science* **377**, eabo7257 (2022).

1917   75. N. Bray, H. Pimentel, P. Melsted, L. Pachter, Near-optimal RNA-Seq quantification with
1918   kallisto. *Nat. Biotechnol.*

1919   76. P. Bankhead, M. B. Loughrey, J. A. Fernández, Y. Dombrowski, D. G. McArt, P. D. Dunne,
1920   S. McQuaid, R. T. Gray, L. J. Murray, H. G. Coleman, J. A. James, M. Salto-Tellez, P. W.
1921   Hamilton, QuPath: Open source software for digital pathology image analysis. *Sci. Rep.* **7**,
1922   16878 (2017).

1923   77. A. Gayoso, R. Lopez, G. Xing, P. Boyeau, V. Valiollah Pour Amiri, J. Hong, K. Wu, M.
1924   Jayasuriya, E. Mehlman, M. Langevin, Y. Liu, J. Samaran, G. Misrachi, A. Nazaret, O.
1925   Clivio, C. Xu, T. Ashuach, M. Gabitto, M. Lotfollahi, V. Svensson, E. da Veiga Beltrame, V.
1926   Kleshchevnikov, C. Talavera-López, L. Pachter, F. J. Theis, A. Streets, M. I. Jordan, J.
1927   Regier, N. Yosef, A Python library for probabilistic analysis of single-cell omics data. *Nat.*
1928   *Biotechnol.* **40**, 163–166 (2022).

1929   78. I. Virshup, D. Bredikhin, L. Heumos, G. Palla, G. Sturm, A. Gayoso, I. Kats, M. Koutrouli,
1930   Scverse Community, B. Berger, D. Pe'er, A. Regev, S. A. Teichmann, F. Finotello, F. A.
1931   Wolf, N. Yosef, O. Stegle, F. J. Theis, The scverse project provides a computational
1932   ecosystem for single-cell omics data analysis. *Nat. Biotechnol.* **41**, 604–606 (2023).

1933   79. D. Mattei, A. Ivanov, M. van Oostrum, S. Pantelyushin, J. Richetto, F. Mueller, M.
1934   Beffinger, L. Schellhammer, J. Vom Berg, B. Wollscheid, D. Beule, R. C. Paolicelli, U.
1935   Meyer, Enzymatic Dissociation Induces Transcriptional and Proteotype Bias in Brain Cell
1936   Populations. *Int. J. Mol. Sci.* **21** (2020).

1937   80. S. Krasemann, C. Madore, R. Cialic, C. Baufeld, N. Calcagno, R. El Fatimy, L. Beckers, E.
1938   O'Loughlin, Y. Xu, Z. Fanek, D. J. Greco, S. T. Smith, G. Tweet, Z. Humulock, T. Zrzavy, P.
1939   Conde-Sanroman, M. Gacias, Z. Weng, H. Chen, E. Tjon, F. Mazaheri, K. Hartmann, A.
1940   Madi, J. D. Ulrich, M. Glatzel, A. Worthmann, J. Heeren, B. Budnik, C. Lemere, T. Ikezu, F.
1941   L. Heppner, V. Litvak, D. M. Holtzman, H. Lassmann, H. L. Weiner, J. Ochando, C. Haass,
1942   O. Butovsky, The TREM2-APOE pathway drives the transcriptional phenotype of
1943   dysfunctional microglia in neurodegenerative diseases. *Immunity* **47**, 566–581.e9 (2017).

1944   81. Cell Press: STAR Protocols. https://star-protocols.cell.com/protocols/694.

1945   82. L. Li, X. Cao, L. Huang, X. Huang, J. Gu, X. Yu, Y. Zhu, Y. Zhou, Y. Song, M. Zhu,
1946   Lycopene inhibits endothelial-to-mesenchymal transition of choroidal vascular endothelial

cells in laser-induced mouse choroidal neovascularization. *J. Cell. Mol. Med.* **27**, 1327–1340 (2023).

83. G. E. Hoffman, P. Roussos, Dream: powerful differential expression analysis for repeated measures designs. *Bioinformatics* **37**, 192–201 (2021).

84. J. W. Squair, M. Gautier, C. Kathe, M. A. Anderson, N. D. James, T. H. Hutson, R. Hudelle, T. Qaiser, K. J. E. Matson, Q. Barraud, A. J. Levine, G. La Manno, M. A. Skinnider, G. Courtine, Confronting false discoveries in single-cell differential expression. *Nat. Commun.* **12**, 5692 (2021).

85. H. L. Crowell, C. Soneson, P.-L. Germain, D. Calini, L. Collin, C. Raposo, D. Malhotra, M. D. Robinson, muscat detects subpopulation-specific state transitions from multi-sample multi-condition single-cell transcriptomics data. *Nat. Commun.* **11**, 6077 (2020).

86. D. Wu, G. K. Smyth, Camera: a competitive gene set test accounting for inter-gene correlation. *Nucleic Acids Res.* **40**, e133 (2012).

87. D. Tingley, T. Yamamoto, K. Hirose, L. Keele, K. Imai, Mediation:RPackage for causal mediation analysis. *J. Stat. Softw.* **59**, 1–38 (2014).

88. Z. Fang, X. Liu, G. Peltz, GSEApy: a comprehensive package for performing gene set enrichment analysis in Python. *Bioinformatics* **39** (2023).

89. B. Reuter, K. Fackeldey, M. Weber, Generalized Markov modeling of nonreversible molecular kinetics. *J. Chem. Phys.* **150**, 174103 (2019).

90. L. Haghverdi, M. Büttner, F. A. Wolf, F. Buettner, F. J. Theis, Diffusion pseudotime robustly reconstructs lineage branching. *Nat. Methods* **13**, 845–848 (2016).

91. L. Heumos, A. C. Schaar, C. Lance, A. Litinetskaya, F. Drost, L. Zappia, M. D. Lücken, D. C. Strobl, J. Henao, F. Curion, Single-cell Best Practices Consortium, H. B. Schiller, F. J. Theis, Best practices for single-cell analysis across modalities. *Nat. Rev. Genet.*, 1–23 (2023).

92. R. Kolde, S. Laur, P. Adler, J. Vilo, Robust rank aggregation for gene list integration and meta-analysis. *Bioinformatics* **28**, 573–580 (2012).

93. M. Efremova, M. Vento-Tormo, S. A. Teichmann, R. Vento-Tormo, CellPhoneDB: inferring cell-cell communication from combined expression of multi-subunit ligand-receptor complexes. *Nat. Protoc.* **15**, 1484–1506 (2020).

94. M. S. B. Raredon, J. Yang, J. Garritano, M. Wang, D. Kushnir, J. C. Schupp, T. S. Adams, A. M. Greaney, K. L. Leiby, N. Kaminski, Y. Kluger, A. Levchenko, L. E. Niklason, Computation and visualization of cell-cell signaling topologies in single-cell systems data using Connectome. *Sci. Rep.* **12**, 4187 (2022).

95. R. Hou, E. Denisenko, H. T. Ong, J. A. Ramilowski, A. R. R. Forrest, Predicting cell-to-cell communication networks using NATMI. *Nat. Commun.* **11**, 5011 (2020).

96. S. Cabello-Aguilar, M. Alame, F. Kon-Sun-Tack, C. Fau, M. Lacroix, J. Colinge,

1984   SingleCellSignalR: inference of intercellular networks from single-cell transcriptomics.
1985   *Nucleic Acids Res.* **48**, e55 (2020).

1986   97.   S. Jin, C. F. Guerrero-Juarez, L. Zhang, I. Chang, R. Ramos, C.-H. Kuan, P. Myung, M. V.
1987   Plikus, Q. Nie, Inference and analysis of cell-cell communication using CellChat. *Nat.*
1988   *Commun.* **12**, 1088 (2021).

1989   98.   E. Armingol, H. M. Baghdassarian, C. Martino, A. Perez-Lopez, C. Aamodt, R. Knight, N. E.
1990   Lewis, Context-aware deconvolution of cell–cell communication with Tensor-cell2cell. *Nat.*
1991   *Commun.* **13**, 1–15 (2022).

1992   99.   M. Ashburner, C. A. Ball, J. A. Blake, D. Botstein, H. Butler, J. M. Cherry, A. P. Davis, K.
1993   Dolinski, S. S. Dwight, J. T. Eppig, M. A. Harris, D. P. Hill, L. Issel-Tarver, A. Kasarskis, S.
1994   Lewis, J. C. Matese, J. E. Richardson, M. Ringwald, G. M. Rubin, G. Sherlock, Gene
1995   ontology: tool for the unification of biology. The Gene Ontology Consortium. *Nat. Genet.*
1996   **25**, 25–29 (2000).

1997   100.   Gene Ontology Consortium, S. A. Aleksander, J. Balhoff, S. Carbon, J. M. Cherry, H. J.
1998   Drabkin, D. Ebert, M. Feuermann, P. Gaudet, N. L. Harris, D. P. Hill, R. Lee, H. Mi, S.
1999   Moxon, C. J. Mungall, A. Muruganugan, T. Mushayahama, P. W. Sternberg, P. D. Thomas,
2000   K. Van Auken, J. Ramsey, D. A. Siegele, R. L. Chisholm, P. Fey, M. C. Aspromonte, M. V.
2001   Nugnes, F. Quaglia, S. Tosatto, M. Giglio, S. Nadendla, G. Antonazzo, H. Attrill, G. Dos
2002   Santos, S. Marygold, V. Strelets, C. J. Tabone, J. Thurmond, P. Zhou, S. H. Ahmed, P.
2003   Asanitthong, D. Luna Buitrago, M. N. Erdol, M. C. Gage, M. Ali Kadhum, K. Y. C. Li, M.
2004   Long, A. Michalak, A. Pesala, A. Pritazahra, S. C. C. Saverimuttu, R. Su, K. E. Thurlow, R.
2005   C. Lovering, C. Logie, S. Oliferenko, J. Blake, K. Christie, L. Corbani, M. E. Dolan, H. J.
2006   Drabkin, D. P. Hill, L. Ni, D. Sitnikov, C. Smith, A. Cuzick, J. Seager, L. Cooper, J. Elser, P.
2007   Jaiswal, P. Gupta, P. Jaiswal, S. Naithani, M. Lera-Ramirez, K. Rutherford, V. Wood, J. L.
2008   De Pons, M. R. Dwinell, G. T. Hayman, M. L. Kaldunski, A. E. Kwitek, S. J. F. Laulederkind,
2009   M. A. Tutaj, M. Vedi, S.-J. Wang, P. D'Eustachio, L. Aimo, K. Axelsen, A. Bridge, N. Hyka-
2010   Nouspikel, A. Morgat, S. A. Aleksander, J. M. Cherry, S. R. Engel, K. Karra, S. R. Miyasato,
2011   R. S. Nash, M. S. Skrzypek, S. Weng, E. D. Wong, E. Bakker, T. Z. Berardini, L. Reiser, A.
2012   Auchincloss, K. Axelsen, G. Argoud-Puy, M.-C. Blatter, E. Boutet, L. Breuza, A. Bridge, C.
2013   Casals-Casas, E. Coudert, A. Estreicher, M. Livia Famiglietti, M. Feuermann, A. Gos, N.
2014   Gruaz-Gumowski, C. Hulo, N. Hyka-Nouspikel, F. Jungo, P. Le Mercier, D. Lieberherr, P.
2015   Masson, A. Morgat, I. Pedruzzi, L. Pourcel, S. Poux, C. Rivoire, S. Sundaram, A. Bateman,
2016   E. Bowler-Barnett, H. Bye-A-Jee, P. Denny, A. Ignatchenko, R. Ishtiaq, A. Lock, Y. Lussi,
2017   M. Magrane, M. J. Martin, S. Orchard, P. Raposo, E. Speretta, N. Tyagi, K. Warner, R.
2018   Zaru, A. D. Diehl, R. Lee, J. Chan, S. Diamantakis, D. Raciti, M. Zarowiecki, M. Fisher, C.
2019   James-Zorn, V. Ponferrada, A. Zorn, S. Ramachandran, L. Ruzicka, M. Westerfield, The
2020   Gene Ontology knowledgebase in 2023. *Genetics* **224** (2023).

2021   101.   International Multiple Sclerosis Genetics Consortium, Multiple sclerosis genomic map
2022   implicates peripheral immune cells and microglia in susceptibility. *Science* **365** (2019).

2023   102.   M. A. Nalls, C. Blauwendraat, C. L. Vallerga, K. Heilbron, S. Bandres-Ciga, D. Chang,
2024   M. Tan, D. A. Kia, A. J. Noyce, A. Xue, J. Bras, E. Young, R. von Coelln, J. Simón-
2025   Sánchez, C. Schulte, M. Sharma, L. Krohn, L. Pihlstrøm, A. Siitonen, H. Iwaki, H. Leonard,
2026   F. Faghri, J. R. Gibbs, D. G. Hernandez, S. W. Scholz, J. A. Botia, M. Martinez, J.-C.
2027   Corvol, S. Lesage, J. Jankovic, L. M. Shulman, M. Sutherland, P. Tienari, K. Majamaa, M.

Toft, O. A. Andreassen, T. Bangale, A. Brice, J. Yang, Z. Gan-Or, T. Gasser, P. Heutink, J. M. Shulman, N. W. Wood, D. A. Hinds, J. A. Hardy, H. R. Morris, J. Gratten, P. M. Visscher, R. R. Graham, A. B. Singleton, 23andMe Research Team, System Genomics of Parkinson's Disease Consortium, International Parkinson's Disease Genomics Consortium, Identification of novel risk loci, causal insights, and heritable risk for Parkinson's disease: a meta-analysis of genome-wide association studies. *Lancet Neurol.* **18**, 1091–1102 (2019).

103.   T. D. Als, M. I. Kurki, J. Grove, G. Voloudakis, K. Therrien, E. Tasanko, T. T. Nielsen, J. Naamanka, K. Veerapen, D. F. Levey, J. Bendl, J. Bybjerg-Grauholm, B. Zeng, D. Demontis, A. Rosengren, G. Athanasiadis, M. Bækved-Hansen, P. Qvist, G. Bragi Walters, T. Thorgeirsson, H. Stefánsson, K. L. Musliner, V. M. Rajagopal, L. Farajzadeh, J. Thirstrup, B. J. Vilhjálmsson, J. J. McGrath, M. Mattheisen, S. Meier, E. Agerbo, K. Stefánsson, M. Nordentoft, T. Werge, D. M. Hougaard, P. B. Mortensen, M. B. Stein, J. Gelernter, I. Hovatta, P. Roussos, M. J. Daly, O. Mors, A. Palotie, A. D. Børglum, Depression pathophysiology, risk prediction of recurrence and comorbid psychiatric disorders using genome-wide analyses. *Nat. Med.* **29**, 1832–1844 (2023).

104.   J. Grove, S. Ripke, T. D. Als, M. Mattheisen, R. K. Walters, H. Won, J. Pallesen, E. Agerbo, O. A. Andreassen, R. Anney, Others, Identification of common genetic risk variants for autism spectrum disorder. *Nat. Genet.* **51**, 431–444 (2019).

105.   N. Mullins, A. J. Forstner, K. S. O'Connell, B. Coombes, J. R. I. Coleman, Z. Qiao, T. D. Als, T. B. Bigdeli, S. Børte, J. Bryois, A. W. Charney, O. K. Drange, M. J. Gandal, S. P. Hagenaars, M. Ikeda, N. Kamitaki, M. Kim, K. Krebs, G. Panagiotaropoulou, B. M. Schilder, L. G. Sloofman, S. Steinberg, V. Trubetskoy, B. S. Winsvold, H.-H. Won, L. Abramova, K. Adorjan, E. Agerbo, M. Al Eissa, D. Albani, N. Alliey-Rodriguez, A. Anjorin, V. Antilla, A. Antoniou, S. Awasthi, J. H. Baek, M. Bækvad-Hansen, N. Bass, M. Bauer, E. C. Beins, S. E. Bergen, A. Birner, C. Bøcker Pedersen, E. Bøen, M. P. Boks, R. Bosch, M. Brum, B. M. Brumpton, N. Brunkhorst-Kanaan, M. Budde, J. Bybjerg-Grauholm, W. Byerley, M. Cairns, M. Casas, P. Cervantes, T.-K. Clarke, C. Cruceanu, A. Cuellar-Barboza, J. Cunningham, D. Curtis, P. M. Czerski, A. M. Dale, N. Dalkner, F. S. David, F. Degenhardt, S. Djurovic, A. L. Dobbyn, A. Douzenis, T. Elvsåshagen, V. Escott-Price, I. N. Ferrier, A. Fiorentino, T. M. Foroud, L. Forty, J. Frank, O. Frei, N. B. Freimer, L. Frisén, K. Gade, J. Garnham, J. Gelernter, M. Giørtz Pedersen, I. R. Gizer, S. D. Gordon, K. Gordon-Smith, T. A. Greenwood, J. Grove, J. Guzman-Parra, K. Ha, M. Haraldsson, M. Hautzinger, U. Heilbronner, D. Hellgren, S. Herms, P. Hoffmann, P. A. Holmans, L. Huckins, S. Jamain, J. S. Johnson, J. L. Kalman, Y. Kamatani, J. L. Kennedy, S. Kittel-Schneider, J. A. Knowles, M. Kogevinas, M. Koromina, T. M. Kranz, H. R. Kranzler, M. Kubo, R. Kupka, S. A. Kushner, C. Lavebratt, J. Lawrence, M. Leber, H.-J. Lee, P. H. Lee, S. E. Levy, C. Lewis, C. Liao, S. Lucae, M. Lundberg, D. J. MacIntyre, S. H. Magnusson, W. Maier, A. Maihofer, D. Malaspina, E. Maratou, L. Martinsson, M. Mattheisen, S. A. McCarroll, N. W. McGregor, P. McGuffin, J. D. McKay, H. Medeiros, S. E. Medland, V. Millischer, G. W. Montgomery, J. L. Moran, D. W. Morris, T. W. Mühleisen, N. O'Brien, C. O'Donovan, L. M. Olde Loohuis, L. Oruc, S. Papiol, A. F. Pardiñas, A. Perry, A. Pfennig, E. Porichi, J. B. Potash, D. Quested, T. Raj, M. H. Rapaport, J. R. DePaulo, E. J. Regeer, J. P. Rice, F. Rivas, M. Rivera, J. Roth, P. Roussos, D. M. Ruderfer, C. Sánchez-Mora, E. C. Schulte, F. Senner, S. Sharp, P. D. Shilling, E. Sigurdsson, L. Sirignano, C. Slaney, O. B. Smeland, D. J. Smith, J. L. Sobell, C. Søholm Hansen, M. Soler Artigas, A. T. Spijker, D. J. Stein, J. S. Strauss, B. Świątkowska, C. Terao, T. E. Thorgeirsson, C. Toma, P. Tooney, E.-E. Tsermpini, M. P. Vawter, H.

Vedder, J. T. R. Walters, S. H. Witt, S. Xi, W. Xu, J. M. K. Yang, A. H. Young, H. Young, P.
P. Zandi, H. Zhou, L. Zillich, HUNT All-In Psychiatry, R. Adolfsson, I. Agartz, M. Alda, L.
Alfredsson, G. Babadjanova, L. Backlund, B. T. Baune, F. Bellivier, S. Bengesser, W. H.
Berrettini, D. H. R. Blackwood, M. Boehnke, A. D. Børglum, G. Breen, V. J. Carr, S. Catts,
A. Corvin, N. Craddock, U. Dannlowski, D. Dikeos, T. Esko, B. Etain, P. Ferentinos, M.
Frye, J. M. Fullerton, M. Gawlik, E. S. Gershon, F. S. Goes, M. J. Green, M. Grigoroiu-
Serbanescu, J. Hauser, F. Henskens, J. Hillert, K. S. Hong, D. M. Hougaard, C. M.
Hultman, K. Hveem, N. Iwata, A. V. Jablensky, I. Jones, L. A. Jones, R. S. Kahn, J. R.
Kelsoe, G. Kirov, M. Landén, M. Leboyer, C. M. Lewis, Q. S. Li, J. Lissowska, C. Lochner,
C. Loughland, N. G. Martin, C. A. Mathews, F. Mayoral, S. L. McElroy, A. M. McIntosh, F.
J. McMahon, I. Melle, P. Michie, L. Milani, P. B. Mitchell, G. Morken, O. Mors, P. B.
Mortensen, B. Mowry, B. Müller-Myhsok, R. M. Myers, B. M. Neale, C. M. Nievergelt, M.
Nordentoft, M. M. Nöthen, M. C. O'Donovan, K. J. Oedegaard, T. Olsson, M. J. Owen, S.
A. Paciga, C. Pantelis, C. Pato, M. T. Pato, G. P. Patrinos, R. H. Perlis, D. Posthuma, J. A.
Ramos-Quiroga, A. Reif, E. Z. Reininghaus, M. Ribasés, M. Rietschel, S. Ripke, G. A.
Rouleau, T. Saito, U. Schall, M. Schalling, P. R. Schofield, T. G. Schulze, L. J. Scott, R. J.
Scott, A. Serretti, C. Shannon Weickert, J. W. Smoller, H. Stefansson, K. Stefansson, E.
Stordal, F. Streit, P. F. Sullivan, G. Turecki, A. E. Vaaler, E. Vieta, J. B. Vincent, I. D.
Waldman, T. W. Weickert, T. Werge, N. R. Wray, J.-A. Zwart, J. M. Biernacka, J. I.
Nurnberger, S. Cichon, H. J. Edenberg, E. A. Stahl, A. McQuillin, A. Di Florio, R. A. Ophoff,
O. A. Andreassen, Genome-wide association study of more than 40,000 bipolar disorder
cases provides new insights into the underlying biology. *Nat. Genet.* **53**, 817–829 (2021).

106. V. Trubetskoy, A. F. Pardiñas, T. Qi, G. Panagiotaropoulou, S. Awasthi, T. B. Bigdeli, J.
Bryois, C.-Y. Chen, C. A. Dennison, L. S. Hall, M. Lam, K. Watanabe, O. Frei, T. Ge, J. C.
Harwood, F. Koopmans, S. Magnusson, A. L. Richards, J. Sidorenko, Y. Wu, J. Zeng, J.
Grove, M. Kim, Z. Li, G. Voloudakis, W. Zhang, M. Adams, I. Agartz, E. G. Atkinson, E.
Agerbo, M. Al Eissa, M. Albus, M. Alexander, B. Z. Alizadeh, K. Alptekin, T. D. Als, F. Amin,
V. Arolt, M. Arrojo, L. Athanasiu, M. H. Azevedo, S. A. Bacanu, N. J. Bass, M. Begemann,
R. A. Belliveau, J. Bene, B. Benyamin, S. E. Bergen, G. Blasi, J. Bobes, S. Bonassi, A.
Braun, R. A. Bressan, E. J. Bromet, R. Bruggeman, P. F. Buckley, R. L. Buckner, J.
Bybjerg-Grauholm, W. Cahn, M. J. Cairns, M. E. Calkins, V. J. Carr, D. Castle, S. V. Catts,
K. D. Chambert, R. C. K. Chan, B. Chaumette, W. Cheng, E. F. C. Cheung, S. A. Chong, D.
Cohen, A. Consoli, Q. Cordeiro, J. Costas, C. Curtis, M. Davidson, K. L. Davis, L. de Haan,
F. Degenhardt, L. E. DeLisi, D. Demontis, F. Dickerson, D. Dikeos, T. Dinan, S. Djurovic, J.
Duan, G. Ducci, F. Dudbridge, J. G. Eriksson, L. Fañanás, S. V. Faraone, A. Fiorentino, A.
Forstner, J. Frank, N. B. Freimer, M. Fromer, A. Frustaci, A. Gadelha, G. Genovese, E. S.
Gershon, M. Giannitelli, I. Giegling, P. Giusti-Rodríguez, S. Godard, J. I. Goldstein, J.
González Peñas, A. González-Pinto, S. Gopal, J. Gratten, M. F. Green, T. A. Greenwood,
O. Guillin, S. Gülöksüz, R. E. Gur, R. C. Gur, B. Gutiérrez, E. Hahn, H. Hakonarson, V.
Haroutunian, A. M. Hartmann, C. Harvey, C. Hayward, F. A. Henskens, S. Herms, P.
Hoffmann, D. P. Howrigan, M. Ikeda, C. Iyegbe, I. Joa, A. Julià, A. K. Kähler, T. Kam-
Thong, Y. Kamatani, S. Karachanak-Yankova, O. Kebir, M. C. Keller, B. J. Kelly, A.
Khrunin, S.-W. Kim, J. Klovins, N. Kondratiev, B. Konte, J. Kraft, M. Kubo, V. Kučinskas, Z.
A. Kučinskiene, A. Kusumawardhani, H. Kuzelova-Ptackova, S. Landi, L. C. Lazzeroni, P.
H. Lee, S. E. Legge, D. S. Lehrer, R. Lencer, B. Lerer, M. Li, J. Lieberman, G. A. Light, S.
Limborska, C.-M. Liu, J. Lönnqvist, C. M. Loughland, J. Lubinski, J. J. Luykx, A. Lynham,
M. Macek Jr, A. Mackinnon, P. K. E. Magnusson, B. S. Maher, W. Maier, D. Malaspina, J.
Mallet, S. R. Marder, S. Marsal, A. R. Martin, L. Martorell, M. Mattheisen, R. W. McCarley,

2122   C. McDonald, J. J. McGrath, H. Medeiros, S. Meier, B. Melegh, I. Melle, R. I. Mesholam-
2123   Gately, A. Metspalu, P. T. Michie, L. Milani, V. Milanova, M. Mitjans, E. Molden, E. Molina,
2124   M. D. Molto, V. Mondelli, C. Moreno, C. P. Morley, G. Muntané, K. C. Murphy, I. Myin-
2125   Germeys, I. Nenadić, G. Nestadt, L. Nikitina-Zake, C. Noto, K. H. Nuechterlein, N. L.
2126   O'Brien, F. A. O'Neill, S.-Y. Oh, A. Olincy, V. K. Ota, C. Pantelis, G. N. Papadimitriou, M.
2127   Parellada, T. Paunio, R. Pellegrino, S. Periyasamy, D. O. Perkins, B. Pfuhlmann, O.
2128   Pietiläinen, J. Pimm, D. Porteous, J. Powell, D. Quattrone, D. Quested, A. D. Radant, A.
2129   Rampino, M. H. Rapaport, A. Rautanen, A. Reichenberg, C. Roe, J. L. Roffman, J. Roth,
2130   M. Rothermundt, B. P. F. Rutten, S. Saker-Delye, V. Salomaa, J. Sanjuan, M. L. Santoro,
2131   A. Savitz, U. Schall, R. J. Scott, L. J. Seidman, S. I. Sharp, J. Shi, L. J. Siever, E.
2132   Sigurdsson, K. Sim, N. Skarabis, P. Slominsky, H.-C. So, J. L. Sobell, E. Söderman, H. J.
2133   Stain, N. E. Steen, A. A. Steixner-Kumar, E. Stögmann, W. S. Stone, R. E. Straub, F. Streit,
2134   E. Strengman, T. S. Stroup, M. Subramaniam, C. A. Sugar, J. Suvisaari, D. M. Svrakic, N.
2135   R. Swerdlow, J. P. Szatkiewicz, T. M. T. Ta, A. Takahashi, C. Terao, F. Thibaut, D.
2136   Toncheva, P. A. Tooney, S. Torretta, S. Tosato, G. B. Tura, B. I. Turetsky, A. Üçok, A.
2137   Vaaler, T. van Amelsvoort, R. van Winkel, J. Veijola, J. Waddington, H. Walter, A.
2138   Waterreus, B. T. Webb, M. Weiser, N. M. Williams, S. H. Witt, B. K. Wormley, J. Q. Wu, Z.
2139   Xu, R. Yolken, C. C. Zai, W. Zhou, F. Zhu, F. Zimprich, E. C. Atbaşoğlu, M. Ayub, C.
2140   Benner, A. Bertolino, D. W. Black, N. J. Bray, G. Breen, N. G. Buccola, W. F. Byerley, W. J.
2141   Chen, C. R. Cloninger, B. Crespo-Facorro, G. Donohoe, R. Freedman, C. Galletly, M. J.
2142   Gandal, M. Gennarelli, D. M. Hougaard, H.-G. Hwu, A. V. Jablensky, S. A. McCarroll, J. L.
2143   Moran, O. Mors, P. B. Mortensen, B. Müller-Myhsok, A. L. Neil, M. Nordentoft, M. T. Pato,
2144   T. L. Petryshen, M. Pirinen, A. E. Pulver, T. G. Schulze, J. M. Silverman, J. W. Smoller, E.
2145   A. Stahl, D. W. Tsuang, E. Vilella, S.-H. Wang, S. Xu, Indonesia Schizophrenia Consortium,
2146   PsychENCODE, Psychosis Endophenotypes International Consortium, SynGO
2147   Consortium, R. Adolfsson, C. Arango, B. T. Baune, S. I. Belangero, A. D. Børglum, D. Braff,
2148   E. Bramon, J. D. Buxbaum, D. Campion, J. A. Cervilla, S. Cichon, D. A. Collier, A. Corvin,
2149   D. Curtis, M. D. Forti, E. Domenici, H. Ehrenreich, V. Escott-Price, T. Esko, A. H. Fanous,
2150   A. Gareeva, M. Gawlik, P. V. Gejman, M. Gill, S. J. Glatt, V. Golimbet, K. S. Hong, C. M.
2151   Hultman, S. E. Hyman, N. Iwata, E. G. Jönsson, R. S. Kahn, J. L. Kennedy, E.
2152   Khusnutdinova, G. Kirov, J. A. Knowles, M.-O. Krebs, C. Laurent-Levinson, J. Lee, T.
2153   Lencz, D. F. Levinson, Q. S. Li, J. Liu, A. K. Malhotra, D. Malhotra, A. McIntosh, A.
2154   McQuillin, P. R. Menezes, V. A. Morgan, D. W. Morris, B. J. Mowry, R. M. Murray, V.
2155   Nimgaonkar, M. M. Nöthen, R. A. Ophoff, S. A. Paciga, A. Palotie, C. N. Pato, S. Qin, M.
2156   Rietschel, B. P. Riley, M. Rivera, D. Rujescu, M. C. Saka, A. R. Sanders, S. G. Schwab, A.
2157   Serretti, P. C. Sham, Y. Shi, D. St Clair, H. Stefánsson, K. Stefansson, M. T. Tsuang, J. van
2158   Os, M. P. Vawter, D. R. Weinberger, T. Werge, D. B. Wildenauer, X. Yu, W. Yue, P. A.
2159   Holmans, A. J. Pocklington, P. Roussos, E. Vassos, M. Verhage, P. M. Visscher, J. Yang,
2160   D. Posthuma, O. A. Andreassen, K. S. Kendler, M. J. Owen, N. R. Wray, M. J. Daly, H.
2161   Huang, B. M. Neale, P. F. Sullivan, S. Ripke, J. T. R. Walters, M. C. O'Donovan,
2162   Schizophrenia Working Group of the Psychiatric Genomics Consortium, Mapping genomic
2163   loci implicates genes and synaptic biology in schizophrenia. *Nature* **604**, 502–508 (2022).

2164 107.   W. van Rheenen, R. A. A. van der Spek, M. K. Bakker, J. J. F. A. van Vugt, P. J. Hop, R.
2165   A. J. Zwamborn, N. de Klein, H.-J. Westra, O. B. Bakker, P. Deelen, G. Shireby, E.
2166   Hannon, M. Moisse, D. Baird, R. Restuadi, E. Dolzhenko, A. M. Dekker, K. Gawor, H.-J.
2167   Westeneng, G. H. P. Tazelaar, K. R. van Eijk, M. Kooyman, R. P. Byrne, M. Doherty, M.
2168   Heverin, A. Al Khleifat, A. Iacoangeli, A. Shatunov, N. Ticozzi, J. Cooper-Knock, B. N.
2169   Smith, M. Gromicho, S. Chandran, S. Pal, K. E. Morrison, P. J. Shaw, J. Hardy, R. W.

Orrell, M. Sendtner, T. Meyer, N. Başak, A. J. van der Kooi, A. Ratti, I. Fogh, C. Gellera, G. Lauria, S. Corti, C. Cereda, D. Sproviero, S. D'Alfonso, G. Sorarù, G. Siciliano, M. Filosto, A. Padovani, A. Chiò, A. Calvo, C. Moglia, M. Brunetti, A. Canosa, M. Grassano, E. Beghi, E. Pupillo, G. Logroscino, B. Nefussy, A. Osmanovic, A. Nordin, Y. Lerner, M. Zabari, M. Gotkine, R. H. Baloh, S. Bell, P. Vourc'h, P. Corcia, P. Couratier, S. Millecamps, V. Meininger, F. Salachas, J. S. Mora Pardina, A. Assialioui, R. Rojas-García, P. A. Dion, J. P. Ross, A. C. Ludolph, J. H. Weishaupt, D. Brenner, A. Freischmidt, G. Bensimon, A. Brice, A. Durr, C. A. M. Payan, S. Saker-Delye, N. W. Wood, S. Topp, R. Rademakers, L. Tittmann, W. Lieb, A. Franke, S. Ripke, A. Braun, J. Kraft, D. C. Whiteman, C. M. Olsen, A. G. Uitterlinden, A. Hofman, M. Rietschel, S. Cichon, M. M. Nöthen, P. Amouyel, SLALOM Consortium, PARALS Consortium, SLAGEN Consortium, SLAP Consortium, B. J. Traynor, A. B. Singleton, M. Mitne Neto, R. J. Cauchi, R. A. Ophoff, M. Wiedau-Pazos, C. Lomen-Hoerth, V. M. van Deerlin, J. Grosskreutz, A. Roediger, N. Gaur, A. Jörk, T. Barthel, E. Theele, B. Ilse, B. Stubendorff, O. W. Witte, R. Steinbach, C. A. Hübner, C. Graff, L. Brylev, V. Fominykh, V. Demeshonok, A. Ataulina, B. Rogelj, B. Koritnik, J. Zidar, M. Ravnik-Glavač, D. Glavač, Z. Stević, V. Drory, M. Povedano, I. P. Blair, M. C. Kiernan, B. Benyamin, R. D. Henderson, S. Furlong, S. Mathers, P. A. McCombe, M. Needham, S. T. Ngo, G. A. Nicholson, R. Pamphlett, D. B. Rowe, F. J. Steyn, K. L. Williams, K. A. Mather, P. S. Sachdev, A. K. Henders, L. Wallace, M. de Carvalho, S. Pinto, S. Petri, M. Weber, G. A. Rouleau, V. Silani, C. J. Curtis, G. Breen, J. D. Glass, R. H. Brown Jr, J. E. Landers, C. E. Shaw, P. M. Andersen, E. J. N. Groen, M. A. van Es, R. J. Pasterkamp, D. Fan, F. C. Garton, A. F. McRae, G. Davey Smith, T. R. Gaunt, M. A. Eberle, J. Mill, R. L. McLaughlin, O. Hardiman, K. P. Kenna, N. R. Wray, E. Tsai, H. Runz, L. Franke, A. Al-Chalabi, P. Van Damme, L. H. van den Berg, J. H. Veldink, Common and rare variant association analyses in amyotrophic lateral sclerosis identify 15 risk loci with distinct genetic architectures and neuron-specific biology. *Nat. Genet.* **53**, 1636–1648 (2021).

108. D. Taliun, D. N. Harris, M. D. Kessler, J. Carlson, Z. A. Szpiech, R. Torres, S. A. G. Taliun, A. Corvelo, S. M. Gogarten, H. M. Kang, A. N. Pitsillides, J. LeFaive, S.-B. Lee, X. Tian, B. L. Browning, S. Das, A.-K. Emde, W. E. Clarke, D. P. Loesch, A. C. Shetty, T. W. Blackwell, A. V. Smith, Q. Wong, X. Liu, M. P. Conomos, D. M. Bobo, F. Aguet, C. Albert, A. Alonso, K. G. Ardlie, D. E. Arking, S. Aslibekyan, P. L. Auer, J. Barnard, R. G. Barr, L. Barwick, L. C. Becker, R. L. Beer, E. J. Benjamin, L. F. Bielak, J. Blangero, M. Boehnke, D. W. Bowden, J. A. Brody, E. G. Burchard, B. E. Cade, J. F. Casella, B. Chalazan, D. I. Chasman, Y.-D. I. Chen, M. H. Cho, S. H. Choi, M. K. Chung, C. B. Clish, A. Correa, J. E. Curran, B. Custer, D. Darbar, M. Daya, M. de Andrade, D. L. DeMeo, S. K. Dutcher, P. T. Ellinor, L. S. Emery, C. Eng, D. Fatkin, T. Fingerlin, L. Forer, M. Fornage, N. Franceschini, C. Fuchsberger, S. M. Fullerton, S. Germer, M. T. Gladwin, D. J. Gottlieb, X. Guo, M. E. Hall, J. He, N. L. Heard-Costa, S. R. Heckbert, M. R. Irvin, J. M. Johnsen, A. D. Johnson, R. Kaplan, S. L. R. Kardia, T. Kelly, S. Kelly, E. E. Kenny, D. P. Kiel, R. Klemmer, B. A. Konkle, C. Kooperberg, A. Köttgen, L. A. Lange, J. Lasky-Su, D. Levy, X. Lin, K.-H. Lin, C. Liu, R. J. F. Loos, L. Garman, R. Gerszten, S. A. Lubitz, K. L. Lunetta, A. C. Y. Mak, A. Manichaikul, A. K. Manning, R. A. Mathias, D. D. McManus, S. T. McGarvey, J. B. Meigs, D. A. Meyers, J. L. Mikulla, M. A. Minear, B. D. Mitchell, S. Mohanty, M. E. Montasser, C. Montgomery, A. C. Morrison, J. M. Murabito, A. Natale, P. Natarajan, S. C. Nelson, K. E. North, J. R. O'Connell, N. D. Palmer, N. Pankratz, G. M. Peloso, P. A. Peyser, J. Pleiness, W. S. Post, B. M. Psaty, D. C. Rao, S. Redline, A. P. Reiner, D. Roden, J. I. Rotter, I. Ruczinski, C. Sarnowski, S. Schoenherr, D. A. Schwartz, J.-S. Seo, S. Seshadri, V. A. Sheehan, W. H. Sheu, M. B. Shoemaker, N. L. Smith, J. A. Smith, N. Sotoodehnia, A. M.

2218   Stilp, W. Tang, K. D. Taylor, M. Telen, T. A. Thornton, R. P. Tracy, D. J. Van Den Berg, R.
2219   S. Vasan, K. A. Viaud-Martinez, S. Vrieze, D. E. Weeks, B. S. Weir, S. T. Weiss, L.-C.
2220   Weng, C. J. Willer, Y. Zhang, X. Zhao, D. K. Arnett, A. E. Ashley-Koch, K. C. Barnes, E.
2221   Boerwinkle, S. Gabriel, R. Gibbs, K. M. Rice, S. S. Rich, E. K. Silverman, P. Qasba, W.
2222   Gan, NHLBI Trans-Omics for Precision Medicine (TOPMed) Consortium, G. J.
2223   Papanicolaou, D. A. Nickerson, S. R. Browning, M. C. Zody, S. Zöllner, J. G. Wilson, L. A.
2224   Cupples, C. C. Laurie, C. E. Jaquish, R. D. Hernandez, T. D. O'Connor, G. R. Abecasis,
2225   Sequencing of 53,831 diverse genomes from the NHLBI TOPMed Program. *Nature* **590**,
2226   290–299 (2021).

2227   109.   A. Manichaikul, J. C. Mychaleckyj, S. S. Rich, K. Daly, M. Sale, W.-M. Chen, Robust
2228   relationship inference in genome-wide association studies. *Bioinformatics* **26**, 2867–2873
2229   (2010).

2230   110.   1000 Genomes Project Consortium, G. R. Abecasis, A. Auton, L. D. Brooks, M. A.
2231   DePristo, R. M. Durbin, R. E. Handsaker, H. M. Kang, G. T. Marth, G. A. McVean, An
2232   integrated map of genetic variation from 1,092 human genomes. *Nature* **491**, 56–65 (2012).

2233   111.   1000 Genomes Project Consortium, A. Auton, L. D. Brooks, R. M. Durbin, E. P.
2234   Garrison, H. M. Kang, J. O. Korbel, J. L. Marchini, S. McCarthy, G. A. McVean, G. R.
2235   Abecasis, A global reference for human genetic variation. *Nature* **526**, 68–74 (2015).

2236   112.   P. Danecek, J. K. Bonfield, J. Liddle, J. Marshall, V. Ohan, M. O. Pollard, A. Whitwham,
2237   T. Keane, S. A. McCarthy, R. M. Davies, H. Li, Twelve years of SAMtools and BCFtools.
2238   *Gigascience* **10** (2021).

2239   113.   C. C. Chang, C. C. Chow, L. C. Tellier, S. Vattikuti, S. M. Purcell, J. J. Lee, Second-
2240   generation PLINK: rising to the challenge of larger and richer datasets. *Gigascience* **4**, 7
2241   (2015).

2242   114.   T. Ge, C.-Y. Chen, Y. Ni, Y.-C. A. Feng, J. W. Smoller, Polygenic prediction via
2243   Bayesian regression and continuous shrinkage priors. *Nat. Commun.* **10**, 1776 (2019).

2244   115.   C. J. Bohlen, F. C. Bennett, A. F. Tucker, H. Y. Collins, S. B. Mulinyawe, B. A. Barres,
2245   Diverse Requirements for Microglial Survival, Specification, and Function Revealed by
2246   Defined-Medium Cultures. *Neuron* **94**, 759–773.e8 (2017).

2247   116.   D. Gosselin, D. Skola, N. G. Coufal, I. R. Holtman, J. C. M. Schlachetzki, E. Sajti, B. N.
2248   Jaeger, C. O'Connor, C. Fitzpatrick, M. P. Pasillas, M. Pena, A. Adair, D. D. Gonda, M. L.
2249   Levy, R. M. Ransohoff, F. H. Gage, C. K. Glass, An environment-dependent transcriptional
2250   network specifies human microglia identity. *Science* **356** (2017).

2251   117.   S. R. Ocañas, K. D. Pham, H. E. Blankenship, A. H. Machalinski, A. J. Chucair-Elliott, W.
2252   M. Freeman, Minimizing the Ex Vivo Confounds of Cell-Isolation Techniques on
2253   Transcriptomic and Translatomic Profiles of Purified Microglia. *eNeuro* **9** (2022).

2254   118.   S. C. van den Brink, F. Sage, Á. Vértesy, B. Spanjaard, J. Peterson-Maduro, C. S.
2255   Baron, C. Robin, A. van Oudenaarden, Single-cell sequencing reveals dissociation-
2256   induced gene expression in tissue subpopulations. *Nat. Methods* **14**, 935–936 (2017).

2257   119.   Y. Lee, J. S. Lee, K. J. Lee, R. S. Turner, H.-S. Hoe, D. T. S. Pak, Polo-like kinase 2
2258   phosphorylation of amyloid precursor protein regulates activity-dependent amyloidogenic
2259   processing. *Neuropharmacology* **117**, 387–400 (2017).

2260   120.   J. S. Lee, Y. Lee, E. A. André, K. J. Lee, T. Nguyen, Y. Feng, N. Jia, B. T. Harris, M. P.
2261   Burns, D. T. S. Pak, Inhibition of Polo-like kinase 2 ameliorates pathogenesis in
2262   Alzheimer's disease model mice. *PLoS One* **14**, e0219691 (2019).

2263   121.   M. Setty, V. Kiseliovas, J. Levine, A. Gayoso, L. Mazutis, D. Pe'er, Characterization of
2264   cell fate probabilities in single-cell data with Palantir. *Nat. Biotechnol.* **37**, 451–460 (2019).

2265   122.   K. Street, D. Risso, R. B. Fletcher, D. Das, J. Ngai, N. Yosef, E. Purdom, S. Dudoit,
2266   Slingshot: cell lineage and pseudotime inference for single-cell transcriptomics. *BMC*
2267   *Genomics* **19**, 477 (2018).

2268   123.   G. Schiebinger, J. Shu, M. Tabaka, B. Cleary, V. Subramanian, A. Solomon, J. Gould, S.
2269   Liu, S. Lin, P. Berube, L. Lee, J. Chen, J. Brumbaugh, P. Rigollet, K. Hochedlinger, R.
2270   Jaenisch, A. Regev, E. S. Lander, Optimal-Transport Analysis of Single-Cell Gene
2271   Expression Identifies Developmental Trajectories in Reprogramming. *Cell* **176**, 928–
2272   943.e22 (2019).

2273